

# KOBELCO TECHNOLOGY REVIEW

No. **32** Dec. 2013

**Feature- I : Welding and Joining Technologies**

**Feature- II : Energy Machinery and Equipment**

## Contents

### Feature- I Welding and Joining Technologies

Recent Development of High-strength and Tough Welding Consumables for Offshore Structures .....	1
Dr. Yoshihiko KITAGAWA, Hiroyuki KAWASAKI	
Robot Welding Process for Medium and Heavy Plate .....	9
Katsuyuki TSUJI, Akira OGAWA, Dr. Kei YAMAZAKI, Yimin YUAN	
New Welding Process, "J-Solution™ Zn", Suitable for Galvanized Steel in the Automotive Industry .....	16
Shun IZUTANI, Dr. Kei YAMAZAKI, Reiichi SUZUKI	
Expansion of "MX-MIG process" as Pure Argon Gas Shielded Welding Method - for Carbon Steel .....	24
Reiichi SUZUKI, Ryu KASAI	
Effects of Post Weld Heat Treatment (PWHT) Temperature on Mechanical Properties of Weld Metals for High-Cr Ferritic Heat-Resistant Steel .....	33
Genichi TANIGUCHI, Ken YAMASHITA	
Built-in Cable Type Welding Robot "ARCMAN™-GS" .....	40
Shuichi INADA, Makoto KONDO, Yoshihide INOUE, Tatsuji MINATO, Dr. Yoshiharu NISHIDA, Takashi WADA	

### Feature- II Energy Machinery and Equipment

Development and Approach to Future Market of the Eco-Radial Steam Turbine Generator .....	45
Atsushi YOSHIDA, Osamu MATSUTANI	
Manufacturing Technology of Diffusion-bonded Compact Heat Exchanger (DCHE) .....	51
Yasutake MIWA, Dr. Koji NOISHIKI, Tomohiro SUZUKI, Kenichi TAKATSUKI	
Microchannel Reactor (Stacked Multi-Channel Reactor: SMCR®) for Bulk Chemical Industry .....	57
Dr. Koji NOISHIKI, Yasutake MIWA, Akira MATSUOKA	
LNG Vaporizer for LNG Re-gasification Terminal .....	64
Shinji EGASHIRA	
Air-sourced 90°C Hot Water Supplying Heat Pump "HEM-90A" .....	70
Takahiro OUE, Kazuto OKADA	

Editor-in-chief :  
Yasuaki SUGIZAKI

Associate Editors :  
Tomokazu NAKAGAWA  
Hidetoshi INOUE

Editorial Committee :  
Tsunehiro FUKUNAKA  
Toru HASHIMURA  
Kenichi INOUE  
Yasushi MAEDA  
Tsuyoshi MIMURA  
Hiroyuki MORI  
Norihiro NAKAJIMA  
Hiroyuki SHIMIZU  
Syoji YOSHIMURA

Published by

**Secretariat & Publicity Dept.  
Kobe Steel, Ltd.**

2-4, Wakinohama-Kaigandori 2-chome,  
Chuo-ku, Kobe, HYOGO 651-8585,  
JAPAN  
<http://www.kobelco.co.jp>

Editorial Office: **Shinko Research  
Co., Ltd.**

5-5, Takatsukadai 1-chome,  
Nishi-ku, Kobe, HYOGO 651-2271, JAPAN  
Fax: +81-78-992-9790  
E-mail: [rd-office@kobelco.com](mailto:rd-office@kobelco.com)

© Kobe Steel, Ltd. 2013

# Recent Development of High-strength and Tough Welding Consumables for Offshore Structures

Dr. Yoshihiko KITAGAWA\*<sup>1</sup>, Hiroyuki KAWASAKI\*<sup>1</sup>

\*<sup>1</sup> Welding Process Dept., Technical Center, Welding Business

*As the exploration fields for oil and gas resources expand into deeper and colder seas, higher strength and greater toughness are required for the structural materials, including welding materials, used in offshore structures. Recent offshore structures require structural materials having sufficient CTOD properties, including a yield strength of 460MPa or higher and good impact toughness down to -60°C. To meet such requirements, we have developed advanced welding consumables for shielded metal arc welding (SMAW), submerged arc welding (SAW) and flux-cored arc welding (FCAW). For SMAW and SAW consumables, the basicity of the flux was adjusted to reduce the oxygen content in the weld metal, thereby achieving good impact toughness down to -60°C, a high yield strength of over 500MPa, and a high CTOD value down to -40°C. The FCAW consumable has been improved with optimized deoxidizers and the appropriate addition of Ni and Mn to produce a weld metal having a very fine microstructure, thus achieving both a yield strength of over 690MPa and good impact toughness down to -60°C.*

## Introduction

Recently, oil and natural gas are being more actively developed throughout the world to cope with the increasing energy demand. A rapidly growing number of offshore structures are being built, for example, in Southeast Asia, Korea and China. As the resource exploration area is expanded into deeper areas of the sea and low temperature oceans, the steel used for offshore structures is required to be stronger and tougher. To achieve such high strength, steels having a 0.2% yield strength (YS) of 500MPa to 690MPa are increasingly being used these days instead of the conventional steels of YS460MPa or less. As to the aspect of toughness, recent welded joints are required to have brittle fracture prevention characteristics, in addition to the Charpy impact energy absorption at temperatures from -40°C to -60°C. Therefore, the critical crack tip opening displacement (CTOD) value, as described later, is more often included in the specification requirements for fracture toughness.

This paper describes the recent trend of offshore structures that are built in deeper areas of the ocean, and the high-quality welding consumables developed for the purpose.

## 1. Types of offshore structures

Offshore structures for oil and natural gas are roughly classified into a fixed, bottom-seated type that is directly supported by the ocean floor, and a floating type that is indirectly supported. The bottom-seated type includes a jacket with legs fixed to the ocean floor and an upper structure, including excavating equipment, mounted on the legs, a jack-up drilling rig consisting of fixed legs and an upper structure that is designed to move up and down, and a compliant tower (CT) with flexible legs. The floating type includes a semi-submersible rig (SSR), a tension-leg platform (TLP), a floating production, storage and offloading facility (FPSO) and a SPAR platform. A SPAR platform is a moored type, comprising a lower structure with a hollow cylindrical float and storage capacity. Since the floating type equipment can perform drilling and production in water deeper than the fixed type can, the number of such types has been increasing in recent years as the resources are sought in deeper areas of the ocean. **Table 1** shows the types of major offshore structures, their operating depths in the water and the strength grades of steel used.<sup>1), 2)</sup> As the structure becomes larger, high-strength steels of the YS460 -690MPa classes are increasingly used for weight reduction.

Table 1 Type, operating water depth, and steel grade of offshore structures

Type	Operating water depth <sup>1),2)</sup>	Steel grade
Jacket	<450 m	~YS500
Jack-up rig	30-200 m	~YS690
CT	300-700 m	~YS460
SSR	70->2000 m	~YS690
TLP	300-1500 m	~YS460
FPSO	50->2000 m	~YS460
Spar	300->2000 m	~YS460

## 2. Design concept of offshore structures

The capsizing of Alexander Kielland in 1980<sup>3)</sup> triggered the introduction in the 1980s of elastoplastic fracture mechanics to the design concept in order to improve structural safety. This has raised the need of brittle-crack propagation arrest characteristics for steel plates and brittle-fracture prevention characteristics for welded joints. More

Table 2 Welding consumables for offshore structures requiring low temperature toughness

Welding process	Welding Consumable *1	Minimum applicable strength (MPa) *2		Applicable temperature (°C) *2		Chemical composition of weld metal (mass%)							Polarity or shielding gas
		0.2%YS (MPa)	TS (MPa)	vE	CTOD (δ)	C	Si	Mn	Ni	Mo	Ti	B	
				≧ 47J	≧ 0.25mm or ≧ 0.10mm※								
SMAW	[T] LB-7018-1	400/390 <sup>*3</sup>	520/490 <sup>*3</sup>	-40	0	0.06	0.4	1.5	-	-	0.03	0.004	AC/DCEP <sup>*4</sup>
	[T] LB-52NS	400/390 <sup>*3</sup>	520/490 <sup>*3</sup>	-60	-30	0.08	0.4	1.4	0.5	-	0.02	0.002	
	[T] NB-1SJ	460/400 <sup>*3</sup>	550/520 <sup>*3</sup>	-60	-40	0.08	0.3	1.3	1.3	-	0.02	0.002	
	[T] LB-55NS	470/460 <sup>*3</sup>	570/550 <sup>*3</sup>	-60	-	0.06	0.3	1.5	0.9	0.1	0.01	0.003	
	[T] LB-62L	530/460 <sup>*3</sup>	620/550 <sup>*3</sup>	-60	-10	0.07	0.3	1.0	2.1	0.1	0.02	0.002	DCEP
	[T] LB-67L	530	620	-60	-20	0.06	0.3	1.1	2.6	-	0.01	0.002	
	[T] LB-67LJ	530	620	-60	-40 ※	0.07	0.4	1.1	2.6	-	0.02	0.002	
	[T] LB-88LT	690	770	-60	-	0.04	0.6	1.8	2.6	0.7	-	-	
[T] LB-80L	690	770	-60	-	0.04	0.5	1.4	3.0	0.8	-	-	DCEP	
SAW	[T] PF-H55LT/ [F] US-36	400	520	-60	-50	0.08	0.2	1.4	-	-	0.02	0.004	AC
	[T] PF-H55LT/ [T] US-36J	465	550	-60	-20	0.09	0.3	1.7	-	-	0.02	0.004	
	[T] PF-H55S/ [T] US-2N	530	620	-60	-20	0.08	0.3	1.3	2.3	0.2	-	-	
	[T] PF-H80AK/ [T] US-80LT	690	770	-60	-	0.08	0.3	1.7	2.5	0.7	-	-	DCEP
	[T] PF-H55AS/ [T] US-36J	400	520	-60	-20	0.07	0.2	1.4	-	-	0.02	0.004	
	[T] PF-H62AS/ [T] US-2N	530	620	-60	-20	0.05	0.3	1.3	2.5	0.2	0.01	-	
	[T] PF-H80AS/ [T] US-80LT	690	770	-60	-	0.06	0.5	1.6	2.4	0.7	-	-	
GMAW (Solid)	[T] MG-S50LT	400	520	-60	-30	0.09	0.4	1.9	-	-	0.08	0.006	80%Ar-20%CO <sub>2</sub>
	[T] MG-S88A	690	770	-60	-	0.06	0.5	1.6	3.6	0.8	-	-	
GMAW (FCW)	[T] DW-55L	400	520	-60	0	0.04	0.4	1.3	1.4	-	0.05	0.003	CO <sub>2</sub>
	[T] DW-55LSR	420	550	-60	-10	0.06	0.3	1.2	1.5	-	0.05	0.004	
	[T] DW-62L	500	610	-60	-40 ※	0.06	0.3	1.2	2.5	-	0.06	0.004	
	[T] DW-A81Ni1	420	550	-60	-10	0.05	0.3	1.3	0.9	-	0.04	0.005	80%Ar-20%CO <sub>2</sub>
	[T] DW-A55L	460	550	-60	-20	0.06	0.3	1.2	1.4	-	0.06	0.003	
	[T] DW-A55LSR	420	550	-60	-20	0.05	0.3	1.3	0.9	-	0.04	0.003	
	[T] DW-A62L	500	610	-60	-40 ※	0.07	0.3	1.3	2.1	-	0.04	0.003	
[T] DW-A80L	690	770	-40	-	0.07	0.3	1.9	2.5	0.2	0.07	-		

\*1 [F]: FAMILIARC™ welding consumables, [T]: TRUSTARC™ welding consumables

\*2 For as-welded state (no post weld heat treatment)

\*3 The left value is for AC (alternate current) welding and the right value is for DCEP (direct current electrode positive) welding.

\*4 Chemical compositions of LB-52NS, NB-1SJ and LB-62L weld metals are for AC current, others are for DCEP current.

specifically, critical CTOD values were additionally required as fracture toughness criteria, especially for offshore structures.

The CTOD testing involves a specimen with a fatigue precrack, in which the precrack is opened by bending or tension to measure the crack opening displacement at the time when unstable fracture begins. The critical CTOD value indicates the opening displacement at the crack tip when the unstable fracture begins, or, when no unstable fracture occurs, indicates the crack tip opening displacement at the maximum load. In general, an offshore structure requires a critical CTOD value of 0.10mm to 0.25mm or even greater at temperatures from 0 to -10°C; however, lately more stringent requirements at temperatures from -30 to -40°C are being seen.

### 3. Welding consumables for offshore structures

For the welding of offshore structures, welding consumables of various strength classes are used for steel grades of the YS320 - 420MPa class, the YS460 - 500MPa class and the YS690MPa class. These welding consumables include the materials approved by classification societies for general shipbuilding; however, qualities other than those approved are often required to satisfy the design requirements unique to offshore structures, such

as applications in intensely cold sea, thicker structural members and the use of high-strength steel. In particular, the stringent requirement for low temperature toughness has led to having the offshore structures welded using consumables designed for steel used at low temperatures.

Table 2 shows typical welding consumables manufactured by Kobe Steel for the low-temperature specifications of offshore structures. The majority of materials in this table satisfy the Charpy impact performance requirements down to approximately -60°C. With the exception of the materials for YS690MPa class steel and a few others, they also satisfy the CTOD requirements down to temperatures of -10°C or lower.

## 4. Design guidelines for weld metal with high toughness

### 4.1 Techniques for improving the toughness of weld metal

The following measures are effective in improving the toughness of weld metals: ① toughening the ferrite, ② refining the microstructure by lowering the transformation temperature, and ③ forming a fine needle-like microstructure consisting of acicular ferrite by introducing intragranular nucleation sites such as oxide. These are common

Table 3 Method to improve toughness of weld metal

Aim	Method	
	$\leq$ YS500	$\geq$ YS600
Toughening matrix	Addition of Ni	Increase of Ni
Refinement of microstructure	Addition of Mo Reduction of O	Reduction of O
Formation of acicular ferrite	Addition of Ti and B	Introduction of nucleation site (Ti oxide, etc.)

approaches for increasing toughness regardless of the strength.

Meanwhile, regarding the microstructures of weld metals, the weld metal of YS500MPa or lower has a microstructure mainly consisting of ferrite + pearlite, while the weld metal of YS600MPa or higher has a microstructure mainly consisting of bainite + martensite. Therefore, in order to design welding consumables for low-temperature specifications, taking account of toughness, the basic composition design of the weld metal should be fairly different below and above the strength boundary of YS500 - 600MPa. **Table 3** shows the method for improving toughness in accordance with strength. Currently, Ti and B are added in combination to the weld metal in the strength class of YS500MPa or lower to suppress the grain boundary ferrite while promoting the formation of acicular ferrite. On the other hand, an increased amount of Ni is mainly added to the weld metal of YS600MPa or higher to toughen the ferrite and refine the microstructure. Another common approach is to reduce the oxygen in the weld metal.

#### 4.2 CTOD design technique

When developing welding consumables, it is not practical to conduct a CTOD test on each and every trial material, due to the long time and high cost of testing. So, a technique was devised for predicting the results of CTOD testing from a simple Charpy impact test, using the relationship depicted in **Fig. 1**. The horizontal axis represents the ratio of the area occupied by brittle fracture surface after the Charpy impact test, while the vertical axis represents the occurrence probability of different fracture modes in the CTOD test. It should be noted that the testing temperature for the Charpy impact test contemplates the temperature shift ( $\Delta T$ ) caused by the thickness effect.<sup>4)</sup> Each plot represents values measured by the Charpy impact test and the CTOD test for various thicknesses and heat inputs, while each curve is an approximation of relevant measured values. This figure indicates that, in order to avoid unstable fracture (c-mode) and to achieve either perfectly ductile fracture (m-mode), or unstable

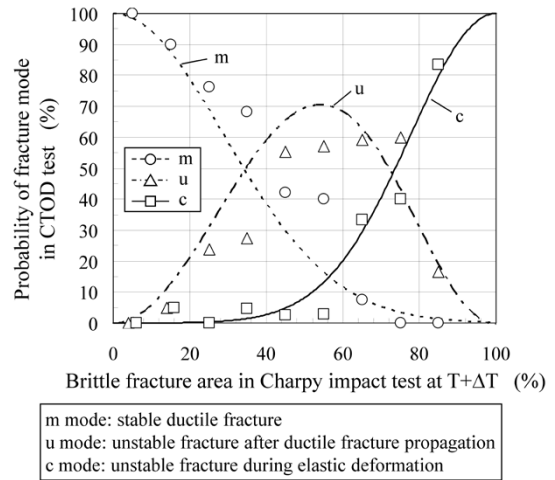


Fig. 1 Relationship between brittle fracture area in Charpy impact test and probability of occurrence of fracture mode in CTOD test

fracture after stable and ductile crack propagation (u-mode), the brittle fracture surface ratio after the Charpy impact test must be approximately 40% or smaller.

#### 5. Development of covered electrode for YS500MPa class steel<sup>5)</sup>

In response to the need for improved toughness of the weld metal for YS500MPa class steel, an electrode has been developed for shielded metal arc welding (SMAW) that satisfies the CTOD value at  $-40^{\circ}\text{C}$ .

##### 5.1 Development concept

The target specifications of the development have been set to include a yield strength of 500MPa or higher, a plate thickness of 50 - 60mm and a critical CTOD value at a testing temperature of  $-40^{\circ}\text{C}$  of 0.10mm or higher. To estimate the CTOD value at  $-40^{\circ}\text{C}$ , the test temperature of the Charpy impact testing was set to be  $-74^{\circ}\text{C}$ , contemplating the temperature shift of  $-34^{\circ}\text{C}$  for the plate thickness of 50mm.

High toughness was ensured mainly by the reduction of oxygen content in the weld metal. In the case of SMAW materials, the oxygen content in the weld metal can be controlled by adjusting

the basicity (BL) of the covering material. Fig. 2 shows the relationship between the oxygen content in weld metals, prepared with adjusted basicity, and the brittle fracture surface ratio at the testing temperature of  $-74^{\circ}\text{C}$ . As shown, the oxygen content in the weld metal must be kept at 200ppm or lower to reliably satisfy the brittle fracture surface ratio of 40% or lower.

In addition to the above basicity adjustment, the Si content in the weld metal has been optimized to decrease the brittle fracture surface ratio. Fig. 3 shows the relationship between the Si content in the weld metal and the brittle fracture surface ratio at  $-74^{\circ}\text{C}$ . The values inside this figure represent the oxygen content in the weld metal. When the Si content is 0.4% or higher, solid-solute Si embrittles the matrix, increasing the brittle fracture surface ratio; whereas, when the Si content is 0.4% or lower, the oxygen content is increased as a result of the lowered deoxidation effect of Si, which results in an increase in the brittle fracture surface ratio. Therefore, the developed material is adjusted such that the Si content in the weld metal reaches the optimum value of approximately 0.4%.

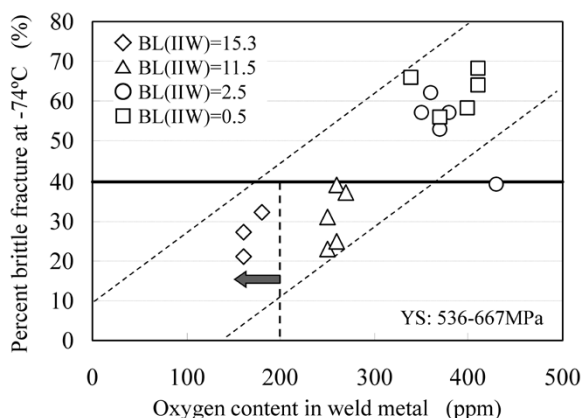


Fig. 2 Relationship between oxygen content in weld metal and percentage of brittle fracture at  $-74^{\circ}\text{C}$  for Charpy impact test (SMAW)

## 5.2 Mechanical properties of weld metal

The newly developed wire, "LB-67LJ," was used to prepare a welded joint, and the weld metal was subjected to tensile and Charpy impact tests. The results are shown in Table 4. Similar joints were used to evaluate the relationship between the welding heat input and the critical CTOD value at the test temperature of  $-40^{\circ}\text{C}$ . The results are shown in Fig. 4. The both-side welding was done

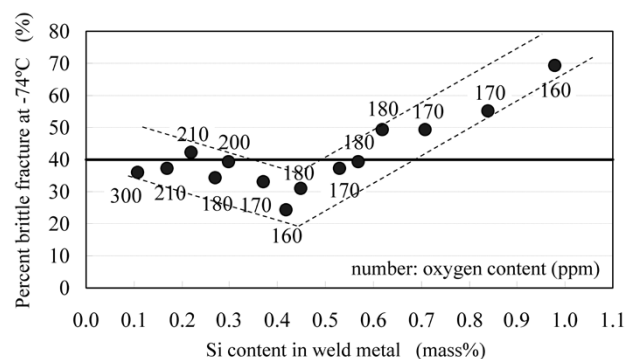


Fig. 3 Relationship between Si content in weld metal and percentage of brittle fracture at  $-74^{\circ}\text{C}$  for Charpy impact test (SMAW)

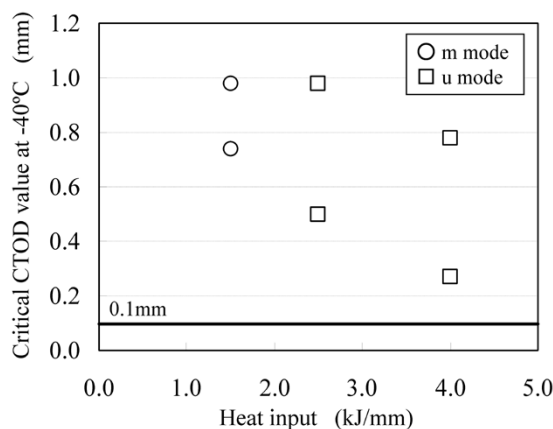


Fig. 4 Relationship between heat input and critical CTOD value at  $-40^{\circ}\text{C}$  of welded joint with LB-67LJ

Table 4 Mechanical properties of welded joint with LB-67LJ

Plate thickness	Welding position	Heat input (kJ/mm)	Location <sup>*3</sup>	Tensile properties <sup>*1</sup>			Notch toughness <sup>*2</sup>			
				0.2%YS (MPa)	TS (MPa)	El. (%)	Absorbed energy: J (Brittle fracture: %)			FATT (°C)
							-80°C	-60°C	-40°C	
60mm	Horizontal (2G)	1.5	F	627	687	22	172 (15)	189 (3)	192 (1)	<-80
			B	640	708	25	146 (17)	186 (7)	197 (0)	<-80
	Flat (1G)	2.5	F	578	669	27	130 (18)	146 (13)	170 (5)	<-80
			B	550	650	28	82 (33)	152 (18)	160 (6)	<-80
	Vertical upward (3G)	4.0	F	576	668	23	107 (25)	141 (14)	153 (5)	<-80
			B	573	696	26	85 (38)	149 (7)	163 (4)	<-80

\*1 JIS Z 3111 No.A2 specimen (dia.=6.0mm, G.L.=24mm)

\*2 Charpy impact test specimen: 10mm × 10mm, 2mm V-notch

\*3 F: 7mm from 2nd side surface, B: 7mm from 1st side surface

on a 60mm thick plate with a double-V groove. The strength of the weld metal satisfies  $YS \geq 500\text{MPa}$  with its Charpy absorption energy being sufficiently high compared with the value, 50J, required for this strength class by ship classification societies. In addition, a critical CTOD value of 0.25mm or higher was obtained even at the welding heat input of approximately 4.0kJ/mm with all the fractures occurring in either m-mode or u-mode.

## 6. Submerged arc welding material for YS500MPa class steel <sup>6)</sup>

A submerged arc welding (SAW) material has been developed using bonded flux as a base with the targets of a yield strength of 500MPa or higher and a critical CTOD value at  $-40^\circ\text{C}$  of 0.10mm or greater.

### 6.1 Development concept

As in the case of the SMAW material described in the previous section, the reduction of oxygen content in the weld metal is mainly used as a technique to achieve high toughness in the weld metal. Several

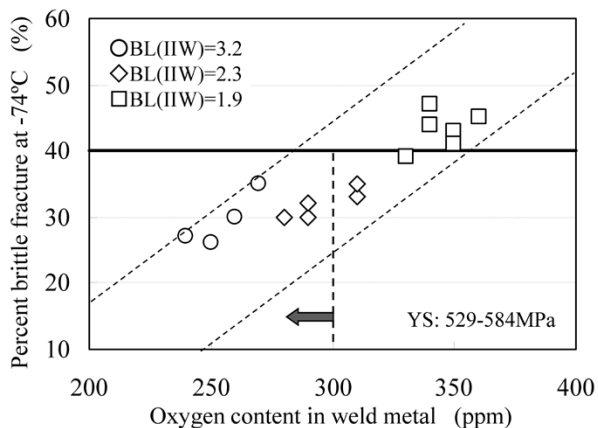


Fig. 5 Relationship between oxygen content in weld metal and percentage of brittle fracture at  $-74^\circ\text{C}$  for Charpy impact test (SAW)

test materials with various flux compositions were prepared to investigate the oxygen content in the weld metal and the brittle fracture surface ratio at the test temperature of  $-74^\circ\text{C}$  (Fig. 5). The weld metal of SAW material has an oxygen content of approximately 300ppm or lower and has achieved a brittle fracture surface ratio of 40% or lower at  $-74^\circ\text{C}$ . In the case of SAW, however, the decreased content of oxygen in the weld metal tends to cause the deterioration of the bead shape. The oxygen content has therefore been adjusted to approximately 280ppm to balance the welding workability and toughness.

### 6.2 Mechanical properties of weld metal

The newly developed SAW material was used to prepare a welded joint and the weld metal was subjected to tensile and Charpy impact tests. The results are shown in Table 5. The relationship between the welding heat input and the critical CTOD value at the test temperature of  $-40^\circ\text{C}$  is shown in Fig. 6. The joint is a double-V groove made of the plates of 60mm thick. Similar to the test

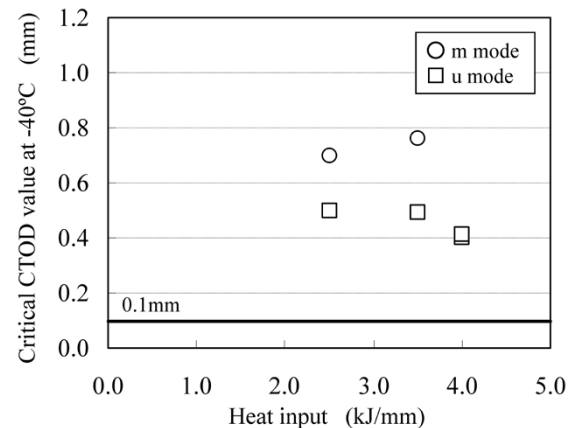


Fig. 6 Relationship between heat input and critical CTOD value at  $-40^\circ\text{C}$  of welded joint with developed SAW consumable

Table 5 Mechanical properties of welded joint with developed SAW consumable

Plate thickness	Welding position	Heat input (kJ/mm)	Location <sup>*3</sup>	Tensile properties <sup>*1</sup>			Notch toughness <sup>*2</sup>			
				0.2%YS (MPa)	TS (MPa)	El. (%)	Absorbed energy: J (Brittle fracture: %)			FATT (°C)
							-80°C	-60°C	-40°C	
60mm	Flat (1G)	2.5	F	557	662	32	66 (38)	108 (25)	166 (8)	<-80
			B	547	649	31	60 (44)	104 (24)	137 (11)	<-80
		3.5	F	532	674	30	51 (45)	83 (25)	137 (12)	<-80
			B	568	656	30	55 (44)	112 (24)	158 (6)	<-80
		4.0	F	532	674	30	51 (45)	83 (25)	137 (12)	<-80
			B	568	656	30	55 (44)	112 (24)	158 (6)	<-80

\*1 JIS Z 3111 No.A2 specimen (dia.=6.0mm, G.L.=24mm)

\*2 Charpy impact test specimen: 10mm × 10mm, 2mm V-notch

\*3 F: 7mm from 2nd side surface, B: 7mm from 1st side surface

results for the SMAW material, the strength of the weld metal satisfies  $YS \geq 500\text{MPa}$ , with its Charpy absorption energy greatly exceeding 50J down to  $-60^\circ\text{C}$ . The critical CTOD value at  $-40^\circ\text{C}$  is as high as 0.40mm or greater at the heat input of 4.0kJ/mm, with all the fractures occurring in either m-mode or u-mode.

## 7. Development of flux-cored wire for YS690MPa class steel<sup>7)</sup>

Conventionally, SMAW materials have mainly been used for the all-position welding of high-strength steel; however, there is an increasing demand for the use of flux-cored wire (FCW) in order to improve the efficiency of welding work and to deskill the work. We have therefore developed an FCW for all-position welding, applicable to the YS690MPa class steel that is often used for offshore structures such as jack-up rigs. As described above, increasingly stringent toughness requirements are being imposed on the welding consumables used in offshore structures. The major issue in developing welding consumables for high-strength steel, such as the YS690MPa class, is to achieve both strength and toughness simultaneously.

### 7.1 Development concept

Reducing the oxygen content in weld metal works well in improving toughness in the case of FCWs, too. Titania-based FCWs are mainly used for the all-position welding of steels of the YS500MPa class or lower. The FCWs designed for high-strength steel up to the YS690MPa class are likely to yield favorable welding workability. However, the weld metal formed of titania-based FCW tends to exhibit high oxygen content, making it difficult to achieve favorable toughness as the strength increases. Meanwhile, the FCW suffers from the fact that welding workability in the vertical position is deteriorated if the basicity of the flux is increased in order to reduce the oxygen content, as is done for SMAW and SAW materials, which makes the FCW inapplicable to all-position welding.

**Fig. 7** shows the relationship between the number density of oxide in the weld metal of the FCW for high-tensile steel (YS550MPa class) and upper shelf energy ( $vE\text{-Shelf}$ ) measured by the Charpy impact test. As shown, the  $vE\text{-Shelf}$  value tends to decrease with the increasing number density of oxide. **Fig. 8** shows the relationship between the bainite grain size of weld metal and fracture appearance transition temperature (FATT) measured by the Charpy impact test. As shown, the refining

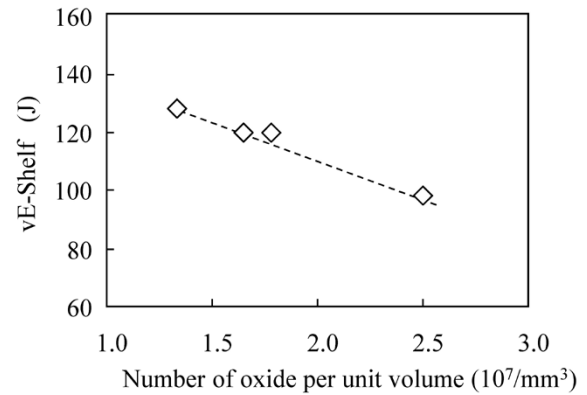


Fig. 7 Relationship between number density of oxide and upper shelf energy ( $vE\text{-Shelf}$ )

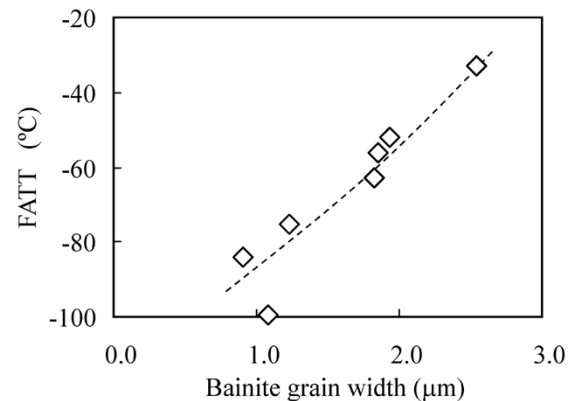


Fig. 8 Relationship between grain size of bainite and fracture appearance transition temperature (FATT)

bainite grain is effective in decreasing the FATT. In other words, in the case of FCW weld metal for high-tensile steel, suppressing the number density of oxide and promoting intragranular bainite transformation to refine the microstructure is considered to provide favorable toughness. In the case of the newly developed wire, the toughness is improved by optimized deoxidizer, which suppresses the amount and number density of oxide in the weld metal, and the addition of mainly Ni and Mn, which lowers the bainite transformation temperature and thus refines the microstructure.

### 7.2 Microstructure morphology

**Fig. 9** shows the microstructure (left) of the weld metal made of a newly developed wire, DW-A80L, and the orientation map (right) obtained by electron backscatter diffraction (EBSD) analysis. Intragranular bainite is observed across the entire surface, forming an extremely fine microstructure. The microstructure size measured on the basis of the orientation map is approximately  $1.66\mu\text{m}$ . **Fig.10** is the result of optical microscopic observation of oxide in the weld metal made of DW-A80L. The number

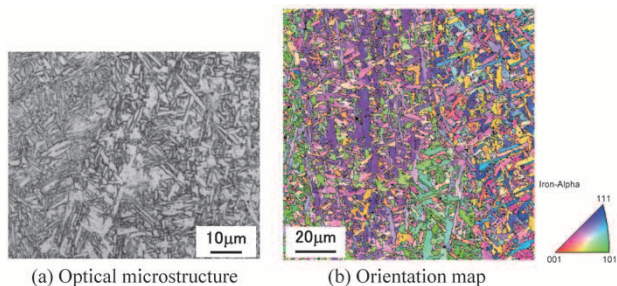


Fig. 9 Microstructure of weld metal and EBSD orientation map

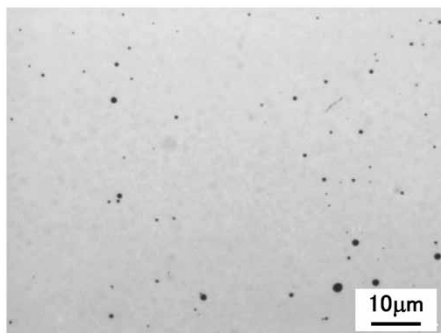


Fig.10 Optical micrograph of oxide in weld metal

density of oxide, obtained by image processing, is approximately  $1.3 \times 10^7/\text{mm}^3$ .

### 7.3 Mechanical properties of weld metal

Table 6 shows the results of tensile and Charpy impact tests of weld metal made by using DW-A80L. The welding was done on both sides of 50mm thick plate with a double-V groove. The strength of the weld metal satisfies the specification required for

the YS690MPa class, and the refined microstructure keeps the fracture appearance transition temperature (FATT), as measured by the Charpy impact test, at a temperature of  $-60^\circ\text{C}$  or lower, suppressing the reduction in absorption energy.

### 7.4 Cold cracking resistance of weld metal

The welding of high-tensile steel, such as the YS690MPa class, often poses problems with cold cracking caused by hydrogen entering the molten metal during welding; so the cold cracking resistance of the weld metal made from the newly developed wire has been evaluated. The evaluation was conducted by a window-type, restrained weld cracking test on a Y groove joint with a plate thickness of 50mm. This test involves fixing the test plate by all-around, multi-layer fillet welding on a constraint plate (thickness 100mm) to ensure a high constraint force, and subsequently welding in the groove, such that the severely constrained state of actual structures is reproduced.

Table 7 shows the welding conditions and cracking test results. The existence of crack was checked by an ultrasonic test (UT) on the weld metal and a magnetic-particle test (MT), the latter test being conducted intermittently while cutting the weld metal. The lowest preheat and interpass temperature to prevent cold cracking is determined to be  $50^\circ\text{C}$  or lower for the welding heat input of  $1.7\text{kJ}/\text{mm}$ , and  $75^\circ\text{C}$  for the welding heat input of  $1.0\text{kJ}/\text{mm}$ . This wire is designed for reduced hydrogen to realize a favorable cold cracking resistance.

Table 6 Mechanical properties of welded joint with DW-A80L

Plate thickness	Welding position	Heat input (kJ/mm)	Location <sup>*3</sup>	Tensile properties <sup>*1</sup>			Notch toughness <sup>*2</sup>			
				0.2%YS (MPa)	TS (MPa)	El. (%)	Absorbed energy: J (Brittle fracture: %)			FATT (°C)
							-60°C	-40°C	-20°C	
50mm	Horizontal (2G)	0.9	F	784	825	20	67 (14)	74 (6)	75 (4)	<-60
			B	818	848	22	66 (14)	73 (9)	77 (7)	<-60
	Vertical upward (3G)	1.7	F	736	811	23	52 (39)	68 (32)	79 (22)	<-60
			B	738	817	24	62 (29)	72 (22)	83 (18)	<-60

\*1 JIS Z 3111 No.A2 specimen (dia.=6.0mm, G.L.=24mm)

\*2 Charpy impact test specimen: 10mm × 10mm, 2mm V-notch

\*3 F: 7mm from 2nd side surface, B: 7mm from 1st side surface

Table 7 Results of window type restrained weld cracking test

Plate thickness	Welding position	Welding current (A)	Arc voltage (V)	Heat input (kJ/mm)	Minimum preheat and interpass temp. to prevent cold cracking
50mm	Flat (1G)	280	29	1.7	$\leq 50^\circ\text{C}$
	Horizontal (2G)	280	29	1.0	$75^\circ\text{C}$

## Conclusions

This paper has described the recent trend of offshore structures, upsized and used in deeper areas of the ocean, and the development of high-strength, high-toughness welding consumables to satisfy the needs of these structures. Currently, Kobe Steel has a line-up of welding consumables to satisfy most needs. We are committed to respond to requirements for even higher strength, toughness and efficiency. We will strive to develop new welding technologies, on the basis of various approaches, and welding consumables based on the new technologies.

## References

- 1) K. Sekita. Offshore Structure. Seizando, 2002, p.8-25.
- 2) Japan Oil, Gas and Metals National Corporation (JOGMEC). Offshore technology Handbook. 2011.
- 3) H. Yajima. Journal of the Japan Welding Society. 1999, Vol.68, No.7, p.503.
- 4) The Japan Welding Engineering Society. WES 2805, Method of Assessment for Flaws in Fusion Welded Joints with Respect to Brittle Fracture and Fatigue Crack Growth. 2007, p.103
- 5) P. Han et al. Preprints of the National Meeting of JWS. 2009, Vol.85, p.358-359.
- 6) P. Han et al. Preprints of the National Meeting of JWS. 2010, Vol.87, p.192-193.
- 7) Y. Okazaki et al. Quarterly Journal of the Japan Welding Society. 2009, Vol.27, No.2, p.131-138.

# Robot Welding Process for Medium and Heavy Plate

Katsuyuki TSUJI\*1, Akira OGAWA\*1, Dr. Kei YAMAZAKI\*2, Yimin YUAN\*2

\*1 Welding System Dept., Technical Center, Welding Business

\*2 Welding Process Dept., Technical Center, Welding Business

*Welding processes are always required to have high-efficiency, quality stability, and reduced costs. The advanced controllability of the welding power sources has enabled the control of the output waveform, using an advanced control law, which has realized a new process with high added value for medium and heavy plates, the Ultra-High Current GMAW process, tandem arc welding and "REGARC™". The Ultra-High Current GMAW process is a highly-efficient welding process using single arc and offers large leg length, low-spatter and deep penetration, using special flux-cored wire and unique waveform control. Tandem arc welding reduces spatter generation by 70 percent compared with conventional equipment, thanks to its new waveform control. The advantage of this welding process is a high deposition rate and high speed welding. "REGARC™" reduces spatter generation by 90 percent compared with the conventional process using CO<sub>2</sub> gas-shielded arc welding.*

## Introduction

Semi-automatic welding has been used more frequently in the field of medium and heavy plate welding, which requires a more sophisticated level of technology than that required for the thin sheet welding used, for example, in the automotive field. Recently, however, robotic welding is being increasingly used to improve welding efficiency, to compensate for the lack of skilled workers and to stabilize the quality. In such circumstances, higher efficiency, faster welding, lower spatter and lower cost are always being pursued, increasing the desire for new welding processes.

In 2010, Kobe Steel began selling SENSARC™, note 1) AB500 (hereinafter, AB500), a digitally controlled power source exclusively designed for welding robots (Fig. 1).



Fig. 1 Appearance of SENSARC AB500

Table 1 Summary of newly developed welding process

	Welding wire	Shielding gas	Characteristics
Ultra high current GMAW Process	FAMILIARC™ MX-A100D φ 1.4mm	Ar+20%CO <sub>2</sub>	One electrode High-deposition rate Big leg length Low spatter
Tandem arc Welding	FAMILIARC™ MG-50R φ 1.2mm	Ar+20%CO <sub>2</sub>	Two electrodes High-deposition rate High-speed welding
REGARC™	FAMILIARC™ MG-50REG φ 1.1mm	100%CO <sub>2</sub>	Low spatter Low gas cost

This power source has improved control capability compared with the conventional machines, enabling the control of output waveform in accordance with high-level control laws. This has made it feasible to implement various welding modes that have been difficult when using the conventional machines and to develop welding processes with high added value.

This paper introduces three welding processes with high added value made possible by the improved functions of AB500 (Table 1). The first process is a type of gas metal arc welding (GMAW), named the "Ultra-High Current GMAW", which has enabled high current and high deposition with one electrode; the second is "tandem arc-welding", a high-deposition high-speed welding process using two electrodes, which has significantly reduced spatter compared with the conventional process; and the last is REGARC™, note 2), which has enabled extremely low spatter despite being a CO<sub>2</sub> welding process.

## 1. Welding system for Ultra-High Current GMAW<sup>1), 2)</sup>

### 1.1 Background

Recently, in fields involving the use of medium to thick plates, as is the case, for example, with construction machinery, there has been a strong need to improve efficiency by increasing the deposition rate with one electrode and thus improving operability. In response to this need, Kobe Steel began selling a welding system for the Ultra-High Current GMAW in October 2012. This section describes the Ultra-High Current GMAW system and explains the effects of its introduction, giving examples of its installation.

note 1) SENSARC (SENSARC™) is a trademark of Kobe Steel.

note 2) REGARC (REGARC™) is a trademark of Kobe Steel.

## 1.2 Exclusive flux-cored wire, FAMILIARC™, note 3) MX-A100D

The major issue with the conventional high-current welding using carbon steel solid wire is the spatter generation caused by rotating transfer.<sup>3)</sup> This is due to the wire extension that is melted by resistance heat, loses its rigidity before it reaches the arc generation point and is rotated by the electromagnetic force to scatter the droplet.<sup>4)-6)</sup> We therefore focused on the possibility that the flux portion of a flux-cored wire (FCW) plays the role of a "column" that prevents this rotation. The inner flux of an FCW allows almost no welding current to flow through it, making the outer metal sheath, the outer portion of the wire, melt first even with an increased current density, while the flux portion maintains its columnar shape. This, as a result, enables spray transfer in which the molten portion of the wire tip does not rotate (**Fig. 2**).<sup>4)-6)</sup> In addition, the flux was designed for high current welding with optimized characteristics including resistance against nitrogen pick-up and slag formation. This has led to the development of FAMILIARC MX-A100D, an FCW exclusively designed for the Ultra-High Current GMAW. **Table 2** shows, as an example, the chemical composition and mechanical properties of a weld metal deposited by this wire.

## 1.3 Control of current, voltage and waveform by AB500

As described, the FCW wire configuration can prevent rotating transfer in the wire melting phenomenon and achieves stable spray transfer. However, when welded with a general constant voltage characteristic, the wire results in irregular variation of the arc voltage and arc length as shown in **Fig. 3**. It has been confirmed that this is caused by the fact that the outer metal sheath in the wire extension is melted by excessive arc heat and Joule heat before it reaches the arc generation point, making it difficult for the wire to maintain its shape and causing it to drop irregularly.<sup>4)-6)</sup>

In order to improve this phenomenon, waveform controls of the welding current and arc voltage have been adapted to stabilize the molten state of the wire extension. As a result, an exclusively designed waveform control incorporating low-current periods provided cyclically to suppress the heat input of the arc heat and Joule heat to the wire has enabled the stabilization of the arc length.

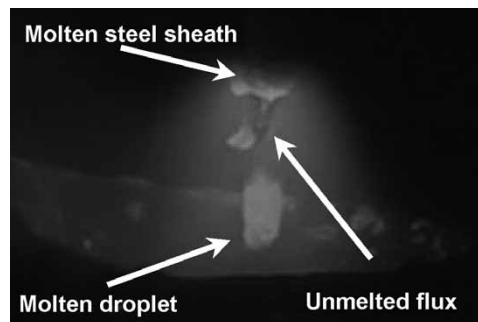


Fig. 2 Observation of droplet transfer using the developed process

Table 2 Chemical compositions and mechanical properties of weld metal

C	Si	Mn	P	S	YS (MPa)	TS (MPa)	El. (%)
0.06	0.81	1.61	0.01	0.007	482	604	25

Welding condition : 500A, 39V, 60cm/min, 4layers-8passes

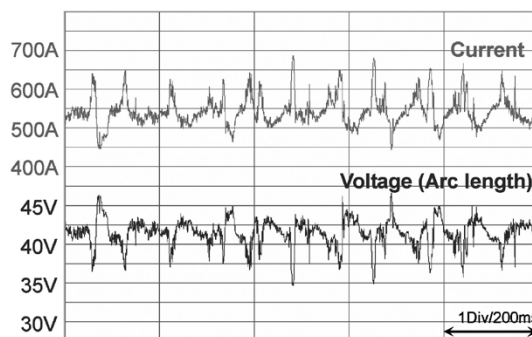


Fig. 3 Current and voltage waveforms in unstable welding arc with non-pulsed constant-voltage power source

## 1.4 Configuration of the welding system for implementing Ultra-High Current GMAW

**Fig. 4** is a schematic diagram showing the configuration of the system for the Ultra-High Current GMAW. The specifications of the system are shown in **Table 3**.

### 1.4.1 AB500 parallel operation system

In order to weld with a current exceeding 500A, the welding power source must output more power than a conventional machine. Therefore, two AB500s, each capable of outputting 500A, have been connected in parallel so as to divide the total output current in half and achieve a high maximum output current of 700A with a utilization of 100%.

The welding power sources have been allocated to a master and a slave such that the master, receiving a command from the robot control panel, sends the command to the slave in order to control it. Thus, like the conventional panel, the robot control panel still controls only one welding power source. Therefore

note 3) FAMILIARC (FAMILIARC™) is a trademark of Kobe Steel.

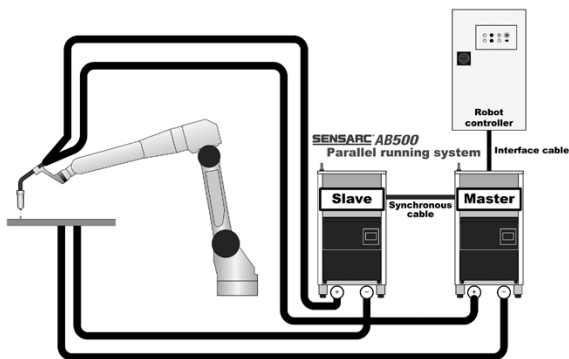


Fig. 4 Configuration sketch of Ultra-High current GMAW Process welding system



Fig. 5 Appearance of RTW601

Table 3 Specifications of Ultra-High current GMAW Process welding system

Manipulator		ARCMAN MP, XL
Welding power source SENSARC™ AB500 Parallel system	Rated output current	700(A)
	Usage rate	100(%)
	Load voltage	55(V)
Maximum wire feed rate		30.0(m/min)
Welding torch for Ultra high current welding RTW601	Rated current	600(A)
	Usage rate	100%(Ar+20%CO <sub>2</sub> )
	Application of wire diameter	1.4(mm)
	Cooling method	Water-cooling
Welding wire	Brand	FAMILIARC MX-A100D
	Wire diameter	1.4(mm)
	Maximum deposition rate	Approximately (300g/min)
Shielding gas		Ar+20%CO <sub>2</sub>

the users need not concern themselves about the fact that two power sources are running, but can operate the system in the same manner as they would operate a single welding power source.

#### 1.4.2 Welding torch, RTW601, for high current

Major problems arising in a welding torch with increased current include the heat generated by the electrical resistance of the power cable and increased radiant heat of the arc. In response, Kobe Steel has developed a new welding torch for high current, RTW601 (Fig. 5).

As a measure against resistance heat generation in the power cable, the two welding power sources are connected by conventionally used power cables to a power supply port of the torch, in which the cables from each power source take separate paths to suppress heat generation as well as to facilitate heat release (Fig. 4).

Increased current enhances the heat radiated from the arc, making the peripheral temperature of the contact tip higher than that hitherto achieved in an arc atmosphere of 600A. Once the temperature of the contact tip becomes too high, the wear of the tip itself is accelerated, which destabilizes the power supply to the wire, increasing the scattering of spatter, and spoiling the appearance of the bead. Therefore, in order to maximize the effect of the improved efficiency

of the Ultra-High Current GMAW, while minimizing the frequency and times of the contact tip changes, it is essential to suppress the temperature rise of the contact tip. To increase its heat releasing efficiency, the RTW601 has increased contact area between its water-cooled tip body and contact tip, as well as an enlarged tip shape and increased inner diameter to increase the surface area. This has achieved wear resistance, in terms of the amount of molten metal, comparable with or better than that achieved by the conventional process.

### 1.5 Effect of Ultra-High Current GMAW

#### 1.5.1 Reduction in spatter generation rate

Fig. 6 shows the amounts of spatter generated by the conventional process using a solid wire and by the Ultra-High Current GMAW. In the conventional process, a wire melting rate exceeding 150g/min (welding current 450A) triggers rotating transfer, which abruptly increases the spatter generation. In contrast, the Ultra-High Current GMAW maintains stable spray transfer regardless of the welding current, enabling low spatter in the high-current region.

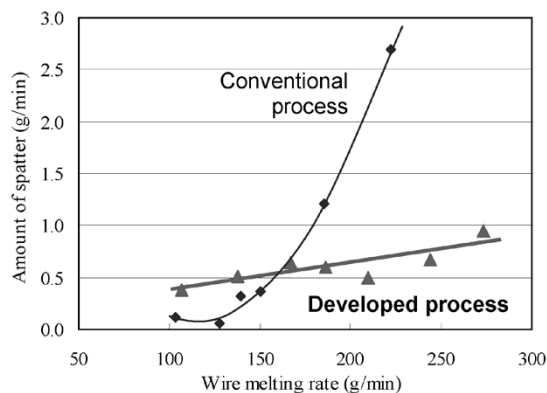


Fig. 6 Comparison of spatter generation rate (Bead on plate) (Welding condition: 1.4mm dia., Ext: 28mm; Ar+20%CO<sub>2</sub>; 60cm/min)

### 1.5.2 Improvement in porosity resistance

Fig. 7 compares the nitrogen content in the welding metal prepared by the conventional process using solid wires with that prepared by the Ultra-High Current GMAW. As described above, the conventional process results in rotating transfer in the high-current region. The softened wire tip is rotated by the magnetic force, which also rotates the arc. Together with this, the shielding gas atmosphere is also agitated and picks up the surrounding air more easily. This is considered to be the cause of the significantly increased nitrogen content in the welding metal. This as a result increases the risk for blowholes at wire melting rates of 200g/min or higher.

Meanwhile, in the case of the Ultra-High Current GMAW, stable spray transfer is achieved even in the high-current region, which minimizes the amount of surrounding air picked up and thus suppresses the nitrogen content of the welding metal. Furthermore, the flux composition of the newly developed wire is designed for resistance against nitrogen pick-up, which prevents porosity defects at a wire melting rate of 300g/min.

### 1.6 Application examples

The following describes examples of the application of the Ultra-High Current GMAW: namely, flat fillet welding and V groove welding. The steel materials used were SS400, and the tip to base-material distance was 28mm.

#### 1.6.1 Flat fillet welding; leg length 15mm; single-pass welding

Table 4 shows the welding conditions for the conventional process and the Ultra-High Current GMAW, Fig. 8 shows their cross-sectional

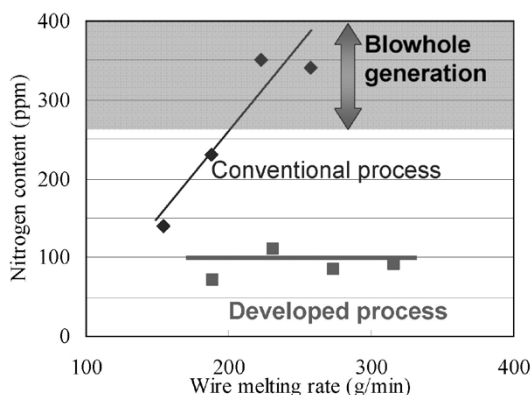


Fig. 7 Comparison of nitrogen content in fillet weld metal (1.4mm dia., Ext: 28mm, Ar+20%CO<sub>2</sub>, 60cm/min)

macrographs, and Fig. 9 shows the appearance of their beads. In order to obtain a leg length of 15mm by the conventional single welding, two-pass welding must be performed. On the other hand, the high deposition rate of the Ultra-High Current GMAW achieves the same leg length with only one pass, the welding efficiency being increased by a factor of 2.4. Despite its high current of 600A, the newly developed process exhibits a clean bead appearance with almost no spatter adhesion. It should be noted that this process has achieved a deep penetration depth of 5.0mm, a depth difficult to achieve using the conventional high deposition process of tandem welding.

#### 1.6.2 50 degree V groove; plate thickness, 16mm; root opening, 5mm

Table 5 shows the welding conditions for the conventional process and the Ultra-High Current GMAW, Fig.10 is a schematic diagram of the welding pass sequence, and Fig.11 shows a cross-sectional

Table 4 Comparison of welding conditions in flat fillet welding

Layers	Conventional process*		Developed process
	1	2	1
Welding current(A)	420	420	600
Deposition rate(g/min)	125	125	268
Welding Speed(cm/min)	34.0	23.0	33.0
Ratio of weld efficiency	1		2.4

\*Solid, 1.4mm dia., MAQ Ext 25mm

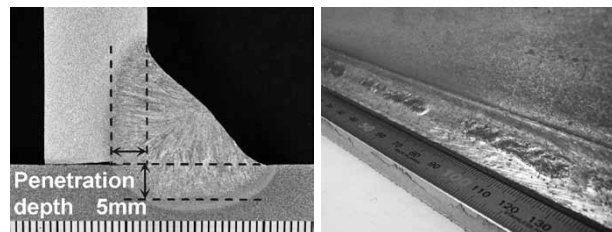


Fig. 8 Macrostructure of cross section Fig. 9 Bead appearance

Table 5 Comparison of welding conditions in single V groove welding

Layers	Conventional process*				Developed process		
	1	2	3	4	1	2	3
Welding current(A)	320	360	360	360	530	530	390
Deposition rate(g/min)	88	101	101	101	255	255	153
Welding speed (cm/min)	32.0	28.0	24.0	19.0	48.0	37.0	25.0
Ratio of weld efficiency	1				1.8		

\*Solid, 1.4mm dia., Ext 25mm

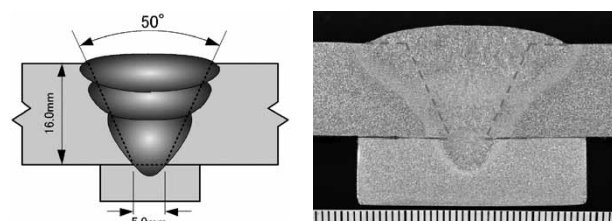


Fig.10 Welding pass sequence Fig.11 Macrostructure of cross section

macrograph. The conventional single welding requires four passes of welding, while the new process reduces the number of passes to three with increased welding speed thanks to its high deposition rate, increasing the welding efficiency by a factor of 1.8.

## 2. Tandem arc welding

### 2.1 Background

In 2001, Kobe Steel started selling a robot system adapting tandem arc welding having two electrodes with one pool to achieve increased welding speed and sound welding bead at the same time. The company continued to develop new technologies with new functions and has achieved improved welding operability by improving the functions of AB500. This section focuses on the newly developed waveform control technology and its effect.

### 2.2 New arc-length control of AB500

#### 2.2.1 Synchronous amplitude modulation control

Tandem arc welding, using two electrodes for generating arcs, adapts pulse welding to reduce spatter; in pulse welding the arc length of the leading electrode is controlled by frequency modulation. In order to suppress arc interference between the two electrodes and improve welding stability, the pulse frequencies of the two electrodes must be synchronized. For this purpose, a conventional machine controls the arc length of its trailing electrode by amplitude modulation of the peak current, rather than by frequency modulation. However, if amplitude modulation based solely on the peak current is adapted, the newly developed process lacks the current required for controlling the arc voltage. This may also cause an inability to maintain the pulse waveform to realize low spatter, a feature of pulse welding, causing difficulty in keeping the desired arc length, increasing spatter.

To deal with this issue, AB500 is equipped with a "synchronous amplitude modulation control", a new way of controlling the arc length of the trailing electrode. The new method controls the arc length by modulating not only the peak current but also the base current (Fig.12). As a result, both the leading and trailing electrodes have greater tolerance for outer disturbance and can maintain their arc lengths within a wider range of conditions. In the case of conventional machines, a change in the welding condition of the leading electrode often causes changes in the welding current and arc length of the trailing electrode. The

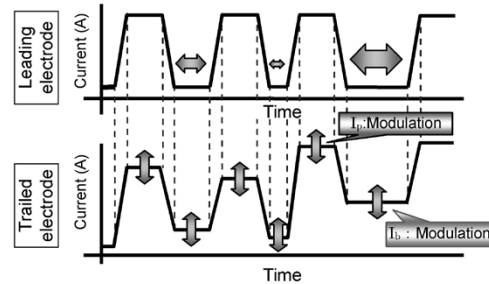


Fig.12 Image of synchronous amplitude modulation control

newly developed control has resolved this issue, facilitating the adjustment of welding conditions.

#### 2.2.2 Advanced load characteristics control (arc length control of the trailing electrode)

In tandem arc welding, it is important that a bulge of molten metal formed between the two arcs be maintained so as to realize arc stability and sound bead shapes (Fig.13).<sup>7)</sup>

In the case of conventional machines, when the state of the molten pool is changed by the arc-length control working against the outer disturbance of the leading electrode, the arc length of the trailing electrode must be fine-tuned for the change. This often causes a further change in the molten pool, which disturbs the bulge of molten metal and destabilizes the arc.

For this reason, Kobe Steel has developed a new "advanced load characteristics control," a type of arc-length control for the trailing electrode. This new control alleviates the effect of outer disturbance on the basis of the moving average of the feedback current, used as a determinant factor for the control target of the arc length, and suppresses the effect of the arc-length control on the molten pool (Fig.14).

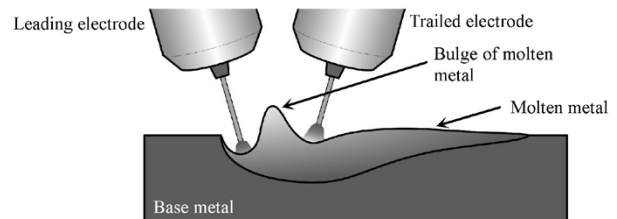


Fig.13 Welding arc and molten metal in tandem arc welding

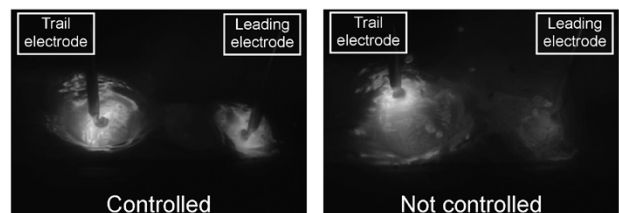


Fig.14 Example of advanced load characteristics control

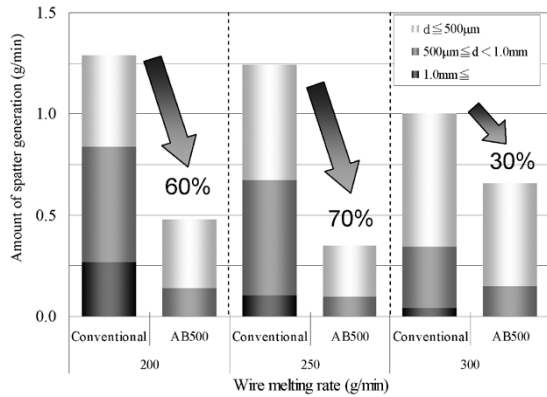


Fig.15 Comparison of spatter generation rate in flat fillet welding

### 2.3 Effects of introducing tandem arc welding (reduced spatter generation rate)

Tandem arc welding using AB500 has remarkably improved the arc stability and welding workability thanks to the two newly developed waveform controls described in section 2.2. It has also significantly reduced the formation of spatter (up to 70% reduction) and decreased the size of the spatter (Fig.15).

## 3. REGARC<sup>®</sup>

### 3.1 Background

Carbon dioxide and argon are mainly used as shielding gas for arc welding, the former having the merit of costing much less than the latter. Conventional carbon dioxide arc welding, however, is inevitably accompanied by large grain spatter. Against this background, Kobe Steel focused on a new droplet transfer control using a special pulse current waveform and has succeeded in the development of a welding system, REGARC, for achieving low spatter by regular droplet formation and detachment.

This section explains the features of the REGARC welding system and the effects of its introduction.

### 3.2 Specifications of REGARC welding system

Table 6 shows the specifications of the REGARC welding system. The FAMILIARC MG-50REG is a new welding wire developed exclusively for REGARC. This wire features excellent feedability with an optimized wire composition and wire

Table 6 Specifications of REGARC welding system

Welding power source	SENSARC AB500
Shielding gas	100%CO <sub>2</sub>
Welding wire	FAMILIARC MG-50REG φ 1.1mm
Maximum wire melting rate	145(g/min)
CTWD	25(mm)
Applicable welding position	Flat fillet, Horizontal fillet

diameter, which has enabled the enlarged range of welding conditions for achieving regular droplet transfer. REGARC has been made possible also by the advanced current voltage waveform control law using the welding power source AB500.

### 3.3 Droplet transfer control in REGARC

In the case of conventional carbon dioxide arc welding, a number of large grains of spatter are generated. This occurs in two ways. In the first case, a droplet becomes short-circuited with the molten pool, causing the arc to be extinguished; and as soon as the short circuit is released and the arc is re-ignited, parts of the droplet and molten pool are blown off (Fig.16 (A)). In the second, the arc is generated in a focused manner at the lower portion of a droplet, which pushes the droplet up in the opposite direction from the arc, making the droplet difficult to detach, and it grows larger. This droplet is further pushed up by the reaction force of the arc and detaches as a spatter of large grains. This phenomenon is generally referred to as globule transfer (Fig. 16 (B)).

To deal with this issue, REGARC prevents the droplet from being pushed up, thanks to its welding current with a special pulsed waveform, at each step of droplet formation and detachment in the process of carbon dioxide arc welding. This has enabled the regular transfer of the droplet into the molten pool before the droplet grows too large, suppressing the short-circuit and scattering of large granular spatter (Fig.17).<sup>9)</sup>

### 3.4 Effect of introducing REGARC

#### 3.4.1 Low spatter

Fig.18 compares the spatter generation rate of conventional carbon dioxide arc welding and REGARC. REGARC resulted in a significantly

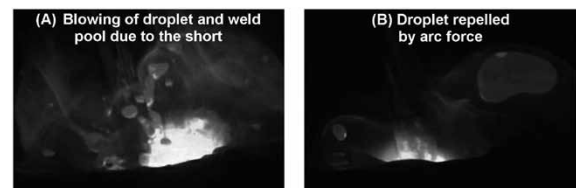


Fig.16 Spatter generation with conventional CO<sub>2</sub> arc welding



Fig.17 Droplet transfer of REGARC

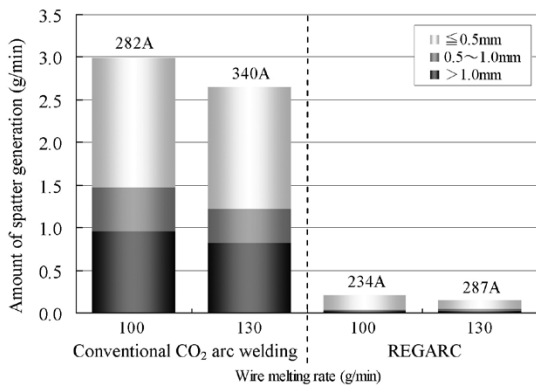


Fig.18 Comparison of spatter generation rate in flat fillet welding

reduced rate of spatter generation, one-tenth of the rate for conventional carbon dioxide arc welding. In addition, the spatter, having a much smaller grain size, is cooled and solidified in the air before it reaches the base material, making it less likely to adhere to the surface of the base material (Fig.19). Hence, users of carbon dioxide arc welding can expect a shortened backend process and improved work environment as benefits of the reduced spatter. Furthermore, those using mixed gas welding to reduce spatter can realize a reduction in cost by switching to the less expensive carbon dioxide.

### 3.4.2 High melting rate / reduced heat input

For any given average current, the wire melting rate of REGARC is 20 to 25% higher than that of conventional carbon dioxide arc welding (Fig.20). This is because REGARC uses a pulse current that has a high effective current and an exclusive wire

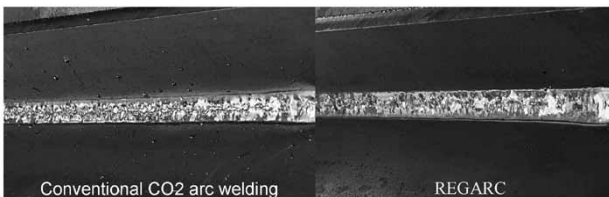


Fig.19 Comparison of adhered spatter in fillet welding

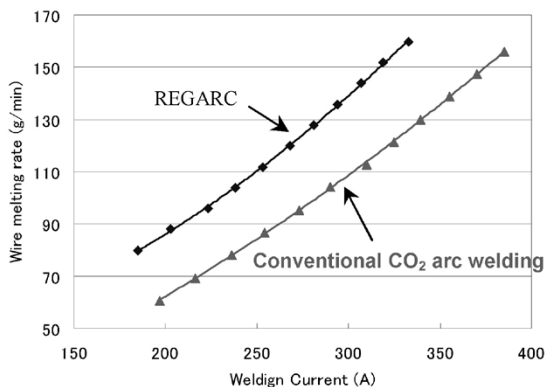


Fig.20 Comparison of wire melting rate

"FAMILIARC MG-50REG". Conversely, the welding current becomes smaller for a given melting rate, which prevents welding deformation due to heat input.

## Conclusions

Three welding processes with high added value for medium to thick plates have been explained. Kobe Steel has lined up tandem arc welding and the Ultra-High Current GMAW for high deposition welding to expand the company's menu of welding processes. These processes have their respective strengths, tandem welding having superior maximum welding speed and the Ultra-High Current GMAW having superior penetration depth with fewer welding deficiencies, enabling their application in accordance with the user's needs. In addition, REGARC has achieved extremely low spatter, something hitherto considered difficult to achieve with general carbon dioxide arc welding. These welding processes are strongly expected to improve the efficiency of welding work for users and their work environment, which eventually leads to cost reduction.

We will strive to provide new welding solutions through various approaches combining welding consumables, application technologies and robot systems.

## References

- 1) K. Tsuji et al. Welding Technology. Sanpo Publications Inc., 2012-11, Vol.60, p.112-117.
- 2) K. Tsuji. Kobe Steel Homepage. Yousetsu-dayori Gijutsu-guide, Gijutsu-report (in Japanese). (Welding News, Technical Guidance, Technical Report) 2012-11, Vol. 52.
- 3) S. Izutani et al. International Institute of Welding 2006. XII Doc. 212-1090-06.
- 4) Y. Yuan et al. Preprints of the National Meeting of JWS 2010-9-7. Japan Welding Society, 2011, p.146-147.
- 5) Y. Yuan et al. "Development of High Current GMAW Process Preventing Rotating Transfer". 214th Technical Commission on Welding Processes, 2011, No. SW-3374-11.
- 6) R. Suzuki. "State of the Arc of Process Control of Molten Droplet and Pool in Gas Metal Arc Welding". Journal of the Japan Welding Society, 2010, Vol.79, No.6, p. 27-33.
- 7) M. Yokota et al. R&D Kobe Steel Engineering Report. 2004, Vol.54, No.2, p.81.
- 8) A. Ogawa. Kobe Steel Homepage. Yousetsu-dayori Gijutsu-guide, Gijutsu-report (in Japanese). (Welding News, Technical Guidance, Technical Report), 2011-12, Vol.51.
- 9) K. Yamazaki et al. Preprints of the National Meeting of JWS 2010-3-29. Japan Welding Society, 2010, p.138-139.

# New Welding Process, "J-Solution™ Zn", Suitable for Galvanized Steel in the Automotive Industry

Shun IZUTANI \*1, Dr. Kei YAMAZAKI \*1, Reiichi SUZUKI \*1

\*1 Welding Process Dept., Technical Center, Welding Business

*In the automotive industry, galvanized steel sheets have been applied for quality improvement. However, the porosity defects generated during welding and increased spattering cause a debasement of welding workability. Porosity-generating behavior, which had not hitherto been clarified, was observed in this study, which also examines a method of reducing both the porosity defects and spatter. The results indicate that releasing zinc vapor from directly under the arc to outside the molten pool is effective in reducing porosity defects. Based on this knowledge, the problem was solved by optimizing (a) the composition and size of the welding material, (b) the shielding gas composition and (c) the current pulse wave pattern. This new welding process was named the "J-Solution Zn".*

## Introduction

Recently, the automotive industry is increasingly using galvanized steel sheets to improve long-term quality and to adapt thinner sheets for weight reduction. Galvanized steel sheets, however, are very poor in weldability compared with ordinary steel sheets. One of their major drawbacks is that the zinc is vaporized during welding, causing porosity defects such as pits that are open onto the weld-bead surface and blowholes that remain inside the beads. Another drawback is that the zinc gas blows off welding droplets and molten pools, which increases the amount of spatter (Fig. 1).

Conventionally, efforts to solve these problems have focused on either the improvement of welding consumables or welding power sources.<sup>1) - 4)</sup> These solutions, however, have not yet been able to resolve the issues of porosity resistance and spatter simultaneously. The porosity defects are considered

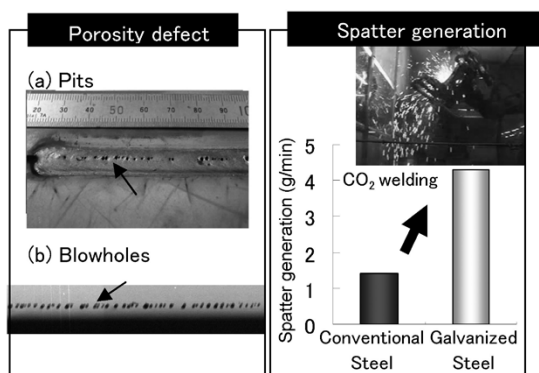


Fig. 1 Welding problems of galvanized steel

to be formed by the zinc gas, generated from the deposit on the lapped portion, penetrating into the molten pool; however, the details of their generation behavior have not been clarified yet, either.

In the present study, we conducted a dynamic observation of porosity formation behavior in the lap fillet welds of galvanized steel sheets and, on the basis of the observation results, have proposed guidelines to reduce porosity defects.<sup>5)</sup> This report also describes the features and effects of a newly developed welding process, "J-Solution™ note 1) Zn"<sup>6) - 9)</sup> (hereinafter referred to as "J-Solution Zn"), for galvanized steel sheets. This new process was developed in the course of the present study to reduce porosity defects and the amount of spatter simultaneously.

## 1. The generation mechanism of porosity defects

### 1.1 Experimental method

The test material was galvanized steel sheets 2.3mm thick (with 45g/m<sup>2</sup> of zinc coating). Spot welding was used to ensure the adhesion of the lapped surfaces (Fig. 2), so as to prevent zinc vapor from escaping to the outside through gaps. Pulsed MAG welding was performed under the conditions shown in Table 1 to study the effect of the welding positions on the numbers of pits and blowholes generated. The surface of each molten pool during welding was observed by a high-speed video camera at a frame rate of 6,000fps. The porosity formation phenomenon inside each molten pool was observed dynamically using a high-intensity X-ray radiography imaging system (an installation of the Joining and Welding Research Institute, Osaka University), shown in Fig. 3, at a frame rate of 500fps.

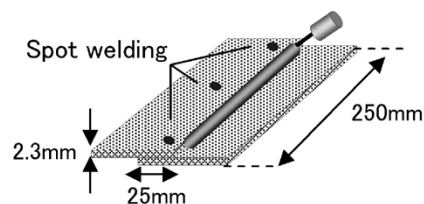


Fig. 2 Schematic diagram of lap joint in fillet welding

note 1) "J-Solution" is a trademark jointly owned by Kobe Steel, Ltd. and DAIHEN Corporation.

Table 1 Welding conditions

Base plate	Galvanized steel sheet (Zinc amount ; 45g/m <sup>2</sup> )
Joint type	Fillet lap joint (Gap:0mm)
Wire	JIS Z 3312 YGW15 φ 1.2mm
Shielding gas	80%Ar+20%CO <sub>2</sub> (20 L/min)
Welding process	Pulsed MAG Welding
Tip height	15mm
Welding speed	100cm/min
Wire feed rate	7.3m/min
Arc voltage	18~30V
Welding position	Horizontal, Downward 30°

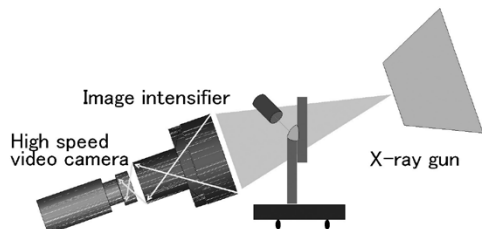


Fig. 3 Schematic diagram of X-ray radiography imaging system

## 1.2 Observation of porosity defects

The generation of porosity defects has been known empirically to be greatly affected by welding positions. Fig. 4 shows the number of pits generated during welding in the horizontal and downward positions, while Fig. 5 shows the number of blowholes generated during the same. As is shown clearly, the downward position causes increased numbers of pits and blowholes to be generated, in comparison with the horizontal position. Fig. 6 shows the surface conditions of the molten pool captured by a high-speed video camera. It has been confirmed that larger numbers of pits and blowholes tend to be generated when the zinc gas, vaporized from the zinc layer, is discharged from inside the molten pool in the rear of the arc, as in the case of the downward position shown in Fig. 6 (b). On the other hand, it has also been confirmed that pits are unlikely to be generated, and the number of blowholes is decreased, when the zinc gas is discharged from directly under the arc, as in the case of the horizontal position shown in Fig. 6 (a). This tendency was the same for various welding currents and arc voltages. The downward position is characterized by the fact that the molten pool moves ahead of the arc. Thus, the present experimental results imply that the porosity formation phenomenon is greatly affected by the conditions of the dug portion directly under the arc.

On the basis of the above assumption, the phenomenon of porosity formation directly under the arc was confirmed. A high-intensity

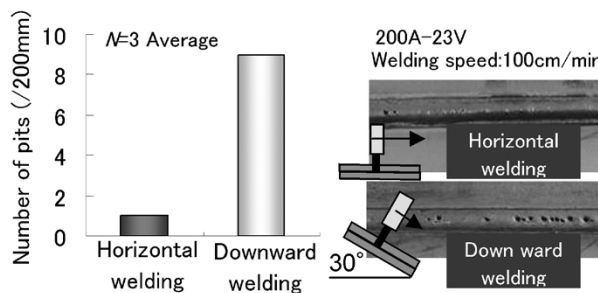


Fig. 4 Effect of welding position on number of pits

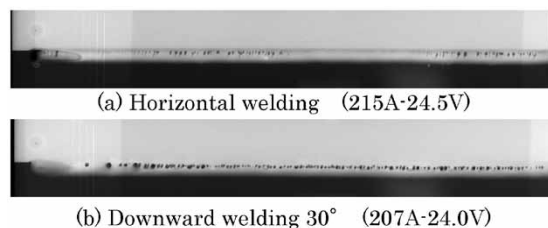


Fig. 5 Effect of welding position on blowhole generation

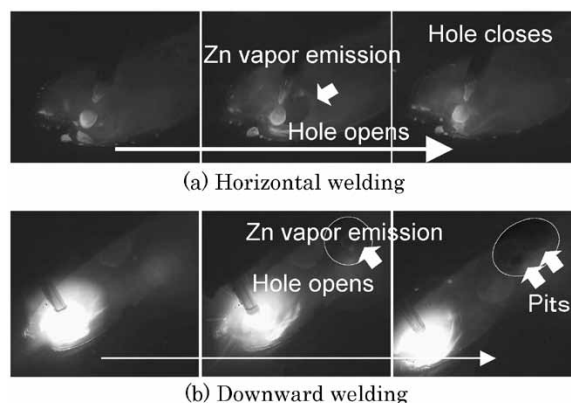


Fig. 6 Observation of molten pool surface by high-speed video camera imaging

X-ray radiography imaging system was used to dynamically observe the formation behavior of porosity defects inside the molten pool. The results are shown in Fig. 7 and Fig. 8. This system offers clear transmission images, allowing distinct observation of the formation and growth of porosity defects even at the frame rate of 500fps. One characteristic of the phenomenon is that all the porosity defects originate and grow from the root portion of the sheet lap, with all of the points of origin being formed under the thin layer of the molten metal directly under the arc. In other words, there is no sudden appearance of porosity originating to the rear of, and slightly away from, the arc. Another characteristic is that a significant amount of zinc gas is constantly released outside the molten pool from the dug portion directly under, and immediately to the rear of, the arc. For example, a porosity defect formed at the position indicated by an arrow in Fig. 7 (a) disappeared at 4ms as a result of the release of gas outside the molten

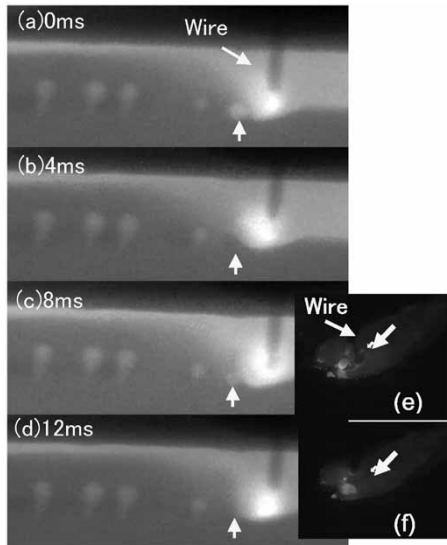


Fig. 7 Behavior of blowhole released from under the arc to outside of the molten pool

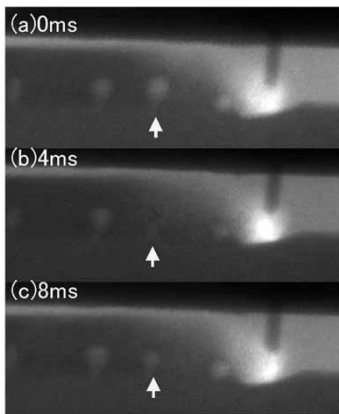


Fig. 8 Behavior of residual blowholes that was not released under the arc

pool (Fig. 7 (b)). Furthermore, a porosity defect formed again at 8ms (Fig. 7 (c)) and disappeared at 12ms (Fig. 7 (d)). These phenomena have also been observed from the surface of the molten pool, as shown in Figs. 7 (e) and (f). Thus a porosity defect repeatedly appears and disappears directly under the arc; however, once its point of origin is carried to the rear of the arc, there is no case in which a porosity defect completely disappears there. For example, a porosity defect that had grown large, as indicated by an arrow in Fig. 8 (a), once shrank at 4ms as a result of the release of gas, with its point of origin not disappearing (Fig. 8 (b)) and started to grow again at 8ms (Fig. 8 (c)). In other words, it is considered that, once a point of origin is carried to the rear of the arc, it remains as a blowhole or a pit in most cases. The relationship between the dug depth and the number of blowholes is shown in Fig. 9. The dug depth directly under the arc was obtained from the X-ray video image. It turns out that as the depth increases, the number of blowholes decreases.

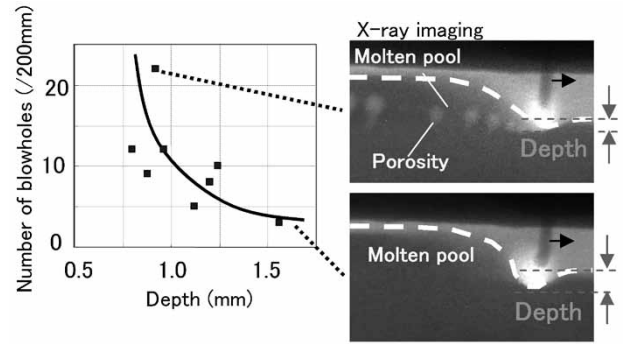


Fig. 9 Relationship between depth of molten pool under the arc and porosity defects

As described above, the final number of porosity defects generated for a zero joint gap is considered to be governed by the relative positions of the arc and molten pool. Therefore, it is considered that a significant suppression of porosity formation can be effectively achieved by maintaining the molten metal layer directly under the arc as thin as possible, such that the zinc gas can be released outside the molten pool at an early stage.

## 2. Study on the reduction of porosity defects

The observation described in section 1 has revealed an important subject for porosity reduction: that is, how to release zinc gas from directly under the arc. To release zinc gas, it is considered effective to somehow decrease the amount of the molten metal that directly flows in under the arc, such that the surface of the base material is exposed.

The shape of the molten pool directly under the arc is governed by the balance between the arc force and the fluidity of the molten metal (Fig.10). It is considered that the digging directly under the arc can be promoted by (a) controlling the balance of forces exerted on the molten pool by suppressing the fluidity and (b) increasing the arc force. To achieve these objectives, we studied the basic elements of MAG welding, i.e., welding wire, shielding gas and the waveform control of electric current by the welding power source.

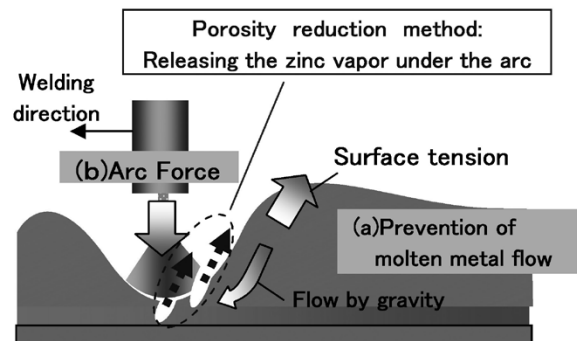


Fig.10 New ideas for reduction of porosity defects

Table 2 Chemical composition of test wires (mass%)

	C	Si	Mn	P	S
Wire1	0.03	0.92	1.36	0.008	0.057
Wire2	0.05	0.56	1.12	0.003	0.014
Wire3	0.05	0.76	1.25	0.008	0.004
Wire4	0.05	0.72	0.60	0.009	0.005

## 2.1 Study on welding wire

One method of suppressing the fluidity, against gravity, of molten metal flowing in directly under the arc is to increase its surface tension. The surface tension of molten iron is known to depend on the chemical composition of the wire. In particular, the oxygen (O) content and sulfur (S) content, the elements called "chalcogen elements", are known to be two major determining factors.<sup>10)</sup> Of the two, we focused on the S content, which is easier to control.

On the other hand, increasing the arc force requires a large current output. This can be achieved by decreasing the electrical resistance of the wire so as to reduce the contribution of the Joule heat at the wire extension. Since the electrical resistance of the wire depends on the chemical composition, we focused on manganese (Mn), which contributes the most, and we controlled the amount of it.

### 2.1.1 Experimental method

Table 2 shows the chemical compositions of the tested wires having varying S and Mn content. In general, the surface tension increases with decreasing S content. Therefore, wire 3 exhibits the greatest surface tension among the wires tested. On the other hand, wire 4 has the lowest electrical resistance, since the resistivity decreases with decreasing Mn content. These wires were used to study the method for exposing the base material directly under the arc.

In each case, welding was conducted in a downward position with a lead angle of 30 degrees, the position which is known to be prone to porosity defects. The welding was repeated three times for a given condition. The number of pits was counted visually, while that of blowholes was determined by radiographic testing (RT).

### 2.1.2 Reduction of porosity by welding wire composition

Fig.11 compares the numbers of blowholes obtained for the tested wires. (Each number represents the average of three repeats.) The number of blowholes decreases with decreasing

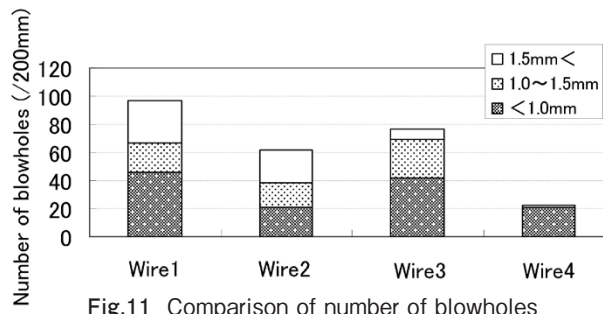
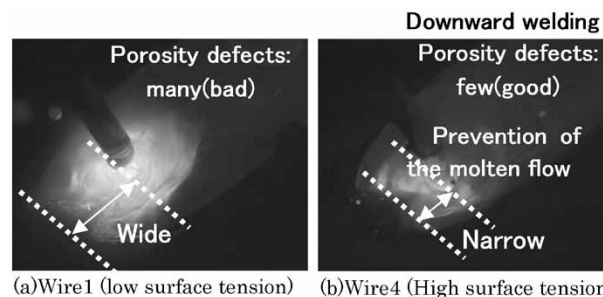


Fig.11 Comparison of number of blowholes



(a)Wire1 (low surface tension) (b)Wire4 (High surface tension)

Fig.12 Comparison of leading distance of molten pool against arc in conventional, as opposed to developed wire

S content (i.e., increasing surface tension). In particular, blowholes larger than 1.5mm have decreased significantly. This result confirms that reducing the additive amount of S, a surface active element, to a minimum and thus increasing the surface tension is an effective approach for reducing blowholes. It should be noted that wire 4, having low Mn content, exhibits a significantly decreased number of blowholes compared with wire 3, which has the same S content. This is considered to have been caused by the decreased electrical resistance of the wire, which increased the electric current required for maintaining the melting rate of the wire and increased the arc force. Two types of lap fillet welding were performed, both in a downward position with a lead angle of 30 degrees, using wire 1 (low surface tension) and wire 4 (high surface tension, low electrical resistance) respectively. For each welding, the shape of the molten pool was captured by a high-speed video camera (Fig. 12). Wire 1, with its low surface tension, was more affected by gravity and exhibited a wide leading distance of molten pool. On the other hand, wire 4, having a higher surface tension, exhibited a smaller leading distance with an increased dug depth. This is considered to have been caused by the molten metal's being pushed up to the rear by the arc force and maintaining its shape against gravity without flowing into a position directly under the arc. These results imply that the wire composition that effectively resists porosity formation will be found in the low S - low Mn system.

## 2.2 Study on shielding gas

Shielding gas is known to greatly affect the shape of the arc. In the case of a mixture of Ar and CO<sub>2</sub>, a higher CO<sub>2</sub> gas ratio brings a cooling effect as a result of the decomposition reaction of CO<sub>2</sub>, which causes the constriction of the arc.<sup>11)</sup> This effect causes the arc force to be more concentrated in a small area. In other words, the current density of the arc is increased, increasing the digging action directly under the arc.

### 2.2.1 Experimental method

To verify the above assumption involving the effect of the CO<sub>2</sub> gas ratio, pulsed MAG welding was performed using welding wire YGW15 ( $\phi$  1.2mm). Two types of gas mixtures, 80%Ar - 20%CO<sub>2</sub> and 70%Ar - 30%CO<sub>2</sub>, were used to study porosity in the weld. The porosity was evaluated in the same manner as described in section 2.1.

### 2.2.2 Reduction of porosity defects by gas composition

Fig.13 shows the effect of shielding gas composition on porosity defects. The commonly used gas mixture, 80%Ar - 20%CO<sub>2</sub>, has caused more than 40 blowholes. On the other hand, the mixture with increased CO<sub>2</sub> gas ratio, 70%Ar - 30%CO<sub>2</sub>, has resulted in about 14 blowholes. The shape of the molten pool for each gas mixture, captured by a high-speed video camera, is shown in Fig.14. It has been demonstrated that the gas composition, 70%Ar - 30%CO<sub>2</sub>, results in an increased digging width in the molten pool. Thus, the increased CO<sub>2</sub> gas ratio is confirmed to increase the arc force, enabling the maintenance of a digging shape appropriate for porosity resistance. However, a CO<sub>2</sub> gas ratio exceeding 30% results in an extreme

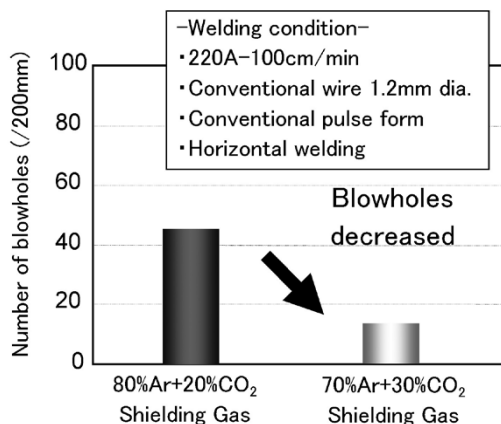


Fig.13 Effect of shielding gas composition on porosity defect

increase in spatter, which significantly deteriorates welding workability. Thus a CO<sub>2</sub> gas ratio of 30% is considered to be the upper limit in practice.

## 2.3 Study on welding current waveform

The relationship between the welding method and the number of porosity defects was studied using a low-frequency superimposed pulse waveform<sup>12)</sup> with modulated frequency and peak current, as shown in Fig.15, as a way of creating contrast in the arc force.

### 2.3.1 Experimental method

Welding was performed using the wire YGW15 ( $\phi$  1.2mm) and the 70%Ar - 30%CO<sub>2</sub> shielding gas that had been confirmed to be effective in reducing porosity defects. The frequency of the low-frequency superimposed pulse was kept in the range from 0 to 30Hz.

### 2.3.2 Reduction of porosity defects by controlling current waveform

Fig.16 shows the relationship between the number of blowholes and frequency. In the case of the low-frequency superimposed pulse welding, the molten pool was observed to vibrate strongly at the frequencies of 10Hz and 20Hz. This vibration facilitates the exposure of the base material directly under the arc and promotes the release of the zinc gas. This is considered to have caused the reduced number of porosity defects at 10Hz and 20Hz compared with the conventional pulse.

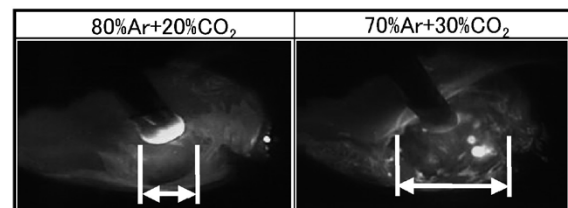


Fig.14 Relationship between shielding gas composition and width of arc-dug portion in molten pool

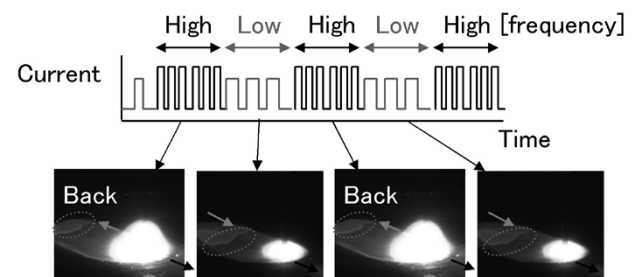


Fig.15 Swing behavior of molten pool caused by low-frequency superimposed pulse

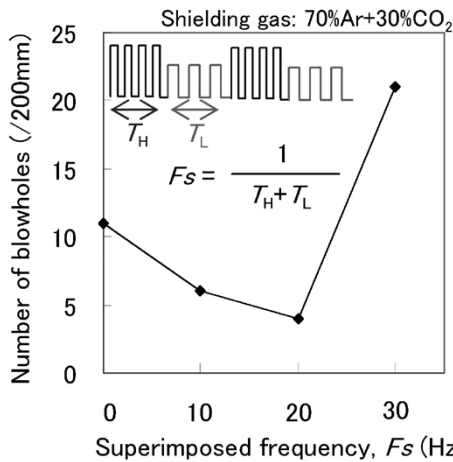


Fig.16 Relationship between superimposed frequency and number of blowholes

### 3. Method for reducing spatter

As shown in Fig. 1, the welding of galvanized steel sheet is inherently susceptible to spatter. In addition, the use of a gas with a higher than conventional CO<sub>2</sub> ratio, the gas known to exhibit excellent porosity resistance, has a multiplier effect of making the welding more susceptible to spatter compared with the conventional welding method. This is because the generation of zinc gas and increased CO<sub>2</sub> ratio cause the droplet to remain at the tip of the wire without detaching from it, making the droplet grow large and hindering its detachment. Hence, the reduction of spatter was studied using a method for smoothly detaching the droplet by employing a two-step pulse waveform (Fig.17) in which the first peak current is kept at a high level and the second peak current at a lower level. A wire with a small diameter was also used to facilitate droplet detachment.

#### 3.1 Experimental method

A gas mixture of 70%Ar - 30%CO<sub>2</sub> was used. Droplet transfer when using the conventional rectangular pulse waveform was compared with that of the two-step pulse waveform.

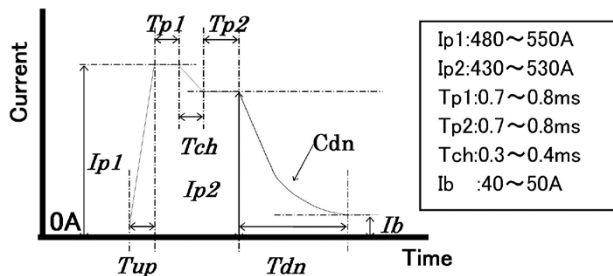


Fig.17 Two-step pulse wave form and parameter

Another comparison was made between the wire diameters of  $\phi$  1.2mm and  $\phi$  1.0mm.

#### 3.2 Spatter reduction effect of two-step pulse waveform and small diameter wire

Fig.18 shows the shapes of the arcs produced by the conventional rectangular pulse and two-step pulse, both using the 70%Ar - 30%CO<sub>2</sub> gas mixture. In the case of the conventional rectangular pulse, in which the pulse peak current is constant, the arc is generated in a low position, which disables the pinch force that should be exerted throughout the molten portion of the wire, making the droplet transfer unstable. The resultant phenomena includes the scattering of the droplet outside the molten pool by the zinc vapor blown from below, and the short-circuiting of the droplet, which has been unable to detach and has grown excessively, with the base material, both resulting in spatter. In the case of the two-step pulse waveform, on the other hand, only a small amount of spatter was confirmed. This is a result of the arc generated at a high position and the stable growth and detachment of the droplet.

In addition, a smaller wire diameter tends to yield a smaller droplet, which increases the current density, improving the ability of the electromagnetic pinch force to detach the droplet. This enables droplet detachment at an early stage. Especially in the case of pulse welding, in which a strong electromagnetic pinch force is exerted at the peak current, droplet transfer can occur smoothly even when the mixed gas atmosphere used is 70%Ar - 30%CO<sub>2</sub>, with a CO<sub>2</sub> ratio higher than that of the conventional atmosphere.

Fig.19 shows the effect of shielding gas and wire diameter on spatter generation. The amount of spatter for  $\phi$  1.2mm wire was about 1.1g/min when combined with the commonly used shielding gas (80%Ar - 20%CO<sub>2</sub>) and conventional rectangular pulse. In contrast, the use of the 70%Ar - 30%CO<sub>2</sub> gas increased the amount of spatter to 1.4g/min. On the

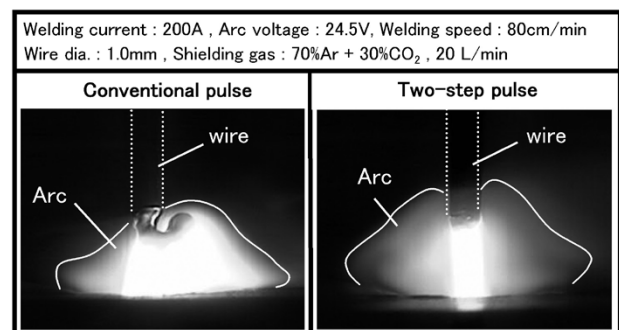


Fig.18 Comparison in arc shape between conventional pulse and two-step pulse

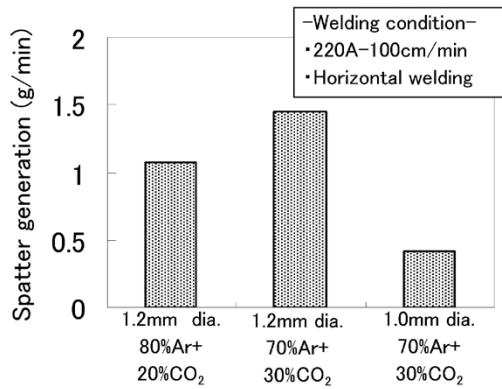


Fig.19 Effect of shielding gas and wire diameter on spatter generation

other hand, the combination of the two-step pulse waveform and  $\phi$  1.0mm wire resulted in an amount of spatter of about 0.4g/min even when the 70%Ar - 30%CO<sub>2</sub> gas was used. This is a significant reduction of spatter compared with the conventional method.

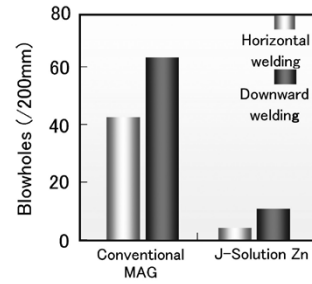
#### 4. Newly developed welding method, "J-Solution Zn"

Fig. 20 depicts a new welding process, named "J-Solution Zn", developed for galvanized steel sheets. This newly developed process has combined features that effectively assure porosity resistance and low spatter: i.e., ① shielding gas consisting of 70%Ar - 30%CO<sub>2</sub>, ② a  $\phi$  1.0mm welding wire, "FAMILIARC™ MIX-Zn" (hereinafter, "FAMILIARC MIX-Zn"), newly developed as a low S-low Mn wire, and ③ a power source for pulsed MAG/MIG welding, "DIGITAL PULSE DP400R", manufactured by DAIHEN Corporation and equipped with waveform controls for the low-frequency superimposed pulse and two-step pulse. Figs.21 and 22 respectively show the number of blowholes and the amount of spatter yielded by

Reduction of porosity	Solution	Reduction of spatter
70%Ar +30%CO <sub>2</sub>	 Shielding gas	-
Low Mn & low S	 Welding solid wire FAMILIARC MIX-Zn	1.0mm dia.
Low-frequency superimposed pulse	 Power source DP400R	Two-step pulse

Fig.20 Composition of J-Solution Zn

note 2) FAMILIARC (FAMILIARC™) is a trademark of Kobe Steel, Ltd.



	Radiographic testing result (Downward welding)
Conventional MAG	
J-Solution Zn	

Fig.21 Use of J-Solution Zn for blowhole resistance

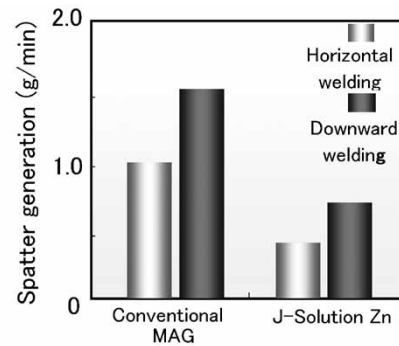


Fig.22 Use of J-Solution Zn for reduction of spatter generation

J-Solution Zn, both compared with the conventional method shown in Table 1. J-Solution Zn has realized the improvement of porosity resistance, as well as decreased spatter.

#### Conclusions

Attempts were made to observe the porosity formation behavior in the weld of galvanized steel sheets. This has led to the development of a new process, "J-Solution Zn", for achieving the simultaneous reduction of porosity defects and the amount of spatter, which can deteriorate the welding workability.

To improve product quality and productivity, the use of galvanized steel sheets is expected to increase. We will strive to introduce and deploy the newly developed process to the markets in Japan and overseas.

The present process was developed in collaboration with the following, to whom we would like to express our sincere gratitude and

appreciation: Messrs. T. Kamizono, Y. Ueda and K. Nakamura of DAIHEN Corporation for their efforts in developing the current waveform control, Professor M. Tanaka of Joining and Welding Research Institute, Osaka University, who allowed us the use of their high-intensity X-ray radiography imaging system, and Assistant Professor S. Tashiro for his cooperation in capturing the images.

## References

- 1) R. Suzuki. Welding Technology 9-12. 2006. Sanpo Publications Inc.
- 2) I. Kimoto et al. Preprints of the National Meeting of JWS, 58. 1996, p.52.
- 3) H. Hirai. DENKI-SEIKO (ELECTRIC FURNACE STEEL). 1996, 67 (3), p.221.
- 4) H. Matsui et al. Quarterly Journal of the Japan Welding Society. 1998, 16 (1), p.45.
- 5) K. Yamazaki et al. Preprints of the National Meeting of JWS, 90. 2012, p.90.
- 6) S. Izutani et al. Preprints of the National Meeting of JWS, 90. 2012, p.92.
- 7) K. Nakamura et al. Preprints of the National Meeting of JWS, 90. 2012, p.94.
- 8) Y. Ueda et al. Preprints of the National Meeting of JWS, 90. 2012, p.96.
- 9) S. Izutani et al. Preprints of the National Meeting of JWS, 91. 2012, p.396.
- 10) K. Nakamura et al. TETSU-TO-HAGANE. The Iron and Steel Institute of Japan. 1983, 69 (16), p.1989.
- 11) M. Tanaka et al. J. Plasma Fusion Res. 2012, Vol.88, No.5, p.276.
- 12) Y. Ueda et al. Preprints of the National Meeting of JWS, 85. 2009, p.88.

# Expansion of "MX-MIG process" as Pure Argon Gas Shielded Welding Method - for Carbon Steel

Reiichi SUZUKI\*1, Ryu KASAI\*2

\*1 Welding Process Dept., Technical Center, Welding Business

\*2 Shinko Welding Service Co., Ltd.

*It used to be considered that pure argon (Ar) was inapplicable to metal inert gas (MIG) welding using steel wire. However, the newly developed process called "MX-MIG," which involves the use of a special welding wire made by Kobe Steel, makes it easily applicable. Many new characteristics are obtained by the MX-MIG process, such as ultra-low spatter, fumes, and slag, as well as excellent bead shape, appearance and weld metal quality. These are the features that were conventionally impossible to achieve with reactive gas. This paper introduces the arc stabilization mechanism and general characteristics of the MX-MIG process, as well as the mechanism for improving the paintability, corrosion toughness and fatigue strength of the carbon steel weld joint. The non-slag characteristic contributes to improved paintability. On the other hand, the fatigue strength is improved by combining the bead shape (wetness) and the low temperature transformation of the crystal microstructure.*

## Introduction

Conventionally, metal inert gas (MIG) welding using steel wire in pure argon (Ar) has been considered impossible.<sup>1), 2)</sup> Against this background, Kobe Steel has made it possible by an MX-MIG process using welding consumables developed by this company and has achieved various new characteristics that cannot be obtained in the conventional reactive gas atmosphere. This paper introduces the arc stabilization mechanism and general features of the MX-MIG process. The main focus is on the mechanism for improving paintability and corrosion resistance by using the MM-1S wire of FAMILIARC™, note 1) (hereinafter "MM-1S"), a family of welding wires designed exclusively for carbon steel, and the mechanism for improving joint fatigue strength by using a wire, TRUSTARC™, note 2) MM-1HS (hereinafter "MM-1HS").

## 1. Problems of welding in pure Ar and the approach taken by the MX-MIG process

The molten shape of wire in the welding arc of

note 1) FAMILIARC (FAMILIARC™) is a trademark of Kobe Steel.

note 2) TRUSTARC (TRUSTARC™) is a trademark of Kobe Steel.

a consumable electrode has been known to have a close relationship with the shielding gas.<sup>3)</sup> Fig. 1 shows the typical relationship between shielding gas composition and the mode of droplet transfer.

In general, a higher CO<sub>2</sub> ratio results in ① a more globular droplet, ② an arc generated from a lower portion of the droplet and ③ a short arc focused on a narrow width. This is caused by the fact that CO<sub>2</sub> is a molecule composed of three atoms. Fig. 2 is a schematic diagram of droplet transfer by an arc in an oxidizing shielding gas. The process of droplet transfer is as follows: 1) The molecules dissociate in an ultra-high temperature arc, in which the dissociation reaction is endothermic. 2) The arc is cooled by the endothermic reaction and shrinks, an action securing thermal stability (thermal pinch force). 3) As a result, the arc comes to be generated from the lower portion of the droplet hanging from the wire. 4) The arc force, generated from the lower portion of the droplet, has a vector opposite to the direction of fall of the droplet, which pushes the droplet up, with the result that the droplet falls less frequently and is more globular. 5) Once the current path is shrunk, a strong electromagnetic force is exerted inwardly (electromagnetic pinch force), causing the droplet to be detached and transferred

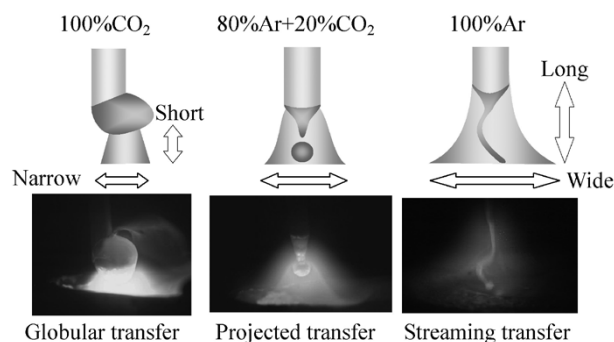


Fig. 1 Typical relationship between shielding gas composition and droplet transfer shape (Solid wire, 1.2mm dia., 300A)

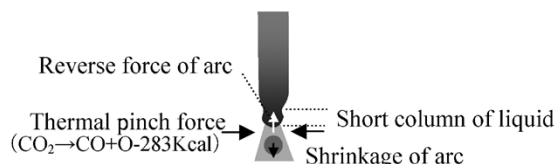


Fig. 2 Schematic diagram of droplet transfer by oxidizing gas shield arc

straight downward, while keeping its globular shape. The above process is repeated for the stable melting and transfer of the wire.

In contrast to this, a monoatomic molecule gas such as Ar does not dissociate in the arc, causing neither an endothermic reaction nor a thermal pinch force. As a result, the arc is generated from a large portion of the wire, including its upper part, and melts the wire. On the other hand, the wide current path can create only a weak electromagnetic pinch force not capable of cutting and detaching the molten wire. This causes the formation of an excessively long liquid column, or the phenomenon called a "streaming transfer". This makes the arc unstable, with its molten portion at the wire tip swinging and whipping (Fig. 3). The resulting weld exhibits a meandering bead, which is called a "wandering phenomenon".

The reason for the long massive liquid column in the Ar gas shielded arc is that a solid wire, having a homogeneous cross-section, starts to melt at the same time throughout almost its entire cross-section.<sup>4)</sup> To resolve this problem, a two-step melting was devised, in which the periphery melts earlier than the center does, such that the solid in the center works as a stable column that prevents the droplet from being affected by a meandering arc. To achieve this, a flux cored wire (hereinafter, FCW) was adapted. The FCW, hitherto unavailable and exclusively designed by Kobe Steel, is combined with pure Ar gas to create a new process, named the "MX-MIG process".

The cross-sectional shape of the FCW is separated into a metal hoop on the periphery and flux in the center. Because most electric current passes through the metal hoop, the flux portion is not directly heated when energized. Therefore, the peripheral hoop melts first, and the inner flux disintegrates, falls and is transferred into the molten pool along with the molten droplet of the hoop. Because the droplet is not formed by melting throughout the entire cross-section, the molten portion at the wire tip does not crawl up, even if the arc crawls up in the gas shield of pure Ar, which maintains the globular-shaped droplet transfer (Fig. 4). Combination with a pulse power source having a high peak current

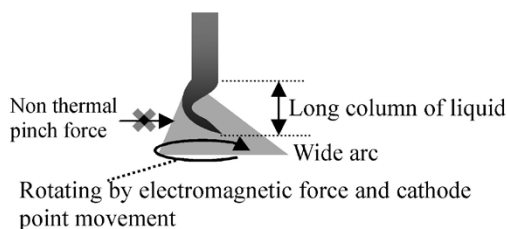


Fig. 3 Schematic diagram of droplet transfer by conventional argon gas shielded arc

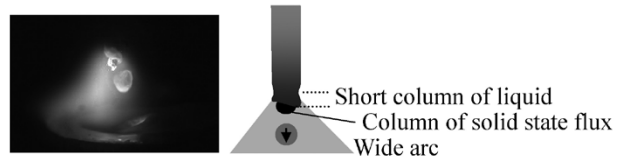


Fig. 4 Schematic diagram of droplet transfer by MX-MIG process combining special flux cored wire with argon gas shielded arc

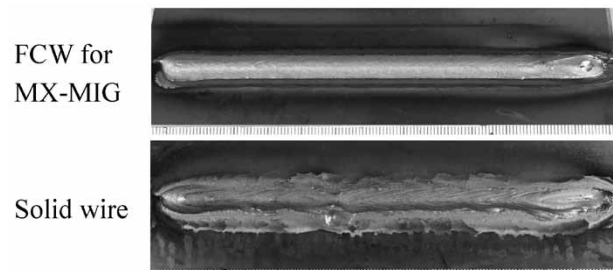


Fig. 5 Examples of bead appearance, comparing MX-MIG exclusive FCW and conventional wire, for argon gas shielded arc

improves the regularity of the droplet transfer, stabilizing the arc in a low current region. It should be noted that not all types of FCWs can achieve normal droplet transfer. Each FCW for MX-MIG is designed such that its composition, hoop/flux ratio and the like are adjusted to achieve the optimum characteristics.

This measure for stabilizing the droplet transfer has enabled the MX-MIG process to produce a weld-metal shape that is superior to that obtained by conventional arc-welding shielded in an oxidizing gas<sup>5)-8)</sup> (Fig. 5).

## 2. Welding quality features of MX-MIG process

Notwithstanding its arc shape that is unique to pure Ar shielding gas, the MX-MIG process has achieved the epoch-making function of significantly stabilizing the droplet transfer, thanks to the design as described in section 1. The arc, unique to the MX-MIG process, has brought about various improvements in the welding quality. The following are the common effects of the process: ①Low spatter: Spatter is due to the counterforce of the arc force. In MX-MIG, the arc area is extended, which suppresses the arc force and leads to an extremely low amount of spattering. ②Low fume: Fume is caused by the evaporation of the metal that is exposed to an ultra-high temperature in the vicinity of the arc anode point. In MX-MIG, the generation of the arc at the wire tip is dispersed, which decreases the arc density and arc temperature, suppressing the fume. This also reduces the amount of hazardous materials, such as hexavalent chromium, that can

cause problems in the welding of stainless steel.

③Slag-free/Low slag: Slag is a compound, formed of elements such as Si, Mn and Ti, which are oxidized in a molten pool. MX-MIG, which uses pure Ar for its shielding gas, is oxygen free and in principle can minimize the generation of slag.

④Less likelihood of being diluted by the base material: MX-MIG has a wide arc area with decreased arc force per unit area, which results in a shallow melting depth. The process is preferable for welding such as overlaying, in which the influence of the base material should be avoided to achieve good weld metal quality.

⑤Clean appearance and shape of the weld bead: The suppressed arc force and extended arc area widen the bead shape, enabling the production of bead shapes with excellent wetting. Welding defects, such as undercut defects, caused by excessive arc force, are less likely to occur. The use of pure Ar gas renders the oxidization of the bead surface unlikely and enables the production of glossy surfaces.

⑥High-speed, high-efficiency: The speeding up of welding generally results in an increased arc force, which increases fluidity and makes the bead more likely to be convex in shape. This also causes so-called "weld-bead humping", a phenomenon in which a bead breaks up. The suppressed arc-force of MX-MIG decreases the fluidity, realizing excellent bead shapes during high-speed welding.

⑦High-quality weld metal: An increased amount of oxygen in steel can cause embrittlement. In the case of stainless steel, an increased amount of carbon lowers the corrosion resistance. MX-MIG uses no CO<sub>2</sub> in its shielding gas, and neither C nor O is dissociated in the arc and transferred into the weld metal, which makes the weld metal very clean.

To achieve these epoch-making features of the MX-MIG process, various welding wires have been developed exclusively for various steel types and applications. The following sections introduce two types of welding consumables designed for carbon steel.

### 3. Welding wire MM-1S, for general carbon steel, to improve paintability and corrosion resistance

MM-1S is an exclusive welding wire that, in particular, exploits the slag-free feature found among the various effects unique to the MX-MIG process described in section 2.<sup>9)-11)</sup>

#### 3.1 Developmental background

Fig. 6 shows an arc-welded portion of an automotive suspension part at the stage of shipment. Despite the post welding corrosion protection

provided by electrodeposition, the part has a large amount of rust generated along the weld metal. On the other hand, no rust has been generated in the area away from the welded portion. Such a phenomenon occurs also on galvanized steel sheets that are surface treated for corrosion protection.

The major cause of the rust generated earlier at welded portions is the existence of welding slag. Welding slag consists of oxides (i.e., SiO<sub>2</sub> and MnO) that are the products of Si and Mn, inevitably contained in steel sheet and welding wire, and reacting with oxygen dissociated from shielding gas such as CO<sub>2</sub> and O<sub>2</sub> at the time of arc welding. The slag has a composition quite similar to that of glass (Fig. 7). These oxides have strong resistance against acid and alkali and are non-conductive. Therefore, they cannot be removed by the conversion treatment applied before the painting process and prohibit the formation of phosphate film. In addition, their non-conductive nature does not permit the formation of a coating film by electrodeposition. The coating film formed, if any, has poor adhesion, and the slag under the coating film is easily peeled off by itself. This is due to the differential thermal expansion between the slag and substrate iron, which causes strain to be introduced during the post weld cooling, making the slag easy to peel off. Thus, the existence of slag inhibits the electrodeposition film from being formed and exposes the substrate iron as a result of peeling-off after painting, making it difficult to impart an anticorrosion function. A method involving chiseling and shot blasting to remove all the slag is not deemed to be realistic for auto parts production, due to cost considerations.



Fig. 6 Rust generated on the welded part after paint treatment

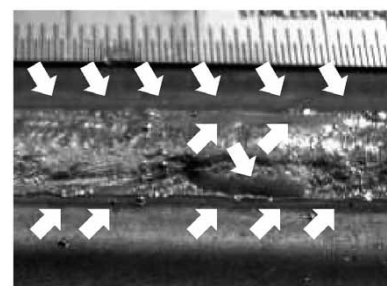


Fig. 7 Welding slag

Meanwhile, galvanization does not provide the welding joint with any anticorrosion function, because the boiling point of zinc is as low as 906°C<sup>12)</sup>, and the ultra-high temperature arc-heat evaporates the zinc. This disables plating beyond the width of the weld metal. It is reported that a sacrificial protection works in the periphery of galvanization<sup>13), 14)</sup>; however, its working distance is too small to cover the entire width of the coating lost by the arc-heat. Thus the use of galvanized steel sheet would accomplish nothing, as far as the welded portion is concerned. Therefore, there has been a need for a more effective approach to prevent rust formation at welded portions.

### 3.2 Mechanism and effect of improving paintability/corrosion resistance

A welded portion must be slag-free for a coating film to form on it. Reducing the slag sources, such as Si and Mn, to zero is not an effective solution because this may oxidize the iron itself, which increases porosity defects and impairs the basic characteristics of the steel. This leaves only one option: that is, to make the oxidizing power of the shielding gas zero so as to inhibit the oxidation reaction of droplets during the arc transfer and in the molten pool. This virtually equates with implementing a shielding gas of pure Ar. Because MIG welding using steel wire in pure Ar has conventionally been considered impossible, there has hitherto been no such practical application of this idea. However, the development of the MX-MIG process, as described above, has enabled the implementation of MIG welding in pure Ar. MM-1S is a wire particularly designed for the most effective exploitation of its slag-free effect. An example of the appearance of the bead produced by this wire is shown in Fig. 8. As shown, the bead of MM-1S has almost no slag formed on it and appears clean.

Fig. 9 compares the bead appearance of the conventional MAG weld made using a general purpose solid wire with that of a weld made using MM-1S. Both welds were made on an actual auto

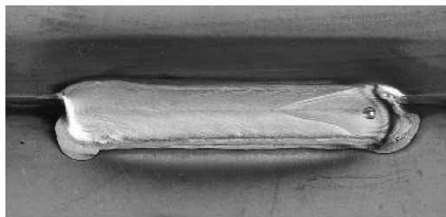


Fig. 8 Bead appearance using FAMILIARC MM-1S

Welding condition;  
100%Ar shielding gas, Pulse power source, 220A current,  
100cm/min travel speed, Lap joint of mild steel 2.3mm thickness

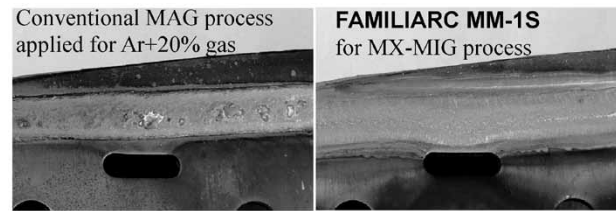


Fig. 9 Slag-free effect of FAMILIARC MM-1S in actual parts

part. The conventional method resulted in slag being formed along the side and at the center of the bead, while MM-1S resulted in no slag formation.

The MM-1S and conventional welding methods / consumables were compared as to their paintability and corrosion resistance. The results are shown in Fig.10. After the electrodeposition, both the CO<sub>2</sub> welding and Ar + CO<sub>2</sub> mixed gas welding, using conventional welding consumables, resulted in painting defects at locations such as the edge of the bead. This sample was subjected as-is to a corrosion test, including repeated cycles of salt water spraying, drying and wetting. In the case of the conventional welding, the rust generation from the edge of the bead becomes evident as the number of cycle increases.

Now two things are known regarding the conventional welding method. The first is that, although Ar + CO<sub>2</sub> mixed gas is reported to generate a smaller amount of slag compared with CO<sub>2</sub> gas, the two are comparable in terms of rust inhibition. This is considered to indicate that the amount of rust is not in a linear relationship with the number of origins of the rust, and a minute number of origins can cause a significant deterioration. The second is that, even if the steel sheet is galvanized, that does not have much effect on the rust inhibition of the welded portion, as described above. In the early stage (at a low cycle number) of the corrosion test, the galvanized steel exhibits a slightly smaller amount of rust, an indication of sacrificial protection; however, the galvanized steel becomes almost comparable to the general steel as the cycle extends to a long term. Meanwhile, the propagation of rust in the direction away from the bead seems to be slightly suppressed.

On the other hand, the Ar gas shielded welding using MM-1S allows almost perfect electrodeposition, which results in almost no rust after a long term corrosion condition of 150 cycles.

There has been no measure available to inhibit automotive parts from rusting after welding and thus to improve the paintability. The improvement needs are satisfied by adopting the MX-MIG process using MM-1S as a welding consumable. This can prevent rusting in a less costly and more effective

Steel		Bare carbon steel		Galvanized steel		Bare carbon steel	Bare High TS steel
Welding wire	Conv. solid (YGW12)	Conv. solid (YGW15)	Conv. solid (YGW12)	Conv. solid (YGW15)	FAMILIARC MM-1S		
Shielding gas	CO <sub>2</sub>	80%Ar+20%CO <sub>2</sub>	CO <sub>2</sub>	80%Ar+20%CO <sub>2</sub>	100%Ar		
As weld bead appearance							
After electro deposition paint coat							
Appearance after the corrosion test	30 cycle						
	60 cycle						
	120 cycle						
	150 cycle	—	—	—	—		

Fig.10 Results of paintability and corrosion test using several welding methods, wires, and shielding gases in combination

Welding condition; 2.3 or 2.9mm thickness, lap joint, 100cm/min travel speed  
 Chemical treatment condition; Dipping phosphate process solution, target 2g/m<sup>2</sup> quantity  
 Electro deposition paint coat condition; Cation type, target 25μm thickness  
 Corrosion test condition; JASO-CCT standard 8h/cycle  
 1 cycle: 5% salt water mist (35 degrees Celsius·2h)→Drying(60 degrees Celsius·25%RH·4h)  
 →Wetting(50 degrees Celsius·98%RH·2h)

manner than would the adoption of galvanized steel sheet, which can incur higher cost.

#### 4. MM-1HS, welding wire to improve joint fatigue strength in high-tensile steel

MM-1HS is an exclusive welding wire particularly exploiting the bead shape improvement effect and the non-entry of oxygen from the shielding gas into the arc atmosphere, among the various effects unique to the MX-MIG process as described in section 2.<sup>15) - 24)</sup>

##### 4.1 Developmental background

Recently, automotive weight reduction has been increasingly needed to further improve fuel economy and thus to reduce CO<sub>2</sub> emissions. Attempts have been made to thin the parts by using high-tensile-strength steel sheets. However, although the strength of the steel sheet has been increased, the fatigue characteristics of the welded joints have not been much improved, due to their

nature (Fig.11). This is the main factor inhibiting the use of high-tensile-strength steel for suspension parts, due to the importance of their fatigue characteristics.

It has been said that there are two reasons why the fatigue characteristics of welded joint do not improve. The first is the stress concentration at the weld toe, or a shape factor. The second is the tensile residual stress in the periphery of weld toes, or a thermal factor. Whether the stress concentration or residual stress contributes more to fatigue strength reduction is considered to depend on the sheet thickness and joint properties. Regardless of the difference in the contribution ratio, at least one of the two, either the shape or the residual stress, must be improved in order to increase the fatigue strength of a welded joint.

Techniques for improving the shape of a weld toe, more specifically, techniques for increasing the weld toe radius  $\rho$  and/or weld toe angle  $\theta$ , include mechanical grinding and re-melting of the weld toe after welding; however, there has been no more efficient measure than this. In order to improve

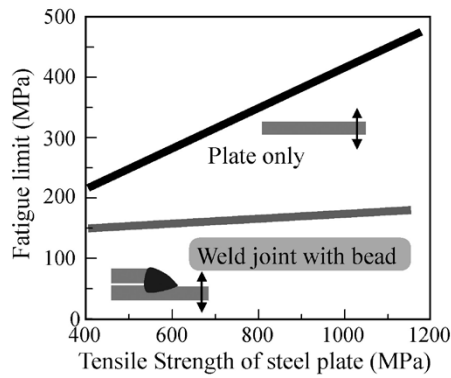


Fig.11 Relationship between tensile strength of steel and fatigue strength

residual stress, on the other hand, techniques such as ultrasonic wave peening and shot-peening have been applied to impart compressive stress to weld toes; however, these techniques are also lacking in efficiency.

Against this background, a technique using a consumable called a "low-temperature transformation welding consumable," has been researched and devised in recent years. This technique exploits the expansion effect of martensite transformation to impart compressive residual stress<sup>25)</sup> (Fig.12). Requiring only the change of welding consumables, this technique is more efficient than conventional ones. However, it has a drawback: a significant cost increase is inevitable because the wire must contain a certain amount of Ni and/or Cr to achieve the low-temperature transformation while realizing reasonable weldability when used in a conventional welding method. Also, there is a concern that an excessively enhanced mechanism of low-temperature transformation may increase the strain in the weld metal, making the weld more susceptible to delayed cracking.

#### 4.2 Mechanism for improving joint fatigue strength

MM-1HS has been developed to solve the conventional problems described in the previous section and to balance characteristics that are generally incompatible with each other, namely, ①improving fatigue strength, ②ensuring crack resistance, and ③suppressing cost increase. The following measures have been taken:

- a) Using the pure Ar shielding gas process to realize a bead shape with a remarkably small stress concentration coefficient, and targeting thin-sheets in which the contribution of stress concentration is higher than other factors affecting the fatigue strength;
- b) Introducing the low-temperature transformation

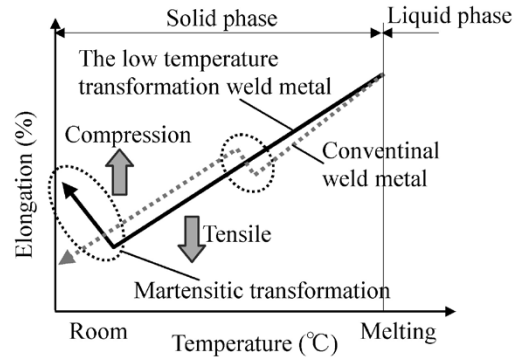


Fig.12 Mechanism of low temperature transformation causing residual strength compression around weld bead

mechanism to make the residual stress compressive in the weld toes to the extent that it does not cause cracking; and

- c) Realizing the low-temperature transformation mechanism without costly alloying elements such as Ni and Cr, by effectively exploiting carbon, in which the pure Ar shielding gas process is used to prevent the carbon from deteriorating weldability.

The following explains the details: As described in section 1, the MX-MIG process enables the stabilization of the droplet transfer, despite the widely spread arc that is unique to Ar gas. As shown in Fig.13, the conventional welding method results in a narrow arc width relative to the width of the bead or of the molten pool, while the MX-MIG process results in an arc width that is even wider than that of the molten pool. This enables the MX-MIG process to heat the edges of the bead, which improves the wetting and, thus, the bead shape. It should be noted that pure Ar must be used to achieve a significant improvement in weld toe shape, as shown in Fig.14.

Next, an FEM analysis was conducted on a lap fillet weld joint subject to a reversed bending amplitude. From the result, a relationship was established between the ratio ( $\rho/t$ ), i.e., weld toe radius ( $\rho$ ) / sheet thickness ( $t$ ), and the stress concentration coefficient  $Kt$ , as shown in Fig.15.  $Kt$  has a minimum value of 1, the equivalent of flat plate, and increases at an accelerating rate as  $\rho/t$  decreases.

A hot-rolled sheet of 780MPa class high-tensile steel, KBHF780OD, having a sheet thickness of approximately 3mm, was used to compare the MX-MIG process using MM-1HS with the MAG process using a conventional solid wire. The former yielded  $\rho$  in a range of approximately 2.5 to 3.2mm; while the later yielded  $\rho$  in a range of approximately 0.2 to 0.7mm. Plotting these values shows the  $Kt$  of 1.1 for the MX-MIG process, the stress concentration

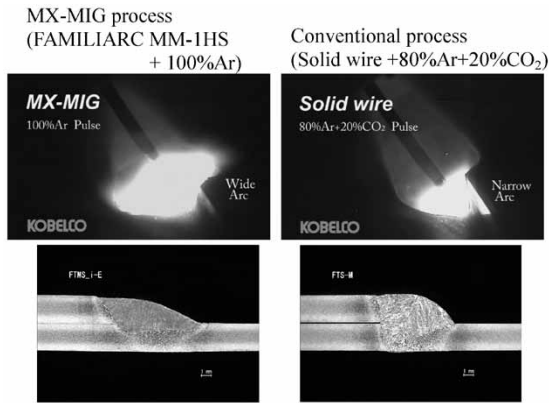


Fig.13 Comparison of arc, molten pool and bead cross shape width in MX-MIG process and conventional welding process (Welding conditions; current: 200A, welding rate: 1,000mm/min, arc voltage)

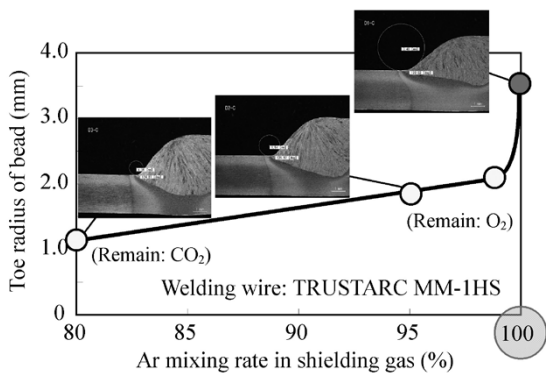


Fig.14 Relationship with argon mixing rate in shielding gas and toe radius of the bead

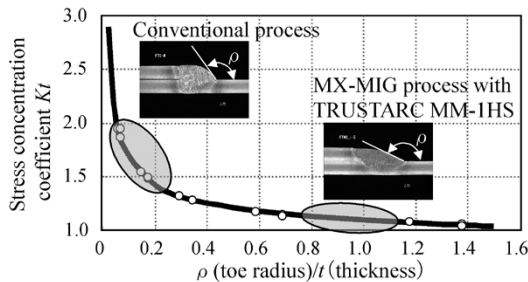
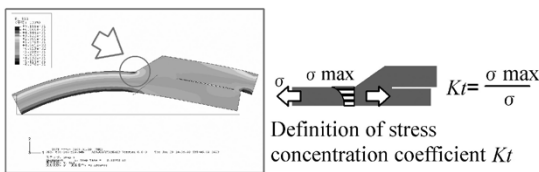


Fig.15 Relationship between toe radius and stress concentration coefficient  $K_t$

that is close to that of a flat plate, and a higher value of approximately 1.5 - 2.0 for the conventional MAG process. In other words, MM-1HS results in a stress concentration, the primary factor in decreasing fatigue strength, that is more relaxed compared with that of the conventional process.

Now, we consider tensile residual stress, another factor decreasing the joint fatigue strength.

Martensite transformation is known as a solid phase transformation accompanying expansion; and the starting temperature of a martensite transformation (hereinafter,  $M_s$ ) is reported to be expressed, for example, as follows:

$$M_s(^\circ\text{C}) = 561 - 474C - 33Mn - 17Cr - 17Ni - 21Mo \dots (1)^{26}$$

$$M_s(^\circ\text{C}) = 550 - 361C - 39Mn - 35V - 20Cr - 17Ni - 10Cu - 5(Mo + W) + 15Co + 30Al \dots (2)^{27}$$

During the cooling process of weld metal, either a ferrite transformation or a martensite transformation occurs, depending on the cooling rate. In accordance with the above  $M_s$  point equations, the  $M_s$  point lowers with an increasing additive amount of C, Mn, Cr, Ni and Mo. Among these elements, Ni, with its advantage of being less susceptible to the cooling rate, is known to be the element that is most effective in causing martensite transformation; however, Ni is very costly. Therefore, the present development proactively exploits C, which has a large coefficient in the  $M_s$  point equations. Being known as an element that causes spatter and fume, C is generally avoided in welding consumables. However, the cause of the deterioration in welding workability associated with the C addition is the gaseous explosion caused by the reaction of oxygen, dissociated from the shielding gas containing  $\text{CO}_2$  and  $\text{O}_2$ , with C in the wire.<sup>28)</sup> The MX-MIG process, on the other hand, has no oxygen in the shielding gas and causes hardly any explosion, which enables the use of wire containing an increased amount of C without causing deterioration in welding workability. Thus the component factor unique to the MX-MIG process permits the proactive use of an inexpensive element that had hitherto been unexploitable.

MM-1HS that was developed has a composition optimally designed for arc stabilization in the MX-MIG process, as well as for low-temperature transformation. FEM analyses were conducted on lap fillet weld joints of 780MPa class steel sheets prepared by conventional welding and by using MM-1HS. The resultant distribution of residual stress in the cross-section of each welded portion is shown in Fig.16.

Comparing the weld toes (circled areas), where the degree of stress concentration becomes high, the joint made by MM-1HS is found to have stronger compressive residual stress. Fig.17 shows the residual stress near the surfaces of actual welded joints, measured by an X-ray residual stress measurement apparatus. MM-1HS exhibits strong compressive stress in the vicinity of the base/weld interface, supporting the analysis results shown in Fig.16.

As described above, MM-1HS is used with a

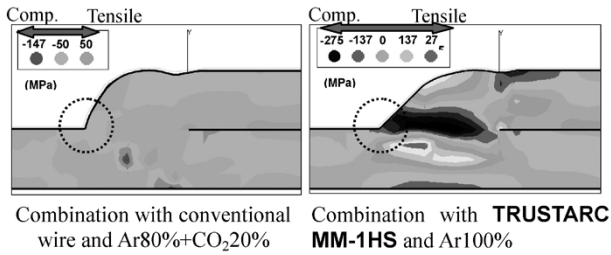


Fig.16 Results of FEM analysis of residual stress in a cross section of the welding joint

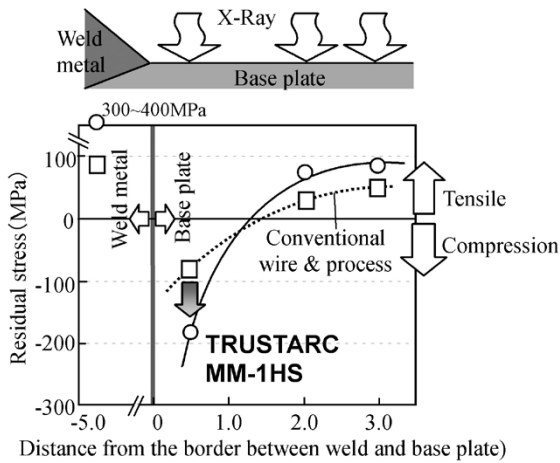


Fig.17 Residual stress on surface of welding toe position, measured using X-ray equipment

shielding gas of pure Ar, which has conventionally been inapplicable, to realize an epoch-making technique for simultaneously improving two issues with weld toes, namely, ①relaxing stress concentration and ②making the residual stress compressive.

### 4.3 Joint fatigue strength improvement effect

Hot rolled steel sheets of 780MPa class (3.4mm thick) were used to prepare lap fillet joints. Fig.18 shows their fatigue strength characteristics (S-N curves). In each diagram, the upper right line represents the fatigue characteristic of a plane base material as a reference. The lower left line represents the fatigue strength characteristic resulting from the conventional welding consumables and method, showing that welding has significantly deteriorated the fatigue strength characteristics compared with those of the plane base material. On the other hand, MX-MIG welding using MM-1HS exhibits a fatigue strength characteristic that is significantly improved compared with that of the conventionally welded joint, although not as high as that of the plane base material. The effect is 3 to 6.2 times in life under 350-400MPa of applied stress and 1.6 times in the fatigue limit strength.

As described above, improvement has been

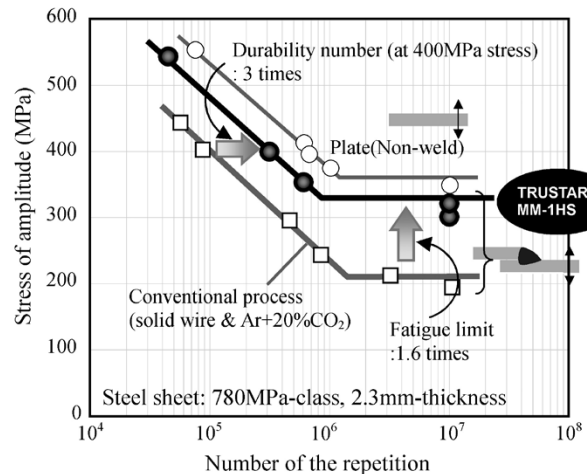
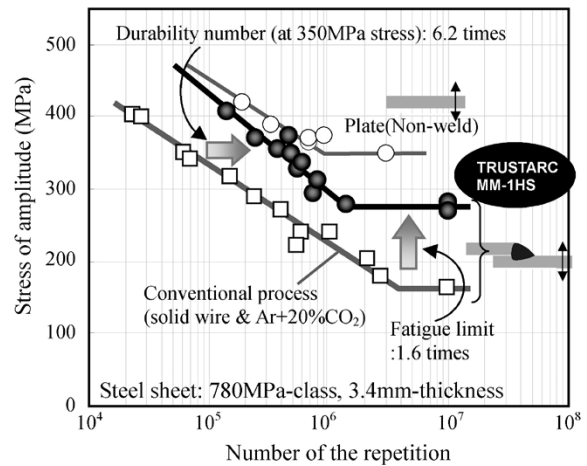


Fig.18 Examples of improving effect on fatigue strength of welding lap joint by applying TRUSTARC MM-1HS

achieved in the fatigue strength characteristics of weld joints. This is expected to improve the structural design, in which thinning and weight reduction has been difficult, bottlenecked by the fatigue characteristics, and to reduce costs as well by eliminating the use of stiffening members such as gusset plates.

### Conclusions

The use of special welding wires has enabled the MIG welding of steel in the shielding of pure Ar, which hitherto had not been feasible. This paper introduces the features of welding consumables for carbon steel; i.e., MM-1S, which improves paintability and corrosion resistance, and MM-1HS, which improves the fatigue strength of joints. The advantages of these consumables are not limited to these features; their use also results in other general improvements, including extremely low spatter and fume, as well as less susceptibility to bead shape failure, and a higher welding speed. With all these features, the MX-MIG process has the potential for raising the quality of gas shielded arc welding. Kobe

Steel will strive to exploit the undeveloped features of inert atmosphere and to make new proposals.

## References

- 1) F. Matsuda et al. Journal of the Japan Welding Society. 1983, 52.
- 2) K. Ando et al. Welding Arc Phenomena. Sanpo Publications Inc., p. 257-268.
- 3) YOSETSU, YOSETSU GIJUTSU NYUMON, Sanpo Publications Inc., p.22.
- 4) K. Taira. Welding technology. Sanpo Publications Inc., Feb. 2006, p.64.
- 5) R. Suzuki. Journal of the Japan Welding Society, 2010, Vol.79, No.6, p.27.
- 6) Y. Umehara et al. Preprints of the National Meeting of JWS. 2008, Vol.81, No.231.
- 7) Y. Umehara et al. No.205 Technical commission on Welding process, Japan Welding Society.
- 8) Kasai et al. IIW Doc.212-1149-09, XII-1970-09, IV984-09, 2009.
- 9) R. Kasai et al. Preprints of the National Meeting of JWS. 2012, Vol.90, No.88.
- 10) R. Suzuki. Welding technology. Sanpo Publications Inc., June 2012, pp.52-59.
- 11) R. Suzuki. Kobe Steel Ltd. Home Page. Technical Report, Vol.522012-7, [http://www.gijutsugaido.jp/catalog/2012/pageview.html#page\\_num=36](http://www.gijutsugaido.jp/catalog/2012/pageview.html#page_num=36), (accessed 2012-11-07).
- 12) Metals Data Book, ed. by Japan Inst. Metals
- 13) K. Ando. The 27<sup>th</sup> Steel Technology Seminar Test, Lecture 11 Surface Treatment, Iron and Steel Institute of Japan.
- 14) Iron and Steel Institute of Japan. The 186<sup>th</sup> and 187<sup>th</sup> NISHIYAMA KINENGIJUTUKOZA, 2005.
- 15) Y. Umehara et al. Preprints of the National Meeting of JWS. 2008, Vol.81, No.232.
- 16) R. Kasai et al. Japan Welding Society No.197 Technical commission on Welding Metallurgy, Japan Welding Society.
- 17) R. Kasai. Kobe Steel Ltd. Home Page. Technical Report, Vol.512011-4, [http://www.gijutsugaido.jp/catalog/techreport/pageview.html#page\\_num=386](http://www.gijutsugaido.jp/catalog/techreport/pageview.html#page_num=386), (accessed 2012-11-07).
- 18) R. Suzuki et al. Welding technology. Sanpo Publications Inc., March 2010, p.74.
- 19) R. Kasai. JWES Technical commission on brazing, Joining of Advanced materials, July 2011.
- 20) M. Kinebuchi. No.89 Technical commission on Joining and materials Processing for Light Structures, Japan Welding Society MP-482 2010.
- 21) M. Kinebuchi. Chemical Plant Welding Research Committee, Japan Welding Engineering Society 6.19. 2012.
- 22) M. Kinebuchi. JSAE Annual Congress (Autumn) 2011.
- 23) M. Kinebuchi. M&M Strength of materials Conference, The Japan Society of Mechanical Engineers. 2011
- 24) M. Kinebuchi. 60th Conference, The Society of Materials Science, Japan, 2011.
- 25) N. Hayakawa. Welding technology. Sanpo Publications Inc., June 2004, p.87.
- 26) S. Haynes. Journal of the Iron and Steel Institute, August. 1956, p.349-359.
- 27) The Japan Institute of Metals and Materials. KOZA, GENDAINO-KINZOKUGAKU-ZAIRYOUHEN Vol.4. Maruzen.
- 28) K. Ando et al. Welding Arc Phenomena. Sanpo Publications Inc., p.210-218.

# Effects of Post Weld Heat Treatment (PWHT) Temperature on Mechanical Properties of Weld Metals for High-Cr Ferritic Heat-Resistant Steel

Genichi TANIGUCHI\*<sup>1</sup>, Ken YAMASHITA\*<sup>1</sup>

\*<sup>1</sup>Welding Process Dept., Technical Center, Welding Business

*Welded joints of high-Cr ferritic heat-resistant steel, ASTM A335 Gr. P91, were subjected to post weld heat treatment (PWHT) to improve mechanical properties and to reduce residual stress. We have measured the  $A_{c1}$  of weld metals for Gr. P91 steel, containing varying amounts of Mn+Ni, and have examined the effects of PWHT temperatures on the mechanical properties of each weld metal. The upper limits of the PWHT temperature for the respective weld metals are considered.*

## Introduction

High-Cr ferritic heat-resistant steel is a material that, along with austenitic heat-resistant steel, has long been studied and utilized. This ferritic steel has a smaller coefficient of thermal expansion compared with the austenitic heat-resistant steel and exhibits excellent creep rupture strength thanks to, among other things, the addition of Nb, V and N. Therefore, this steel is widely used in thermal power plants that run and stop repeatedly, in accordance with the power demand, in an environment of steam at high temperature and pressure. The steel ASTM A335 Gr. P91 is a typical high-Cr ferritic heat-resistant steel and is applied particularly to large diameter thick-walled pipes such as the main steam pipes in thermal power plants.

The welded joints of Gr. P91 steel are generally subjected to post weld heat treatment (hereinafter referred to as "PWHT") to reduce residual stress and to improve the performance of the weld. If the PWHT is conducted at an appropriate temperature and time, the welded joint exhibits favorable mechanical properties. However, if the PWHT temperature is too low, the weld metal exhibits inadequate toughness due to insufficient tempering effect. On the other hand, if the PWHT temperature is too high, the tensile strength at ambient and elevated temperatures becomes insufficient due to excessive tempering effect. Especially in cases where the PWHT temperature exceeds the  $A_{c1}$  transformation point of the weld metal, the weld metal undergoes reverse transformation, which results in a microstructure containing fresh martensite with high strength and low toughness. This microstructure deteriorates the performance of the welded joint. To avoid these problems, the PWHT temperature is controlled

in the actual implementation.<sup>1), 2)</sup> In connection with selecting welding consumables, chemical constituents, such as Mn and Ni, that lower the  $A_{c1}$  transformation point are regulated.<sup>3)</sup> However, not much has been done to validate the applicability of this control and regulation to the weld metals from the aspect of mechanical properties.

In this study, two types of weld metals for Gr. P91 steel, containing different amounts of Mn+Ni, were mainly used to study the change of their mechanical properties during PWHTs performed at temperatures exceeding their  $A_{c1}$  transformation points. The upper limit of the PWHT temperature allowable for each weld metal is considered.

## 1. Experimental method

### 1.1 Tested materials

The materials tested were the weld metals TRUSTARC<sup>TM, note)</sup> CM-9Cb (hereinafter "CM-9Cb") and TRUSTARC CM-95B9 (hereinafter "CM-95B9"). Both are Kobe Steel's covered electrodes for Gr. P91 steel. The CM-9Cb has been used for over 20 years, mainly in thermal power plants in Japan. On the other hand, CM-95B9 is a covered electrode that meets the American Welding Society (AWS) standard, A5.5 E9015-B9: 2006, and features a lower content of Mn and Ni in the weld metal, compared with CM-9Cb. In the following description, the weld metal of CM-9Cb is referred to as "A", and that of CM-95B9 is referred to as "B".

Fig. 1 shows the shape of the welding groove configuration. Plates of JIS G3106 SM490A were used for the test. Prior to the test, each groove surface

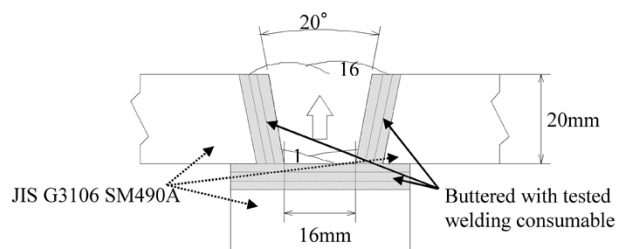


Fig. 1 Groove configuration and pass sequences

note) TRUSTARC (TRUSTARC<sup>TM</sup>) is a trademark of Kobe Steel.

Table 1 Welding conditions

Diameter of core rod	$\phi$ 4.0mm
Welding current (Polarity)	150 A (DCEP)
Welding voltage	26~29 V
Welding speed	14~20 cm/min.
Pass sequences	8Layers 16Passes
Preheat and interpass temperature	235~255 °C
Heat input	Avg.16 kJ/cm
Welding position	Flat

was provided with three layers of buttering welding using respective welding consumables tested and machined smoothly so as to prevent the fluctuation of the chemical composition due to dilution by the base material. **Table 1** shows the welding conditions inside the groove.

## 1.2 PWHT conditions

Each specimen for mechanical properties evaluation was subjected to PWHTs. For weld metal A, the PWHTs were conducted at five temperatures: i.e., 670, 730, 760, 790 and 820°C. For weld metal B, PWHTs were conducted at four temperatures; i.e., 720, 760, 800 and 850°C. The holding time for each PWHT was 4 hrs. The lower control limit for the PWHT temperature was 300°C, while the heating rate and cooling rate above the lower control limit temperature were 55°C/h or lower.

## 1.3 Measurement of $A_{c1}$ transformation points of weld metals

In order to measure the  $A_{c1}$  transformation point, a solid cylindrical specimen of  $\phi 8 \times 66$ mm was taken from each weld metal, as-welded. Each specimen was taken in the direction parallel to the welding direction and from a location at the center of the bead width and of the plate thickness. The  $A_{c1}$  transformation point is defined as the temperature at which the austenitic phase starts to form during the heating process. A general method for measuring the  $A_{c1}$  transformation point involves detecting the expansion and contraction of the specimen during the phase transformation.<sup>4)</sup> This type of measurement technique, however, often yields measurement values that vary significantly, because its accuracy depends on the method of the expansion/contraction measurement and the measurement conditions. Therefore, a preliminary study was conducted to verify the validity of the method adopted in this study for measuring the  $A_{c1}$  transformation point.<sup>5)</sup> The measurement method adopted involves heating a specimen by induction in a high vacuum atmosphere of approximately  $10^{-3}$  Pa, and detecting the diameter change of the specimen during the heating, using a non-contact high-precision measuring system

equipped with an LED device. The heating rate of the specimen was 10°C/min up to 600°C and was 5°C/min in the temperature range from 650 to 1,050°C, the range in which reverse transformation is expected to occur. On the other hand, a carbon steel containing 0.19mass%C was used as a standard sample to verify the validity of the measurement result. For this verification, comparisons were made between the  $A_{c1}$  transformation point measured and the  $A_1$  point that is roughly derived from the Fe-C phase diagram.

## 1.4 Mechanical properties evaluation of weld metal

The mechanical properties evaluated were tensile strength at room temperature, Charpy impact absorbed energy at 20°C and the creep rupture time at 600°C (applied stress : 108MPa and 147MPa). The specimens, in accordance with AWS A5.5, were prepared from each weld metal after the PWHT for the room temperature tensile test and Charpy impact test. Each creep rupture specimen had a diameter of  $\phi 6.0$ mm with extensometer limb and was taken in the direction parallel to the welding direction and from a location at the center of the bead width and of the plate thickness.

## 1.5 Observation on the state of carbonitride precipitation and the extracted residue analysis

A transmission electron microscopy (TEM) study was conducted on the precipitation state of carbonitride after the PWHT. Each TEM observation sample was taken from a cross-section vertical to the welding direction at the center of the bead width and of the plate thickness. The observation was conducted by an extraction replica technique. Extracted residue analysis was conducted to identify the amount and composition of carbonitride, using a solid cylindrical specimen of  $\phi 8 \times 20$ mm. Each specimen was taken from the same location as the TEM observation sample, but in the direction parallel to the welding direction.

## 2. Experimental results and discussion

### 2.1 The chemical compositions of weld metals

**Table 2** shows the chemical compositions of weld metals A and B, as well as that of the carbon steel used as the standard sample for the measurement of  $A_{c1}$  transformation point. The amounts of Mn+Ni in the weld metals were 2.49 mass% for A and 1.38 mass% for B.

### 2.2 $A_{c1}$ transformation point of weld metals

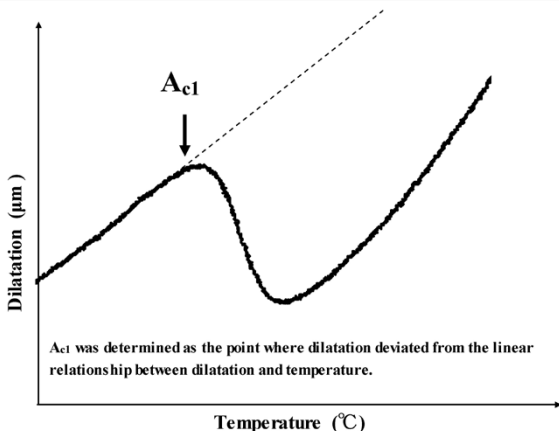
**Table 3** shows the  $A_{c1}$  transformation points

Table 2 Chemical compositions of testing materials

Testing materials	Chemical compositions (mass%)									
	C	Si	Mn	Ni	Cr	Mo	V	Nb	N	Mn+Ni
Weld metal A	0.07	0.35	1.57	0.92	8.86	1.02	0.24	0.025	0.028	2.49
Weld metal B	0.11	0.23	0.85	0.53	9.01	1.01	0.25	0.034	0.027	1.38
Carbon steel	0.19	0.10	0.03	-	-	-	-	-	-	0.03

Table 3 Measurement results for  $A_{c1}$

Weld metal A	733 °C
Weld metal B	785 °C
Carbon steel with 0.19mass%C	732 °C



measured. The  $A_{c1}$  transformation point of the 0.19 mass%C carbon steel, used as the standard sample, was found to be 732°C. This temperature agrees well with the  $A_1$  transformation point of approximately 727°C derived from the Fe-C system phase diagram. This result verifies the reliability of the method used to measure the  $A_{c1}$  transformation point in the present study; i.e., the method involving heating a specimen by induction in a high vacuum atmosphere, and detecting the change in the diameter of the specimen using a non-contact high-precision measuring system with an LED device.

The  $A_{c1}$  transformation points of weld metals A and B, measured in accordance with this method, were 733°C and 785°C, respectively. These measurement results are hereinafter used as the  $A_{c1}$  transformation points of the respective weld metals.

### 2.3 Effect of PWHT temperature on mechanical properties of weld metals

Fig. 2 and Fig. 3 show the relationships between the PWHT temperature and mechanical properties at room temperature of the weld metals A and B, respectively. Also included in each figure is the strength of Gr. P91 steel specified by ASTM.

The room-temperature tensile strength of weld metal A decreases with rising PWHT temperature until the PWHT temperature reaches 760°C, but increases when the PWHT temperature exceeds 760°C. The room-temperature tensile strength of weld metal B, on the other hand, decreases monotonically with rising PWHT temperature and becomes almost

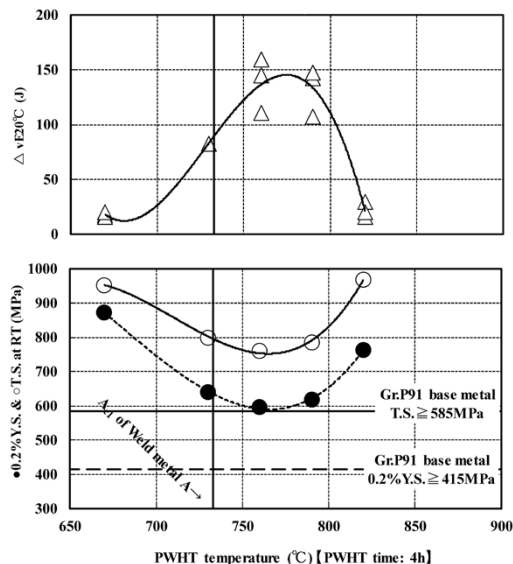


Fig. 2 Relationship between PWHT temperature and mechanical properties of weld metal A at RT

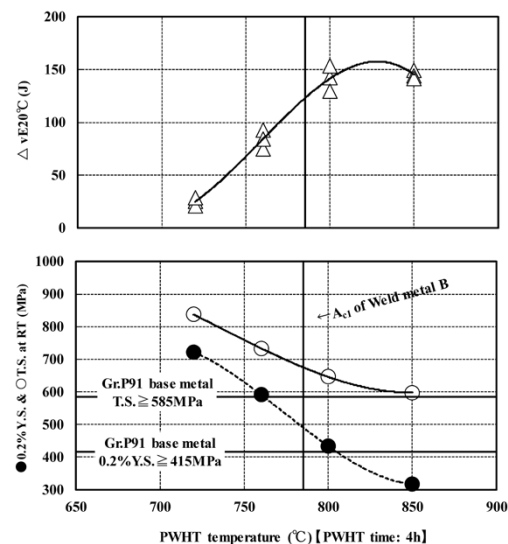


Fig. 3 Relationship between PWHT temperature and mechanical properties of weld metal B at RT

equal to the lower-limit strength value specified for the steel at the PWHT temperature of 800°C. At 850°C, 0.2% proof strength at room temperature drops below the lower-limit strength value specified for the steel.

The absorbed energy of weld metal A increases with rising PWHT temperature until the temperature reaches 760°C, but decreases when the PWHT temperature exceeds 760°C. The absorbed energy of weld metal B, on the other hand, increases with rising PWHT temperature and appears to reach a maximum at a PWHT temperature between 800°C and 850°C.

Fig. 4 shows the relationship between the PWHT temperature and creep rupture time of weld metals A and B. When the applied stress is low (108MPa), the creep rupture times of both weld metals A and B become shorter with rising PWHT temperature. The

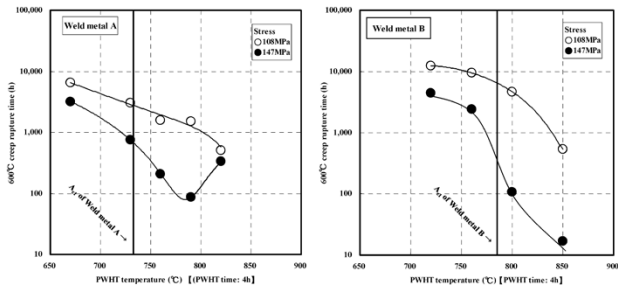


Fig. 4 Relationship between PWHT temperature and 600°C creep rupture time of weld metals A and B

creep rupture time of weld metal B decreases abruptly at PWHT temperatures exceeding 800°C. When the applied stress is high (147MPa), the creep rupture time of weld metal A shortens with rising PWHT temperature until the temperature reaches 790°C, but, in contrast to this, above 790°C, it lengthens. The creep rupture time of weld metal B, on the other hand, shortens with rising PWHT temperature and decreases abruptly at PWHT temperatures exceeding 760°C.

In the case of weld metal A, a reversal phenomenon was observed, at a boundary of the PWHT temperature, in each mechanical property, i.e., the room-temperature tensile strength, absorbed energy and creep rupture time under high applied stress. This phenomenon is considered to be caused by fresh martensite precipitated at PWHT temperatures exceeding the  $A_{c1}$  transformation point. Fresh martensite is formed from the austenitic phase that is formed at temperatures exceeding the  $A_{c1}$  transformation point, undergoing martensitic transformation in the cooling process. The primary objective of PWHT is tempering; however, the fresh martensite is not tempered and exhibits high strength and low toughness. This is considered to have caused the reversal phenomena in the mechanical properties.

There are two facts that should be noted. The first fact is that the reversal of the mechanical properties of weld metal A occurs at temperatures higher than its  $A_{c1}$  transformation point. This fact is roughly explained by the reverse transformation ratio. Fig. 5

shows the reverse transformation ratios of weld metals A and B. Each reverse transformation ratio was determined from the temperature vs. expansion/contraction curve obtained by the  $A_{c1}$  transformation point measurement. For each of weld metals A and B, the ratio of the reverse transformation to the austenitic phase is rather small in the temperature range immediately above the  $A_{c1}$  transformation point, which makes the amount of fresh martensite precipitated in the cooling process small and not enough to cause the reversal of the mechanical properties. On the other hand, as the PWHT temperature rises, the reverse transformation ratio increases, increasing the amount of fresh martensite with high strength and low toughness. This is considered to have caused the reversal phenomena described above. Meanwhile, unlike weld metal A, weld metal B did not show any reversal of mechanical properties even when the PWHT temperature greatly exceeded its  $A_{c1}$  transformation point and the reverse transformation ratio became sufficiently large. This phenomenon cannot simply be explained by the reverse transformation ratio alone. For an explanation, two assumptions were considered; i.e., the precipitation of low C fresh martensite and the precipitation of ferrite phase<sup>6)</sup>. The former, in particular, was considered on the basis of the fact that weld metal B has a smaller amount of Mn + Ni compared with weld metal A. When the amount of Mn + Ni is small, only a small amount of solid solute C is generated in the austenitic phase by the reverse transformation. As a result, low C fresh martensite that is relatively soft is considered to precipitate in the cooling process.

The following experiment was conducted to verify these assumptions. The specimens for the  $A_{c1}$  transformation point measurement were prepared from weld metals A and B, both as-welded. Each specimen was held for 1h at a temperature approximately 30°C higher than its respective  $A_{c1}$  transformation point and was subjected to the cooling process at a cooling rate of 2°C/min. The temperature

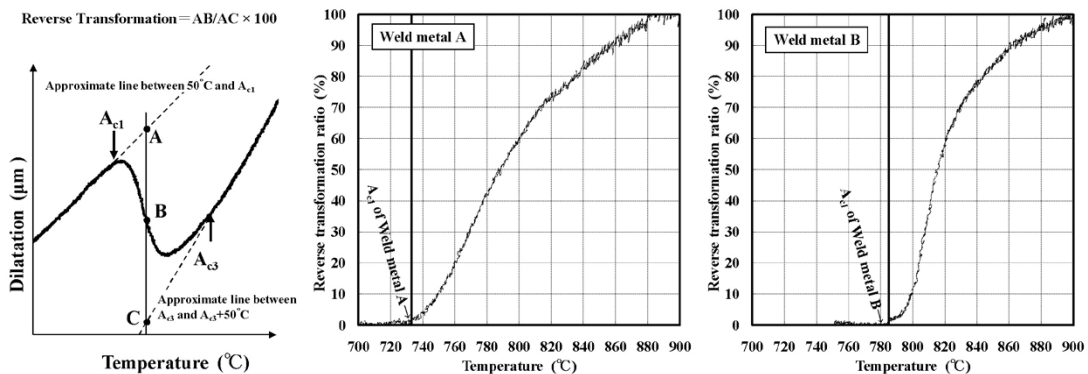


Fig. 5 Relationship between temperature and reverse transformation ratio of weld metals A and B

vs. expansion/contraction curve was measured during the cooling process to confirm the precipitated phase. Fig. 6 shows the results. Weld metal A exhibits a linear expansion behavior, an indication of fresh martensite formation, at around 400°C. Weld metal B, on the other hand, exhibits another linear expansion behavior, an indication of third phase precipitation, at around 750°C. Fig. 7 shows the microstructures of weld metals A and B after this test, and Fig. 8 shows the Kernel Average Misorientation (KAM) images of the respective fields. The KAM images are obtained by electron backscatter diffraction (EBSD) analysis and provide measures of crystal misorientation and lattice strain. A KAM image represents the average crystal misorientations between a pixel and the nearest neighboring pixels in the image, and displays the crystal misorientation distribution in the observed field. Martensite has a large lattice strain in its crystal lattice, enabling the KAM image to discriminate between ferrite and martensite in the microstructure. Comparing weld metals A and B in Fig. 7, it can be seen that the microstructure of weld metal B has a coarse white texture in the perpendicular direction in

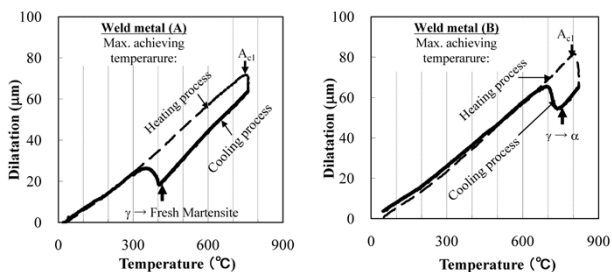


Fig. 6 Phase transformation temperature of weld metals A and B during cooling process

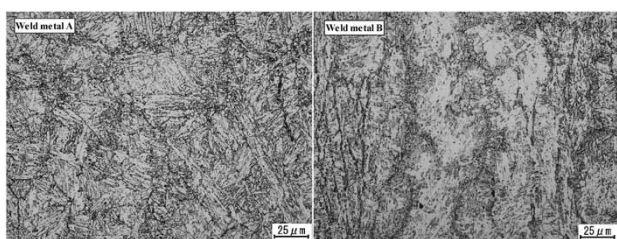


Fig. 7 Microstructures of weld metals A and B after phase transformation temperature analysis

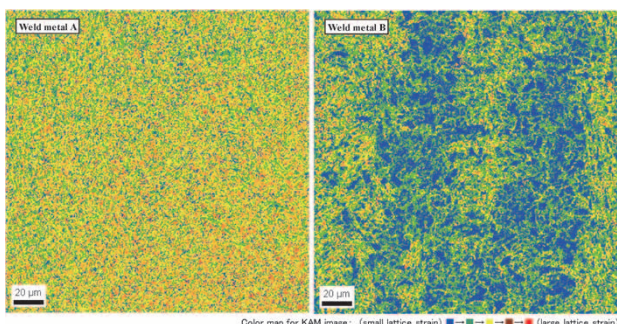


Fig. 8 KAM images of weld metals A and B after phase transformation temperature analysis

the middle of the photograph. This white structure corresponds to the area of concentrated blue in the KAM image of weld metal B shown in Fig. 8, which indicates that the lattice strain of this area is significantly smaller than that of the structure in the surrounding area. This implies that the white structure observed in weld metal B may possibly be ferrite. The identification of this precipitate phase will be pursued further.

The second fact that should be noted is that weld metal A shows a reversal in the relationship between PWHT temperature and creep rupture time under high applied stress, which, however, is not the case for the low applied stress. This is considered to have been caused by the difference between the deformation behavior of the creep rupture test specimens under high stress and that under low stress.<sup>7)</sup> In other words, when a high stress is applied, deformation occurs throughout the entire specimen. Fresh martensite, with highly dense dislocations in its crystal grain, contributes to the prolonged creep rupture time. On the other hand, under a low applied stress, deformation preferentially occurs in the vicinity of prior austenitic grain boundaries. Hence, the fresh martensite is considered not to have contributed to the prolonged creep rupture time.

The above results confirm that the upper limit of allowable PWHT temperature is governed by the mechanical properties, rather than by the  $A_{c1}$  transformation point.

#### 2.4 Effect of PWHT temperature on the precipitation state and composition of carbonitride precipitation in weld metals

An investigation was made regarding the effect of PWHT temperature on the precipitation state and precipitate amount/composition of carbonitride in weld metal A. Fig. 9 shows the TEM images of weld metal A after PWHT at each temperature. No

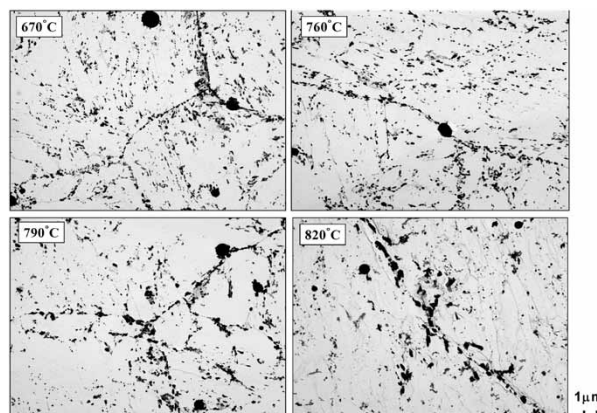


Fig. 9 TEM images of weld metal A after PWHT at different temperatures

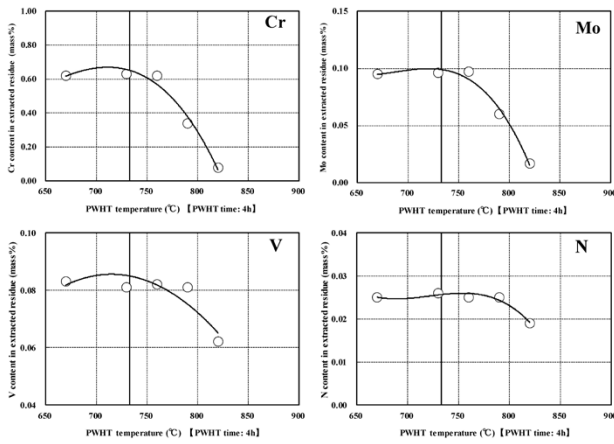


Fig.10 Analysis of extracted residues of weld metal A after PWHT at different temperatures

significant difference was found in the precipitation amount and distribution of carbonitride between the PWHT temperatures of 670°C and 760°C. However, it was clearly observed that the precipitates of intragranular carbonitride are more thinly distributed at 790°C, and the lath carbide on grain boundaries has been coarsened at 820°C.

Extracted residue analysis was conducted to quantitatively compare the precipitation amount of carbonitride at the respective PWHT temperatures. Fig.10 shows the analysis results. It is confirmed that the elements Cr, Mo, V and N all decrease abruptly when the PWHT temperature exceeds 760°C. This is considered to have been caused by the increased PWHT temperature promoting the dissolution of carbonitride into the matrix to form a solid solution.

### 3. The upper limit PWHT temperature allowable for each weld metal

The  $A_{c1}$  transformation points of weld metals A and B were measured and found to be 730°C and 780°C, respectively. If the construction standard that stipulates that the PWHT temperature must be lower than the  $A_{c1}$  transformation point is followed, the upper limits of the PWHT temperature for weld metals A and B should be approximately 730°C and 780°C, respectively. However, the PWHT temperature of 730°C provides weld metal A with tempering insufficient to achieve the desired mechanical properties. In the case of weld metal B, on the other hand, the PWHT temperature of 780°C makes the room-temperature tensile strength almost equal to the lower limit value of the standard for Gr. P91 steel, which raises a concern that the margin against the specification becomes too small. Thus, a PWHT temperature selected merely on the basis of the  $A_{c1}$  transformation point may not be practical. Comprehensive contemplation of

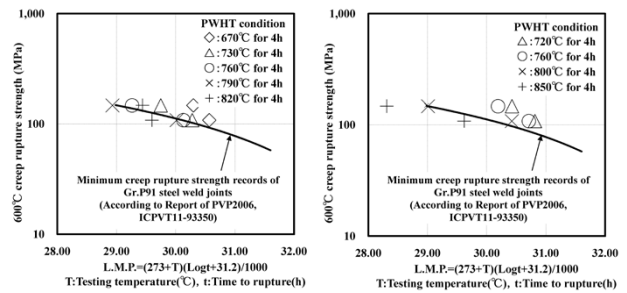


Fig.11 Creep rupture strengths of weld metals A and B after PWHT at different temperatures

mechanical properties is considered to be important in determining the PWHT temperature.

Fig.11 shows the creep rupture strengths of weld metals A and B. The creep master curve for the Gr. P91 steel welded joint is also included. From the results, and now assuming that the weld metal is required to have a creep rupture strength that is equal to or greater than that of the welded joint, the upper limits of the PWHT temperatures for weld metals A and B become 760°C and 800°C respectively.

If the PWHT temperature of 760°C is used for weld metal A, the weld metal exhibits a favorable toughness with its tensile strength at room temperature fully satisfying the specification for Gr. P91 steel. In the case where the PWHT temperature of 800°C is used for weld metal B, the weld metal exhibits a favorable toughness; however, its room-temperature tensile strength has only a small margin against the Gr. P91 steel specification, as described above.

After the comprehensive consideration of mechanical properties based on the above results, the upper limits of the PWHT temperatures for weld metals A and B are concluded to be 760°C and 800°C, respectively.

### Conclusions

Two types of weld metals were prepared using CM-9Cb and CM-95B9, Kobe Steel's covered electrodes designed for ASTM A335 Gr. P91 steel. The weld metals are mainly characterized by their different Mn + Ni content. Each of them was subjected to post weld heat treatment (PWHT) at temperatures above its  $A_{c1}$  transformation point to study its mechanical properties after the heat treatment. There was discussion concerning the upper limit of the PWHT temperature allowable for each of the weld metals. The results show that the amount of Mn+Ni for the CM-9Cb weld metal was 2.49mass%, and the  $A_{c1}$  transformation point was 733°C. In accordance with the construction standard stipulating that the PWHT temperature must be lower than the  $A_{c1}$  transformation point, the upper limit of the PWHT temperature should be 730°C; however, on the basis

of the evaluation results for mechanical properties, a PWHT temperature of up to 760°C is judged to be allowable.

The amount of Mn + Ni for the CM-95B9 weld metal was 1.38mass% and  $A_{c1}$  transformation point was 785°C. If the standard described above is followed, the upper limit of the PWHT temperature should be 780°C; however, on the basis of the evaluation results for mechanical properties, a PWHT temperature of up to 800°C is judged to be allowable.

The above findings indicate that the PWHT temperature for a weld metal of high Cr ferritic heat-resistant steel should not be determined merely on the basis of the Mn + Ni content and/or the  $A_{c1}$  transformation point, but rather should take into consideration the mechanical properties, including creep rupture performance.

The present paper studying the upper limit of the PWHT temperature focuses only on the weld metals. However, more comprehensive research should be done to evaluate the actual welded joints, and this would include a study of the base material and the heat-affected zone of the base material.

## References

- 1) ASME B31.1. POSTWELD HEAT TREATMENT. 2001, 132.1, p.87.
- 2) Thermal and Nuclear Power Engineering Society. The interpretation for the technical standard for thermal power plant [Chapter 10, Welding] [handbook] (Revision H19). 2009, p.159.
- 3) AWS A5.5/A5.5M. 2006. p.8.
- 4) ASTM 1033-4. Standard Practice for Quantitative Measurement and Reporting of Hypoeutectoid Carbon and Low-Alloy Steel Phase Transformations.
- 5) Chen Liang et al. Effect of PWHT temperature and mechanical properties of High-Cr ferritic heat-resistant steel weld metal. *Welding in the World*. 2012, Vol.56, January-February (1-2).
- 6) T. Tokunaga, et al. Phase transformation behavior of Gr. 91 ferritic steel around the  $A_{c1}$  temperature. *CAMP-ISIJ*. 2008, Vol.21, p.1066.
- 7) H. Kushima et al. Degradation of Mod. 9Cr-1Mo Steel during Long-term Creep Deformation. *TETSU-TO-HAGANE* (in Japanese). 1999, Vol.85, No.11, p. 57.

# Built-in Cable Type Welding Robot "ARCMAN™-GS"

Shuichi INADA\*1, Makoto KONDO\*1, Yoshihide INOUE\*1, Tatsuji MINATO\*1, Dr. Yoshiharu NISHIDA\*2, Takashi WADA\*2

\*1 Welding System Dept., Technical Center, Welding Business

\*2 Production Systems Research Laboratory, Technical Development Group

*This paper describes the features of the "ARCMAN™-GS", a welding robot with built-in cables. The robot was launched in the market in September 2011. To reach deep inside hollow workpieces, the robot has a sufficient working area especially designed for an overhead-suspended system and has a torch-integrated arm that is suitable for teaching. These features make the "ARCMAN™-GS" a more versatile robot, enabling the welding of various workpieces and improving the customers' production. The robot is expected to see worldwide sales.*

## Introduction

Kobe Steel's arc welding robots target the fields of medium- and heavy-thick plates, (e.g., construction machinery, buildings steel structures, bridges and rolling stock), and have been widely adopted by domestic and overseas users. The user's needs in these fields include; ① productivity improvement (increased automation rate), ② the improvement of welding quality, ③ space saving and ④ the reduction of production costs.

A specific example of need ① is as follows. In the field of construction machinery, there are many cases where a welding torch enters deep inside a workpiece, increasing the possibility of the welding torch and torch cables interfering with the workpiece. In such a case, welding cannot be done by a robot and must be done by hand. To improve productivity in such a work environment, there has been a need for a "built-in cable type welding robot" with its torch cable running through the upper arm of the robot to avoid interference with the workpiece.

On the other hand, there is a strong need for downsizing and space saving in welding systems, while the workpieces are becoming larger. As a result, there is an increasing demand for overhead-suspended systems that can easily approach large workpieces and save space.

Kobe Steel has therefore developed a built-in cable type robot, the ARCMAN™ (note) -GS (Fig. 1), having the advantages of ① built-in cables, in which the torch cable is much less likely to interfere with the workpiece, and ② a large working area suitable

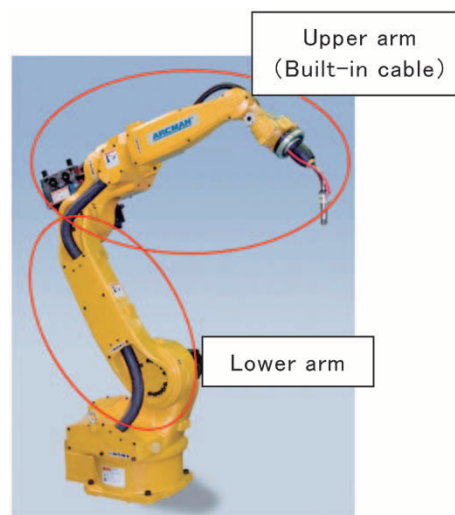


Fig. 1 Appearance of ARCMAN-GS<sup>1)</sup>

for overhead-suspended systems.<sup>1)</sup>

The ARCMAN-GS has a structure newly developed for built-in cables and has mechanical advantages that are different from those of the conventional ARCMAN series. A new control technology was also developed to achieve high position-tracking precision (e.g., weaving precision and sensing precision). The new structure and control technology have realized the development of this new robot with high functioning and high performance.

The name, "ARCMAN-GS", is derived from "Global Standards / Global Strategy" and reflects Kobe Steel's intention to build robots that serve for many users over the world.

## 1. The advantages of ARCMAN-GS

### 1.1 Upper arm types that can be selected to suit the system

The ARCMAN-GS has the following two options for upper arm types:

- ① A type having a welding torch passing through the wrist and torch cables passing through the upper arm (Fig. 2).
- ② A type having a torch passing through the wrist and torch cables not passing through the upper arm (Fig. 3).

Type ①, with the welding torch passing through the wrist and the torch cables passing through the upper arm, significantly decreases the interference

<sup>note)</sup> ARCMAN (ARCMAN™) is a trademark of Kobe Steel, Ltd.

of the cable with the workpiece, compared with conventional robots. Type ② is effective in decreasing interference around the wrist when exchanging the welding torch and torch cable with others, such as in the case of the automatic exchange of single and tandem torches.

Fig. 4 shows a conventional robot, ARCMAN-SR, approaching the workpiece of a construction machine. The problem with a torch approaching a narrow and deep part of the workpiece is that the torch may interfere with the object and the torch cable may become entangled with it. In the example shown, the torch cable, extending from a feeding apparatus, is about to come in contact with the inner surface of the workpiece. By adopting type ① with the built-in torch cable, interference of the torch cable with the workpiece can be avoided. This facilitates the robot teaching operation and is suitable for off-line teaching using a PC.

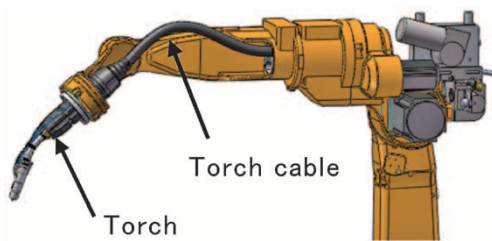


Fig. 2 Upper arm with built-in torch cable

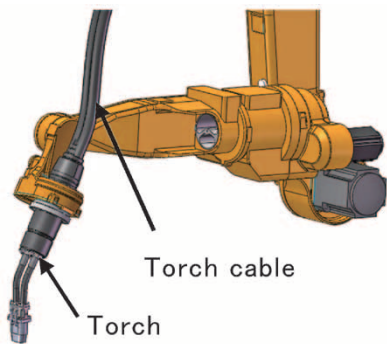


Fig. 3 Torch-integrated wrist axis

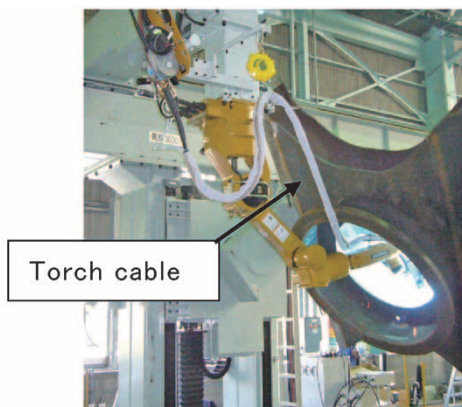


Fig. 4 ARCMAN-SR approaching a construction machine

Type ②, with the torch cable not passing through the upper arm, is adopted when the torch cable cannot be built into the upper arm, such as in the case of the automatic exchange of single and tandem torches described later. Even in this case, the welding torch passes along the center of the S6 axis in the robot axis configuration (Fig. 5) without protruding out of the robot. Thus interference with the workpiece is decreased even when the welding is performed in a narrow and deep part of it.

In order to realize the built-in torch cables described above, a new wrist structure, different from the ones for conventional robots, has been developed.

## 1.2 Newly developed wrist structure

The wrist structure of the ARCMAN-GS comprises an upper arm and a torch cable built into it. The structure has an asymmetric configuration (cantilever) around the S4 axis of the upper arm (Fig. 6) to allow for the automatic exchange of single and tandem torches. It should be noted that a conventional robot (e.g., the ARCMAN-MP) does not have a built-in torch cable and has a symmetric structure around its S4 axis (Fig. 7).

In order to have a built-in torch cable while slimming down the wrist structure, an arrangement that is totally different from the conventional ones

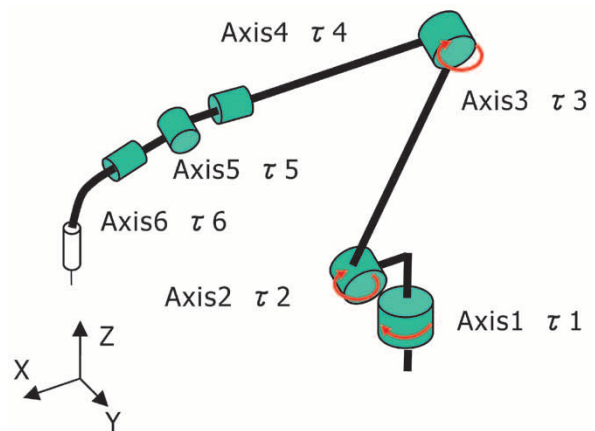


Fig. 5 Torque of each axis

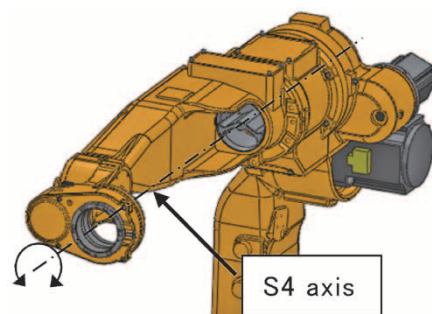


Fig. 6 Asymmetrical wrist of ARCMAN-GS

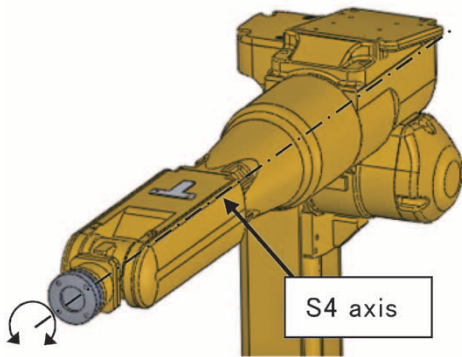


Fig. 7 Symmetrical wrist of conventional robot (ARCMAN-MP)

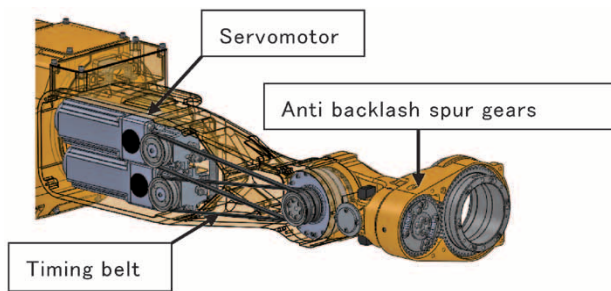


Fig. 8 Wrist structure

has been employed. The new arrangement includes the S5 and S6 axes with their timing belts crossing each other and a new structure with zero backlash spur gears. (Fig. 8)

With the welding torch and torch cable built-in, there is no protrusion at the tip of the wrist, which has realized a structure causing less entanglement of the torch cable and less interference with the workpiece.

### 1.3 Automatic exchange of single and tandem welding torches (tool exchange)

One of the advantages of the ARCMAN series exists in tandem welding (two-electrode welding) that increases the welding efficiency for medium- and heavy- thick plates. The ARCMAN-GS can build-in the tandem torches centered on its S6 axis. The advantage of the robot with a built-in torch cable has improved the application ratio of tandem welding in narrow and deep parts, which has conventionally been impossible. Its combination with the tool exchange exclusively designed for the ARCMAN-GS enables the automatic exchange of single and tandem torches during the welding process, allowing the use of welding torches based on the shapes of the workpieces and joints (Fig. 9).

Fig.10 shows the operation of automatically dismantling a single torch, preparatory as the first step in the automatic exchange. A single torch is fixed on a holder. The mounting and dismantling of

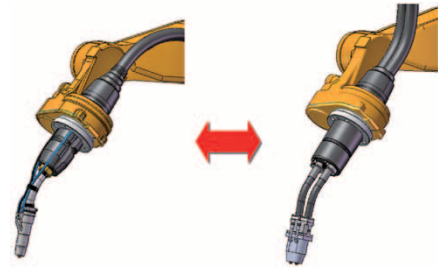


Fig. 9 Single torch (left) and tandem torch (right)

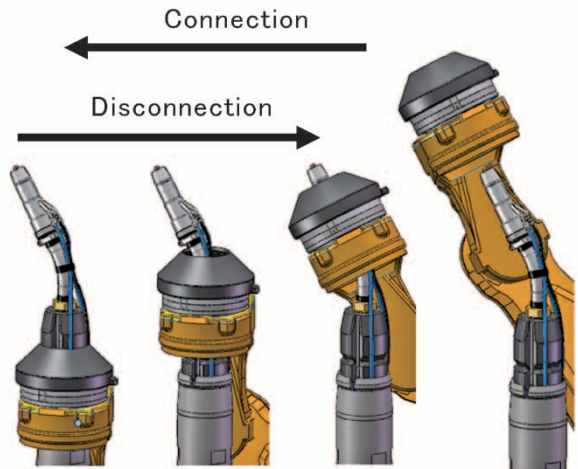


Fig.10 Automatic exchange operation of single torch

the welding torches is done along the S6 axis of the robot from the tip of the torch. By thus automatically exchanging a welding torch for a more suitable one, the application ratio can be maximized.

### 1.4 Reverse-elbow of S3 axis

A posture in which a robot arm is bent such that its upper arm extends to the rear of the robot is called a "reverse-elbow position." In an overhead-suspended system, which is suitable for welding large objects consisting of medium- and heavy-thick plates, this reverse-elbow position is advantageous, providing a larger working area than a conventional robot does when the robot approaches the object from the top.

Fig.11 compares the working areas in overhead-suspended postures of the ARCMAN-GS with those of a conventional robot (ARCMAN-MP). The weldable area (depicted in pink) in the rear of the robot is 40% larger than that of the conventional robot. Thanks to its ability to take the reverse elbow position, the ARCMAN-GS, overhead-suspended, has an enlarged working area despite its arm size being in the same class as the ARCMAN-MP.

Fig.12 shows examples of approaches to a workpiece when using an overhead-suspended system. This comparison shows how, of the two approaches to the same welding location, the

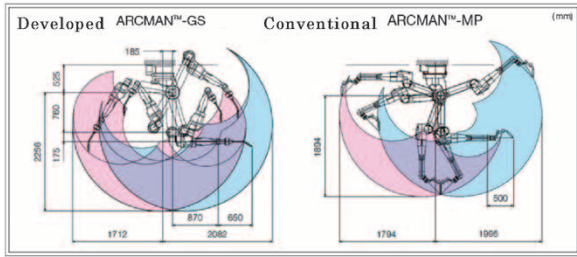


Fig.11 Comparison of working area

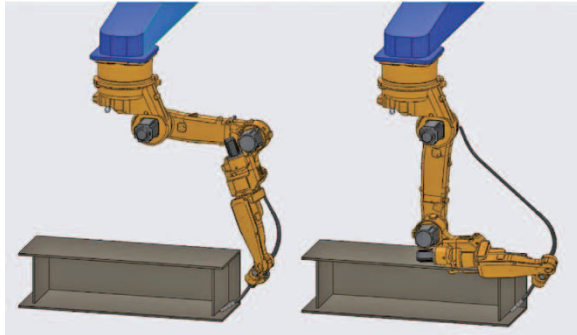


Fig.12 Reverse posture (left) and conventional posture (right)

reverse-elbow capability allows a posture that can take the shape of the workpiece into account and avoid interference. The conventional way of avoiding interference involves once moving the robot away from the workpiece on a moving apparatus (e.g., a cradle for moving the robot itself). The ARCMAN-GS, on the other hand, can avoid interference by a simple motion of the robot without the help of any moving apparatus, which decreases the length of the stroke required for the moving apparatus. This example offers a wider range of possibilities for the space saving and weight reduction of the entire system.

## 2. Development of new control technology

Unlike the conventional ARCMAN series, the ARCMAN-GS has an "asymmetric wrist structure." Therefore, the following new control technology had to be developed to achieve equal or better performance (e.g., weaving precision and sensing precision), important for welding robots used in the field of medium- and heavy-thick plates.

- ① Feed-forward model for six-axis articulated robot
- ② Elastic deformation compensation for six-axis articulated robot
- ③ New backlash compensation
- ④ New coulomb friction compensation
- ⑤ New acceleration/deceleration trajectory

This paper explains only the above ① and ②, due to space limitations.

## 2.1 Feed-forward model for six-axis articulated robot

Assuming that a robot joint is a rigid body, its motion is described by the following general equation.

$$\{J_M + J_L(\theta_M)\} \ddot{\theta}_M + (B_M + B_L) \dot{\theta}_M + C(\dot{\theta}_M, \theta_M) + F = \tau \quad (1)$$

wherein,  $\theta_M$ : motor position

$J_M, J_L(\theta_M)$ : motor inertia, load-side inertia

$B_M, B_L$ : viscosity friction coefficient of the motor,

viscosity friction coefficient of the load-side

$C(\dot{\theta}_M, \theta_M)$ : centrifugal/Coriolis force, gravity

$F$ : external force

$\tau$ : motor torque

Equation (1) is a general equation for only one axis. Conventionally, the axes that significantly affect the position of the robot tip are considered to be only the principal axes (S1 axis to S3 axis), as indicated by equation (2). The ARCMAN-GS has an upsized wrist structure, as well as left-right asymmetry of the upper arm. As a result, it has turned out that the wrist axes (S4 axis to S6 axis) also significantly affect the positioning of the robot tip. Therefore, equation (2) was extended to develop a new model that takes account of all the axes (equation (3)).

Equation (3) is used to calculate, in advance, the torque that would be required at the time of operation so as to add the calculation result to the control system as feed forward. This has achieved a high degree of position-tracking accuracy. The originally derived model required a large quantity of computation, involving approximately twenty thousand calculations, which made it difficult to implement the model on a robot controller. Repeated verification of the equation on an actual robot has decreased the amount of computation to one-twentieth of what it was, which has enabled implementation on the controller.

### (1) Conventional control law

$$\begin{bmatrix} \tau_1 \\ \tau_2 \\ \tau_3 \end{bmatrix} = \begin{bmatrix} J_{11} & J_{12} & J_{13} \\ J_{21} & J_{22} & J_{23} \\ J_{31} & J_{32} & J_{33} \end{bmatrix} \begin{bmatrix} \ddot{\theta}_1 \\ \ddot{\theta}_2 \\ \ddot{\theta}_3 \end{bmatrix} + \begin{bmatrix} B_1 & 0 & 0 \\ 0 & B_2 & 0 \\ 0 & 0 & B_3 \end{bmatrix} \begin{bmatrix} \dot{\theta}_1 \\ \dot{\theta}_2 \\ \dot{\theta}_3 \end{bmatrix} + C(\theta_1, \theta_2, \theta_3) + F \quad (2)$$

### (2) New control law

$$\begin{bmatrix} \tau_1 \\ \tau_2 \\ \tau_3 \\ \tau_4 \\ \tau_5 \\ \tau_6 \end{bmatrix} = \begin{bmatrix} J_{11} & J_{12} & J_{13} & J_{14} & J_{15} & J_{16} \\ J_{21} & J_{22} & J_{23} & J_{24} & J_{25} & J_{26} \\ J_{31} & J_{32} & J_{33} & J_{34} & J_{35} & J_{36} \\ J_{41} & J_{42} & J_{43} & J_{44} & J_{45} & J_{46} \\ J_{51} & J_{52} & J_{53} & J_{54} & J_{55} & J_{56} \\ J_{61} & J_{62} & J_{63} & J_{64} & J_{65} & J_{66} \end{bmatrix} \begin{bmatrix} \ddot{\theta}_1 \\ \ddot{\theta}_2 \\ \ddot{\theta}_3 \\ \ddot{\theta}_4 \\ \ddot{\theta}_5 \\ \ddot{\theta}_6 \end{bmatrix} + \begin{bmatrix} B_1 & 0 & 0 & 0 & 0 & 0 \\ 0 & B_2 & 0 & 0 & 0 & 0 \\ 0 & 0 & B_3 & 0 & 0 & 0 \\ 0 & 0 & 0 & B_4 & 0 & 0 \\ 0 & 0 & 0 & 0 & B_5 & 0 \\ 0 & 0 & 0 & 0 & 0 & B_6 \end{bmatrix} \begin{bmatrix} \dot{\theta}_1 \\ \dot{\theta}_2 \\ \dot{\theta}_3 \\ \dot{\theta}_4 \\ \dot{\theta}_5 \\ \dot{\theta}_6 \end{bmatrix} + C(\theta_1, \theta_2, \theta_3, \theta_4, \theta_5, \theta_6) + F \quad (3)$$

The torque at the tip (S6 axis) during the operation of all axes was estimated, and the results are shown in Fig.13 and Fig.14. The conventional control technique, adapted to the ARCMAN-GS, has caused a difference between the estimated torque value and feedback torque (Fig.13). On the

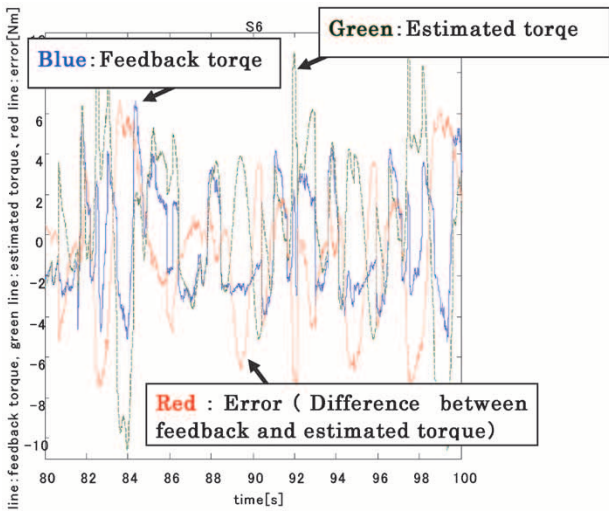


Fig.13 Estimated torque with existing control (Axis 6)

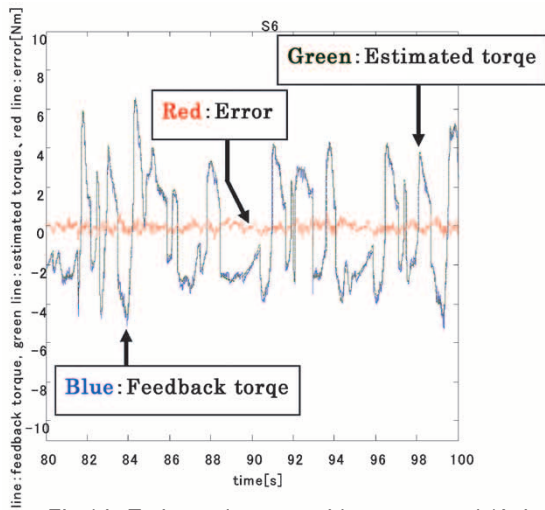


Fig.14 Estimated torque with new control (Axis 6)

other hand, it has been verified that the new control technique accurately estimates the torque (Fig.14). This torque, accurately estimated, has been added to the control system as feed-forward to achieve high precision in position tracking.

## 2.2 Elastic deformation compensation for six-axis articulated robot

The effects of the strain placed on the wrist portion, due to its increased weight and complexity, have made it more difficult for the ARCMAN-GS to ensure the weaving precision of the robot. Therefore, the predictive control of strain was extended from the conventional 3 axes to 6 axes (equation (4)). This has made it possible to secure the weaving precision required.

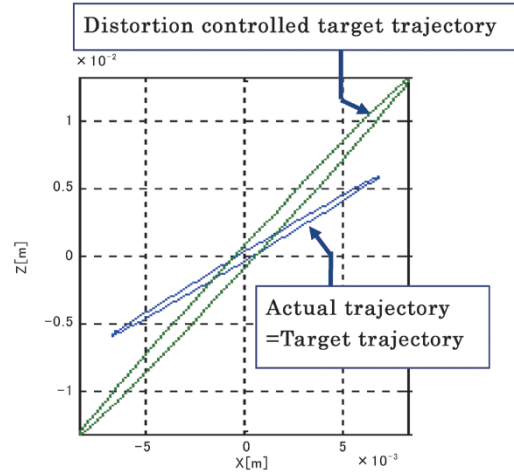


Fig.15 Prediction result with new control

$$\begin{bmatrix} \Delta\theta_1 \\ \Delta\theta_2 \\ \Delta\theta_3 \\ \Delta\theta_4 \\ \Delta\theta_5 \\ \Delta\theta_6 \end{bmatrix} = \begin{bmatrix} K_1^{-1} & 0 & 0 & 0 & 0 & 0 \\ 0 & K_2^{-1} & 0 & 0 & 0 & 0 \\ 0 & 0 & K_3^{-1} & 0 & 0 & 0 \\ 0 & 0 & 0 & K_4^{-1} & 0 & 0 \\ 0 & 0 & 0 & 0 & K_5^{-1} & 0 \\ 0 & 0 & 0 & 0 & 0 & K_6^{-1} \end{bmatrix} \begin{bmatrix} \tau_1 \\ \tau_2 \\ \tau_3 \\ \tau_4 \\ \tau_5 \\ \tau_6 \end{bmatrix} \dots \dots \dots (4)$$

wherein  $K$  represents the spring constant.

The above model enables the prediction of strain in the robot arm, allowing the ARCMAN-GS to track the desired trajectory with its robot tip.<sup>2)</sup> Fig.15 shows a result of the predictive control as an example. The horizontal axis is the coordinate in the X direction, while the vertical axis is the coordinate in the Z direction, of the robot tip (See Fig. 5). When the robot tip is aimed so as to move along an oblique angle of 45 degrees, the target trajectory of strain prediction falls on the solid green line. When the robot is operated with this green trajectory as a target, the actual trajectory falls on the angle of 45 degrees, indicated by the solid blue line, as targeted. This verifies the precision of the strain prediction.

## Conclusions

In the development of the ARCMAN-GS, new machine technology and new control technology were integrated to create a world-class robot. We will strive to improve the technology to develop high performance robots by exploiting the experience acquired through this study.

## References

- 1) T. Minato Technical Guide, Technical Report. 2011-9, Vol.51, p.1-6.
- 2) Y. Nishida et al. "Motion control of arc welding robot for medium- and heavy-thick plates" Journal of the Society of Instrument and Control Engineers (Journal of SICE). 2012, Vol.51, No.9.

# Development and Approach to Future Market of the Eco-Radial Steam Turbine Generator

Atsushi YOSHIDA \*1, Osamu MATSUTANI \*2

\*1 Refrigeration System & Energy Dept., Compressor Div., Machinery Business

\*2 Shinko Engineering Co., Ltd.

*A new power generation system, the Eco-Radial, has been developed and launched into the market. The system employs a radial turbine, designed for steam pressure up to 0.98MPaG. The manufacturing cost has been cut to 50% of the conventional cost as a result of various efforts such as downsizing, reducing the number of components and decreasing the machining time. This paper introduces the development of this new model and our approach to the future market.*

## Introduction

Kobe Steel originally developed an expansion turbine for the cold generation unit of an air separation system in 1934, launched a steam turbine in 1987, and since has been striving to promote the business of various turbines as professional energy-saving machines. The company has designed and built non-general-purpose radial turbines that can be used, not only for steam, but also for various other gases. Those gases include exhaust gas from the reactors of chemical plants, ammonia gas mixed with water—the gas mixture used for the Kalina cycle for recovering mid-to-low-temperature exhaust heat—liquefied natural gas and city gas. These radial turbines have been favorably received by many users.

Being tailor-made, however, these non-general-purpose turbines are rather costly and have been delivered only to a limited number of customers.

With this background, Kobe Steel has developed and launched a small power generating system (hereinafter referred to as the Eco-Radial <sup>note 1)</sup>) equipped with a general-purpose radial turbine. This system is designed for boiler steam at pressures up to 0.98MPaG, the pressure range commonly used by many users. The newly developed turbine maintains the high efficiency that is an advantage of radial turbines and is less costly. This paper outlines the development of the Eco-Radial and introduces its future market.

note 1) Eco-Radial is a Kobe Steel's trademark registered in Japan.

## 1. Advantages of non-general-purpose radial turbines developed by Kobe Steel

### 1.1 High efficiency

Turbines are generally classified into an axial-flow type and a radial-flow type. Kobe Steel adapted a radial-flow type (hereinafter, a "radial turbine"). This radial turbine comprises a built-in reduction gear that makes the speed ratio between its high-speed shaft and low-speed shaft selectable. Optimizing the rotational speed of the high-speed shaft, having a turbine impeller (hereinafter, a runner) at its end, ensures high efficiency.<sup>1)-3)</sup> Fig. 1 compares the structures of an axial turbine and a radial turbine, and Fig. 2 shows the power they generate under certain conditions. As shown, the radial turbine is superior to the axial turbine for the conditions of low pressure and small output power.

### 1.2 High reliability

One of the advantages of a radial turbine is its small number of components. For example, an axial turbine has an impeller with several tens of blades

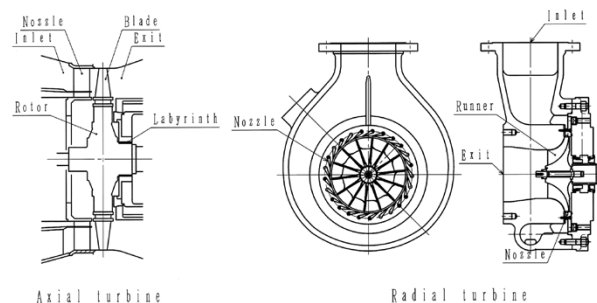


Fig. 1 Comparison of axial turbine and radial turbine

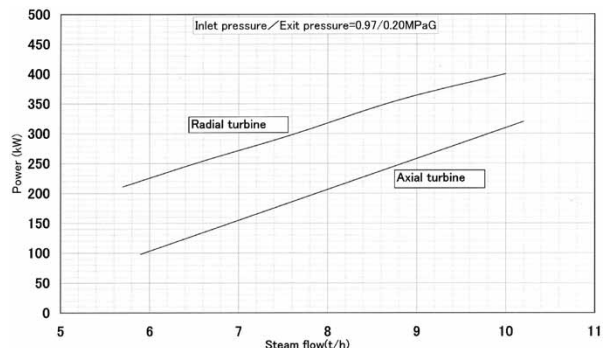


Fig. 2 Power comparison of Eco-Radial and axial turbine

embedded. A radial turbine, on the other hand, has an impeller (runner) incorporating blades that are machined out from a forging stock as a unit, all together comprising a single component. This impeller is attached to an end of a high-speed shaft rotor, which contains fewer than ten components in total. The small number of components results in a simple mechanical structure with the advantage of more easily securing greater reliability.

### 1.3 High durability

Kobe Steel's first machine, a small turbine for 500kW class generator, is still running smoothly at a plant owned by the customer. For fluids other than steam, there are many machines that have been running for over thirty years.<sup>4)</sup>

## 2. Development of Eco-Radial

### 2.1 Developmental background

In order to cope with global warming and with the power supply problem after the Great East Japan Earthquake, improving power self-sufficiency has become a major industrial issue. In 2007, Kobe Steel began selling a small screw-type steam generator, the STEAMSTAR™ MSEG™<sup>note 2)</sup> and since then has delivered more than seventy units. Recently, with the increasing demand for power saving, there have been new projects to save power using several generators of the 160kW class. In order to respond to such a high-end market for the STEAMSTAR MSEG, Kobe Steel started to downsize a conventional steam generator—a non-general-purpose type equipped with a radial turbine—to develop a new general-purpose generator, the Eco-Radial (model number: GRT160e, maximum output 400kW), which is a unit type and is less costly. **Table 1** shows the design specifications of the Eco-Radial.

### 2.2 Generalization and cost reduction

This development project has primarily aims at significantly reducing the cost while achieving a high efficiency that is an advantage of radial turbines. Specific measures for the cost reduction include commonizing components by generalizing the purposes within the scope of the applications of the developed machine, reducing the weight of each component and simplifying the structure. Such commonization includes large castings, such as

<sup>note 2)</sup> STEAMSTAR and MSEG are trademarks of Kobe Steel.

Table 1 Specifications of Eco-Radial

	Eco-Radial (GRT160e)
Inlet condition:	
Max. pressure (MPaG)	0.97
Max temperature (°C)	210
Exit pressure (MPaG)	0~0.5
Steam flow (t/h)	2.5~10.0
Max. power (kW)	400
Generator type	Induce
Size(mm)	1,900×3,500×1,900
Weight(kg)	3,500
Control system	4 options with inlet valve (power, inlet pressure, exit pressure or flow constant control)

gear casings and turbine casings, which have been commonized to perpetuate the wooden models used for the casting and thus to reduce the cost of these models. As a result, the production cost has been reduced to approximately 50% of the conventional cost.

The following section outlines the cost-reduction measures for the major components of a radial turbine, i.e., a turbine runner and turbine nozzles.

### 2.3 Reducing the number of turbine-runner blades and turbine nozzles

Among the various components that constitute a turbine, the turbine runner is the most costly to machine. This component, however, affects the turbine performance directly; hence no major effort has hitherto been made to reduce its cost. For the same reason, not much effort has been made to reduce the cost of the turbine nozzles. This project has aimed at significantly reducing these costs, while minimizing the adverse effect on the turbine performance. Studies were conducted to reduce the machining cost by decreasing the number of the turbine-runner blades and turbine nozzles.

#### 2.3.1 Reduction of machining time

Decreasing the numbers of the turbine-runner blades and turbine nozzles increases the area of the gas passages inside these components. This enables the use of drill bits with large diameters when machining, which can reduce the machining time. In the present project, these numbers were reduced as shown in **Table 2**, which reduced their machining costs to approximately 60% of what they had been.

#### 2.3.2 Verification of turbine performance using actual machine

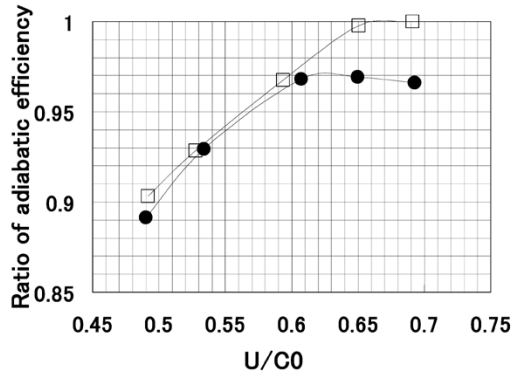
In order to verify the performance of the turbine

Table 2 Processing cost comparison of Eco-Radial and original

	Number of runner blades	Number of nozzles	Processing cost
Eco-Radial	11	14	60%
Original	14	26	100%

Table 3 Test condition

Inlet pressure (MPaA)	Inlet temperature (°C)	Exit pressure (MPaA)	Test Gas
0.3221	184	0.12	Air



□ : Runner blade number =14+Nozzle number =26 (Original)  
 ● : Runner blade number =11+Nozzle number =14 (Eco-Radial)  
 U/CO : Dimensionless number showing turbine operation condition

Fig. 3 Test result of turbine performance (Ratio of adiabatic efficiency vs. U/CO)

with its numbers of runner blades and nozzles reduced, tests were conducted using an actual machine loaded with air. Table 3 shows the test conditions.

The test results verify that the turbine with a decreased number of blades and nozzles exhibits, at maximum, approximately 97% of the efficiency of the conventional turbine (Fig. 3). From these results, it has been judged that the effect of the reduced number of blades and nozzles on the turbine performance falls within an acceptable limit.

### 2.3.3 Verification of turbine performance by CFD analysis

As described in 2.3.2, the reduced numbers of the turbine-runner blades and turbine nozzles were found to cause a drop in turbine efficiency, although the decrease is within an acceptable limit quantitatively.

A computational fluid dynamics (CFD) analysis was performed to clarify the main cause of the efficiency drop.

(1) The effect of the reduced number of nozzles on the turbine efficiency

A test on an actual machine has revealed that

the reduced number of nozzles affects the turbine efficiency only slightly. Therefore, the number of nozzles was set at the conventional number (26 nozzles) in the model for this CFD analysis.

(2) CFD analysis model and analysis conditions

The analysis object (range of modeling) consists of a series of flow passages including turbine nozzles, a turbine-runner, outlet pipe and straight pipe (up to the pressure measuring port on the outlet side for the test run on an actual machine) (Fig. 4). The analysis conditions were as follows:

- Software used: ANSYS FLUENT R13
- Fundamental equations: Equation of continuity, Navier-Stokes equation, Energy equation
- Turbulence model: k-ε SST2 equation model
- Boundary condition : The same as the actual machine testing condition (Table 3)
- Other conditions including rotational speed:

Table 4

It should be noted that the numbers of the runner blades were set at 14, the conventional number, and 9. Both of these numbers are different from the number 11, which was used for the test run on the actual machine. This is because conducting analyses on two conditions with vastly different numbers of blades is expected to clarify the cause for the efficiency drop.

(3) Analysis results

As for turbine efficiency, the analysis qualitatively yielded almost the same result as the

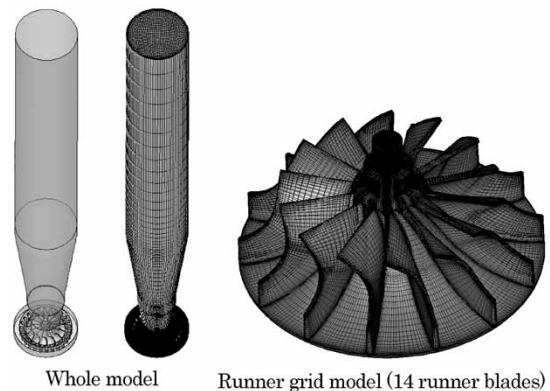


Fig. 4 Analysis model

Table 4 Analysis conditions

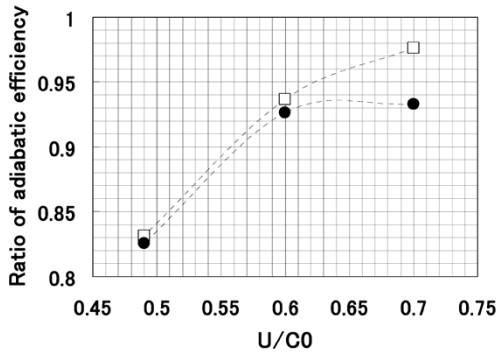
Case	U/CO	Rotation speed (rpm)	Number of runner blades
Case1	0.7	39,800	14
Case2	0.6	34,000	14
Case3	0.49	27,200	14
Case4	0.7	39,800	9
Case5	0.6	34,000	9
Case6	0.49	27,200	9

Number of nozzles : 26 in all cases

test run on the actual machine (Fig. 5). From the analysis results shown in Fig. 6, the relative flow velocity at the runner outlet is as follows:

- For  $U/C_0 = 0.7$

The relative flow velocity at the outlet suction surface near the shroud side was approximately 200m/s when the number of the blades was 14. When the number of the blades



- : Runner blade number =14 + Nozzle number =26 (Original)
- : Runner blade number =11 + Nozzle number =14 (Eco-Radial)
- U/C0 : Dimensionless number showing turbine operation condition

Fig. 5 Turbine performance curve by CFD analysis (Ratio of adiabatic efficiency vs.  $U/C_0$ )

was 9, on the other hand, it became 0 to 15m/s, indicating the existence of a low speed region (separated flow region).

- For  $U/C_0 = 0.6$  and  $0.49$

The flow-velocity profile at the outlet was barely affected by the number of blades.

- (4) Summary of the effect of the number of runner blades

**Table 5** summarizes the differences in the efficiency ratio and relative flow velocity profile at the runner outlet between 14 blades and 9 blades. From this, it is considered that there is a qualitative relationship (or effect) on the efficiency ratio and relative flow velocity profile at the runner outlet when the number of blades is decreased from 14 to 9.

- (5) The reason for the efficiency drop caused by the reduced number of runner blades

From the description in (4), the cause of the efficiency drop when the number of blades is reduced is considered to be related to the difference in the relative flow velocity profiles at the runner outlet. In the case of  $U/C_0 = 0.7$ , in which the difference in efficiency is large, the effect of the low speed region (separated flow region) generated at

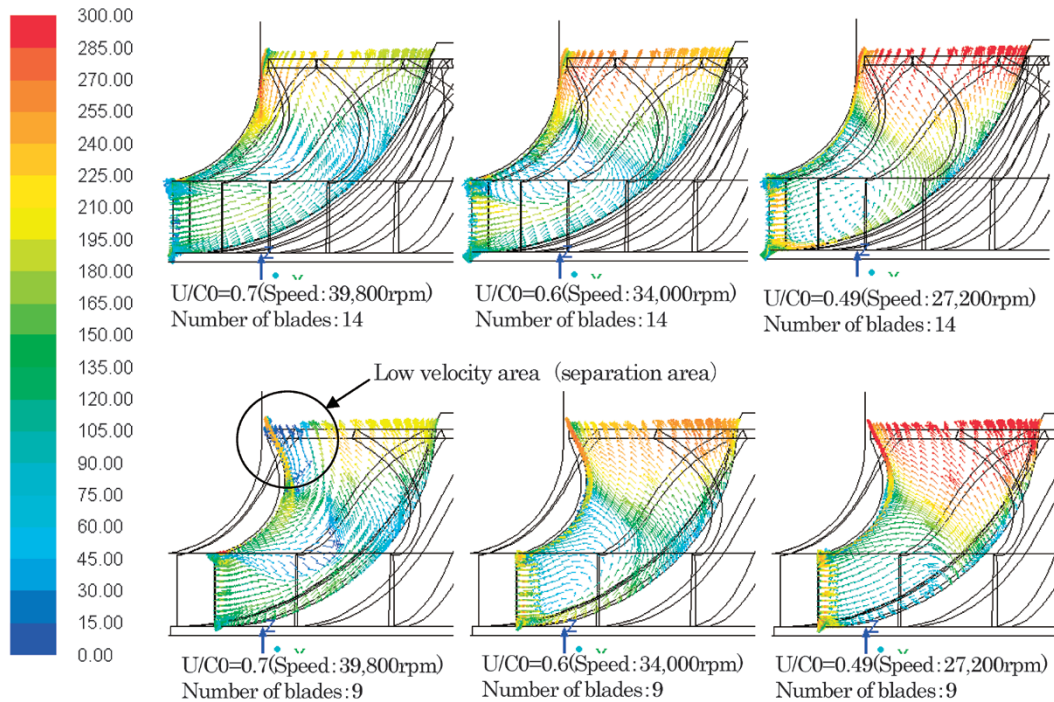


Fig. 6 Relative velocity profile near suction meridian surface by CFD analysis

Table 5 Relationship between difference of efficiency ratio and difference of relative velocity profile at runner outlet

U/C0	Difference of efficiency ratio between 14 blades and 9 blades in measured result	Difference of efficiency ratio between 14 blades and 9 blades in analytical result	Difference of relative velocity profile between 14 blades and 9 blades in analytical result
0.7	big	big	big
0.6	small	small	small
0.49	small	small	small

the outlet suction surface near the shroud side is considered to be rather significant.

## 2.4 Test operation loaded with steam

In order to verify the mechanical stability during actual-load operation, the shaft vibration, bearing temperature, leakage and the like were confirmed on an Eco-Radial operated with steam generated by a boiler. The results verified that there was no operational problem.

## 2.5 Summary of Eco-Radial development

- ① The production cost has been reduced to approximately 50% of the conventional cost, achieving the original goal.
- ② As a way of reducing cost, the numbers of the runner blades and nozzles were decreased. The resulting decrease in turbine performance was verified as falling within an acceptable limit.
- ③ From the CFD analysis, the decreased turbine performance caused by the reduction in the number of runner blades was considered to be attributable to the low speed region (separated flow region) generated at the outlet suction surface near the shroud side. This presumption is considered to be useful in designing special runners based on the current runners and in developing new runners.

## 3. Advantages of Eco-Radial

Fig. 7 shows the outline of the Eco-Radial package. Fig. 8 compares the appearance of Eco-Radial package with that of the conventional package of Kobe Steel's non-general-purpose radial turbine (gas recovery turbine; GRT). The Eco-Radial is a compact package including the turbine body, generator, piping, miscellaneous devices, and supplemental equipment such as a control panel, all installed on a common base. As a result, the new package has a smaller foot print than Kobe Steel's conventional radial turbines and reduces the period and cost of the fieldwork, including piping. Standard equipment includes Kobe Steel's original control monitor system, Kobenicle,<sup>® note 3)</sup> which facilitates maintenance. Kobenicle provides remote 24hr monitoring of operation conditions and alarms. In addition, it can record and store operational data for one year, which is quite useful for long-term operational management, including repair and maintenance.

note 3) Kobenicle is a registered trademark of Kobe Steel.

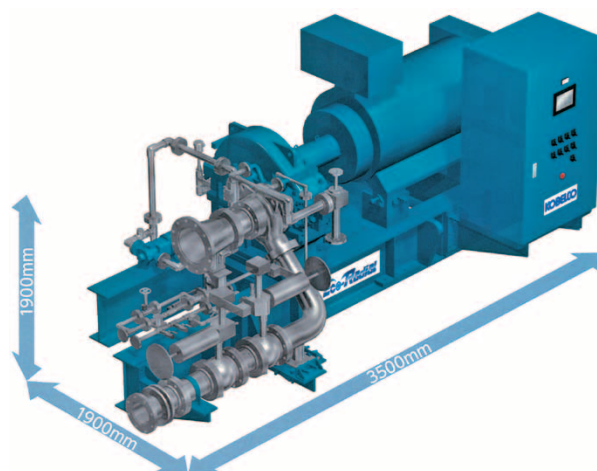


Fig. 7 Eco-Radial outline

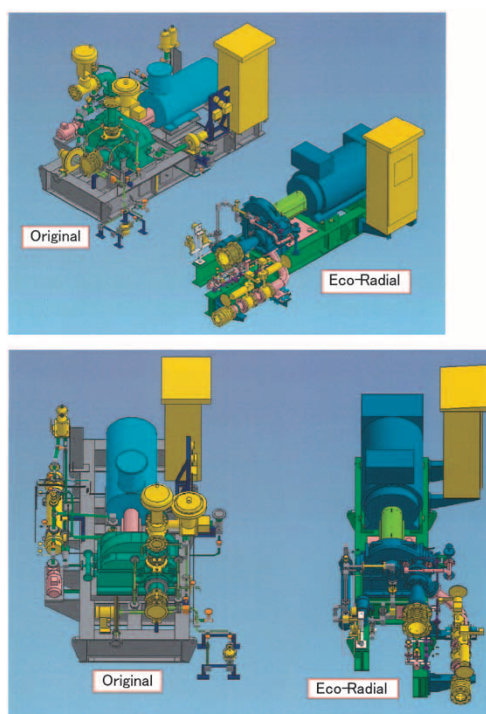


Fig. 8 Outline comparison of original machine and Eco-Radial

## 4. Applications of Eco-Radial

Fig. 9 shows an example of the application of the Eco-Radial. The Eco-Radial can generate electricity from unused energy using, for example, the surplus steam of factories. It can also be used as an alternative for pressure-reducing valves for process steam. The turbine is used as a key component of a small driver for a compressor, or for a pump. Outside Japan, there is a larger amount of unused steam, such as the exhaust steam from small-scale waste incineration plants. Thus, overseas applications will also be considered.

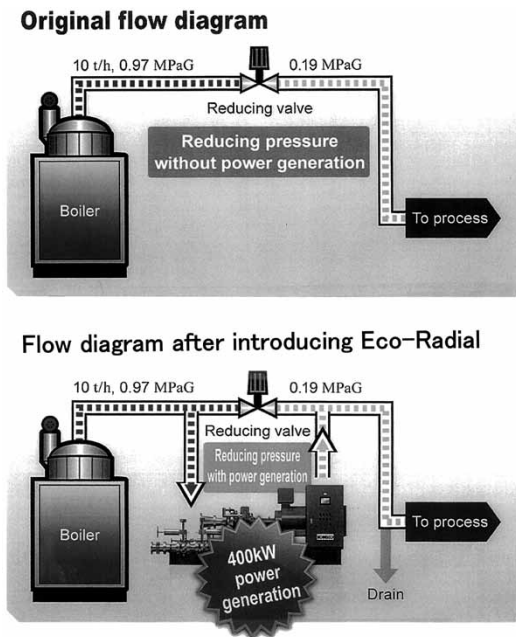


Fig. 9 Example of Eco-Radial application

## 5. Future initiative

### 5.1 Understanding market trends and optimizing specifications

Kobe Steel's non-general-purpose radial turbines can be used at pressures up to 45barG, temperatures up to 400°C and power output up to 6,000kW, judging from the company's experience. The specifications of Eco-Radial can be optimized, without many technical issues, for ever-changing market trends both domestic and abroad. We will focus on markets with high needs, aiming to establish new specifications for Eco-Radial.

### 5.2 Measures against varying amount of steam

The efficiency of radial turbines is decreased during operation at off-design point (partial load), a type of operation caused by the varying amount of steam. In order to suppress this, our non-general-purpose radial turbines are equipped with "variable nozzle mechanisms." Eco-Radial, on the other hand, is not equipped with any variable nozzle mechanism, because that may enlarge the package size, increasing the number of components and complicating the structure. To alleviate the efficiency drop during operation at off-design point due to the varying amount of steam, an Eco-Radial may be combined with a "STEAMSTAR MSEG" (small steam generator) into a system, the latter being a displacement-type rotating machine, and then the efficiency is much less susceptible to operations at off-design point. The idea is to run Eco-Radial by

base-load steam with a constant flow rate and to run STEAMSTAR MSEG by the varying steam. This makes it possible to deal with a varying amount of steam while maintaining high efficiency.

### 5.3 Activity for dissemination

The Eco-Radial product now sells at about half the price of the power generating system based on Kobe Steel's conventional non-general-purpose radial turbine. We will continue to strive to satisfy our customers' needs and to further reduce the cost. This product was originally designed as a unit for power generating systems; however, it can be used as a pump unit and blower unit by changing the driven unit from a generator to a pump or a blower, respectively. It can also be used as a driver unit (a steam motor) including the end of the output shaft of the reduction gears. Further cost reduction is possible by fixing the major core components of the product while developing models derived from applications thus, bringing the volume effect on production into play. We will continue to develop new models while addressing the market needs.

## Conclusions

Kobe Steel owns and is expanding a line-up of products that serves to recover and reuse various types of waste energy: i.e., "STEAMSTAR MSEG", "Microbinary" (the currently sold model is a hot-water-heat-source type, and a steam-heat-source type is being developed), a high-efficiency steam supply system "Steam Grow Heatpump (SGH<sup>note 4)</sup>" which has already been commercialized, a small steam compressor, "STEAMSTAR MSRC," and a steam driven air compressor, "Kobelion<sup>note 5)</sup> -SD". We will strive to further expand and improve our product menu in anticipation of market expansion and will contribute globally to energy-saving and the effective use of unused energy.

## References

- 1) H. Suzuki. *R&D Kobe Steel Engineering Reports*. 1999, Vol. 49, No. 1, p.25-27.
- 2) T. Matsumoto. *R&D Kobe Steel Engineering Reports*. 2006, Vol. 56, No. 2, p.43-46.
- 3) O. MATSUTANI, et al. *R&D Kobe Steel Engineering Reports*. 2009, Vol. 59, No. 2, p.40-44.
- 4) O. MATSUTANI. *R&D Kobe Steel Engineering Reports*. 2009, Vol. 59, No. 3, p.43-46.

note 4) Steam Grow Heatpump and SGH are Kobe Steel's trademarks registered in Japan.

note 5) Kobelion is a Kobe Steel's trademark registered in Japan.

# Manufacturing Technology of Diffusion-bonded Compact Heat Exchanger (DCHE)

Yasutake MIWA \*1, Dr. Koji NOISHIKI \*1, Tomohiro SUZUKI \*2, Kenichi TAKATSUKI \*2

\*1 Products Development Dept., Development Center, Machinery Business

\*2 Takasago Equipment Plant, Energy & Nuclear Equipment Div., Machinery Business

*The Diffusion-bonded Compact Heat Exchanger (DCHE) is a compact heat exchanger, and the demand for it is expected to increase in applications for weight saving or those calling for a compact plot area, as well as for use in floating plants. Kobe Steel has been working on the development and establishment of the manufacturing technology of DCHE, which is a compact and high strength micro channel heat exchanger. Its heat transfer performance has been evaluated by comparing it with the conventional shell & tube type heat exchanger, and its strength and fatigue have been evaluated using Kobe Steel's stress analysis technology and fatigue test. This paper introduces the features of DCHE and the activity involved in its development.*

## Introduction

The number of marine resource projects that require equipment with a small footprint and high efficiency is increasing. Thus, high-efficiency compact heat exchangers designed for floating plants are gathering increasing attention. These compact heat exchangers include microchannel heat exchangers with flow passages, each several millimeters in size, to ensure a large heat transfer area per unit volume.<sup>1)</sup> Such microchannel heat exchangers can be made small in size and will contribute to weight reduction.

Kobe Steel has over 40 years of experience in delivering brazed aluminum plate-fin heat exchangers (hereinafter, ALEXs<sup>®</sup>, note)). Adapting their design and manufacturing technologies,<sup>2)</sup> the company has developed a diffusion-bonded compact heat exchanger (hereinafter DCHE).

This paper introduces the structure and features of DCHEs and reports the verification results for their heat transfer performance and mechanical strength.

## 1. Structure and features of DCHE

### 1.1 Structure of DCHE (comparison between ALEX and DCHE)

An ALEX comprises a brazed core body for exchanging heat and a header/nozzle for guiding

fluid inside the core (Fig. 1). The core body includes multiple assemblies, each consisting of a parting sheet, fin and side bar (Fig. 2), which are cut out in the required sizes. These assemblies are stacked and brazed together in a vacuum furnace to constitute the core body. To ensure sound brazing and weight reduction, aluminum alloy is used as the material.

The production process of a DCHE is shown in Fig. 3. A DCHE has a stacked structure similar to that of an ALEX and is produced in almost the same manner, but with some significant differences in the flow-passage fabrication and joining. The flow passages of a DCHE are fabricated by chemical etching done directly on the material plates, rather than by fin forming. Thus each layer consists of only one plate, which facilitates assembly by stacking.

The joining is accomplished by diffusion bonding, which can offer stronger joints than brazing. The plate material depends on the application. For example, stainless steel, having a strength and corrosion resistance higher than those of aluminum alloy, is used for applications in which an ALEX cannot be used.

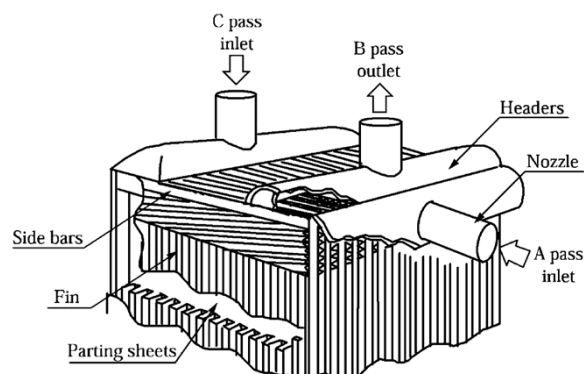


Fig. 1 Structure image of ALEX

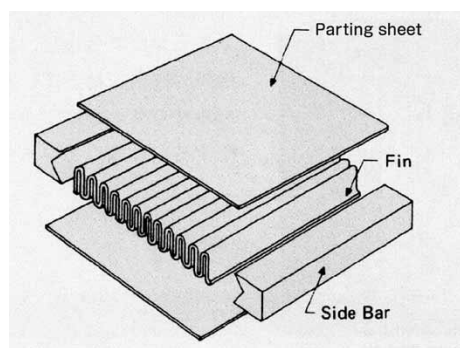


Fig. 2 Main parts of ALEX

note) ALEX is a registered trademark of Kobe Steel.

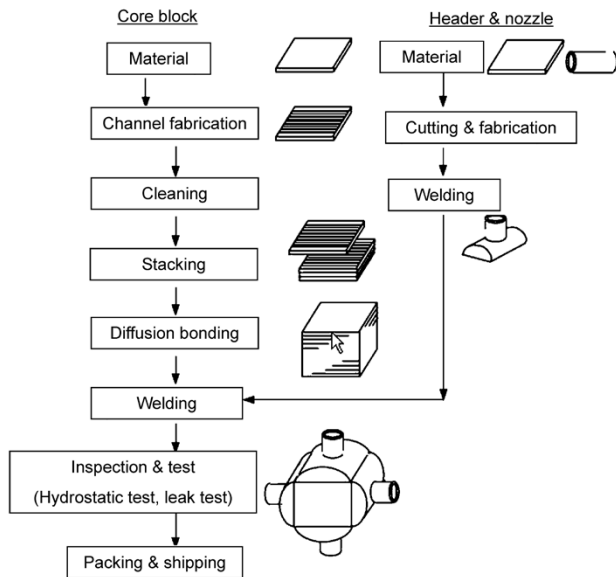


Fig. 3 Manufacturing flow of DCHE

### 1.2 Advantages of DCHE

A DCHE is based on the design and production technologies of the ALEX and has the advantage of possessing the capability of exchanging heat among several fluids at a time.<sup>3)</sup> Fig. 4 schematically shows an example in which three fluids are involved. As shown, optimizing the design for the flow passage of each fluid in accordance with its processing conditions permits one heat exchanger to exchange heat among several fluids. This makes it possible to unify a number of multitubular heat exchangers.

Several materials, including stainless steel, nickel-base alloy and titanium, have so far been evaluated for their flow-passage fabrication and bonding performance. The use of stainless steel enables the flow passages to be made several millimeters in size with thin walls, thanks to its high strength. As a result, excellent heat-transfer performance is expected even when stainless steel is used, in spite of its relatively poor thermal conductivity.

Furthermore, diffusion bonding ensures a joining strength higher than that achieved by brazing, making it possible to use the DCHE in applications to which ALEX has been inapplicable: for example, applications involving high pressure (13MPa or higher) and/or with operational fluctuations.

### 1.3 Applications of DCHE

A DCHE is a heat exchanger that can handle several fluids at a time and is used, depending on its material and the size of its flow passage, up to the designed pressure of 100MPa and design temperature of 900°C. The following describes possible applications:

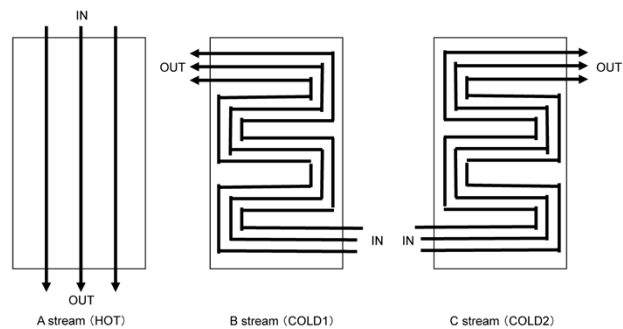


Fig. 4 Stream images of multi pass (3 stream examples)

- (1) Equipment requiring compactness, such as offshore facilities  
 Example: Intercoolers and aftercoolers for compressors
- (2) Equipment installed at a height, requiring compactness and lightness  
 Example: Vaporizers and condensers used on towers such as distilling columns
- (3) Applications with severe operating conditions (e.g., high pressure, large temperature differences among fluids, operational fluctuations)  
 Example: Hydrogen coolers for high-pressure hydrogen stations

It should be noted that, from the aspect of economy, the ALEX is recommended for applications in which the design pressure is low enough (13MPa or lower) and there are no operational fluctuations.

## 2. Verification of heat transfer performance

### 2.1 Technique for performance calculation

The performance calculation of a DCHE employs the calculation technique used for the ALEX, which has already been proven in many applications. More specifically, regarding the fin shape of an ALEX as the flow passage shape of a DCHE, as shown in Fig. 5, enables us to apply the design techniques of ALEX. This conversion from the ALEX to DCHE is applicable also to the strength calculation for each member.

The detailed calculation of the pressure loss and heat transfer performance requires coefficients (dimensionless numbers). These coefficients are obtained by making small cores, each simulating a corresponding flow passage, and measuring their pressure loss and heat transfer performance. The results are reflected in the performance calculation.

### 2.2 Performance verification test

To verify the performance calculation technique

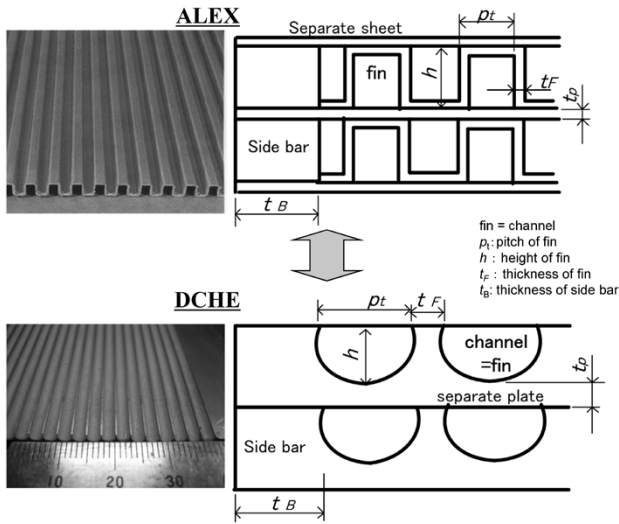
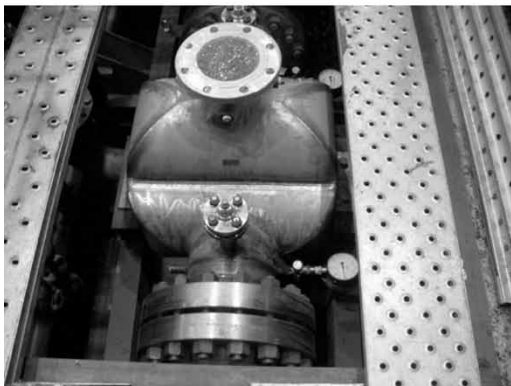


Fig. 5 Relationship of form between ALEX fin and DCHE channel



(a) Shell & Tube  
 $\Phi 650 \times 4,200$ TL-TL (5,500kg)



(b) DCHE  
 $330 \times 350 \times 650$  (700kg)

Fig. 6 Outside view of Shell & Tube and DCHE at same condition

and to confirm the performance, a DCHE was adapted to the aftercooler of a compressor. Fig. 6-top shows a multitubular heat exchanger, which has conventionally been used for the aftercooler of a compressor having a design pressure of 9MPaG. This multitubular heat exchanger is replaced by a DCHE (Fig. 6-bottom), designed for similar

conditions of heat transfer performance and pressure loss, to measure the DCHE's pressure loss and heat transfer performance.

Each of these heat exchangers was operated under various conditions to confirm its performance. The results have demonstrated that the DCHE performs with heat transfer and pressure loss as designed. This verifies that the design, based on the design technique for the ALEX, is applicable to the DCHE. Also, it has been demonstrated that a DCHE can be made significantly compact, approximately 1/10 in volume and 1/8 in weight, compared with the multitubular heat exchanger with the same heat transfer performance and pressure loss. It should be noted that greater effects than those of the conventional heat exchanger are achieved in compactness and weight reduction in cases where the operating pressure is higher and/or where a higher heat transfer performance is required.

### 3. Verification of mechanical strength of diffusion-bonded bonding parts

#### 3.1 Diffusion bonding

Diffusion bonding is a key step in producing a DCHE. Diffusion bonding is defined in JIS Z3001<sup>4)</sup> as "a method for joining comprising the steps of closely sticking base materials together and pressing these materials against each other at a temperature not exceeding their melting points, while suppressing their plastic deformation to a minimum, so as to cause the diffusion of atoms at the joining interface to complete the bonding." It is considered to fall into the category of solid phase joining, which includes various other pressure welding methods such as friction welding and cold pressure welding (ambient temperature pressure welding).<sup>5), 6)</sup> Fig. 7 shows an example of the results of cross-sectional observation on a diffusion-bonded product.

In a DCHE, several hundreds of plates are stacked, each having flow passages. The stacked plates must be homogeneously bonded together to achieve the heat transfer and pressure resistance required. Thus, verification by a bonding test becomes just as important as, for example, theoretical verification obtained by analysis.

#### 3.2 Compliance with regulations and standards

DCHEs handle high-pressure gas and liquefied gas in many cases. In those cases, they must comply with the "High Pressure Gas Safety Law" in Japan and the "Boiler and Pressure Vessel Code (BPVC)" of the American Society of Mechanical Engineers

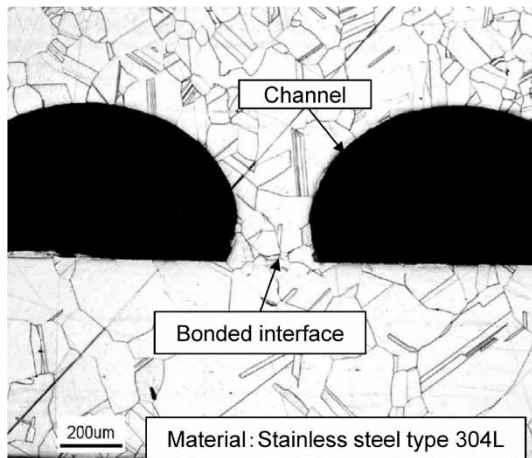


Fig. 7 Channel and cross-section observation of diffusion bonding

(ASME) outside Japan. **Fig. 8** shows an example of products that have passed testing according to the ASME standard. The soundness of each product is assured by its passing the non-destructive test, hydrostatic test and air tight test (leak test) required by the standards. Thus, advance verification of the diffusion bonding technique is indispensable. As in the case of the ALEX, the bondability is evaluated on the following points:

- ① Soundness evaluation for diffusion-bonded bonding parts (bondability attributable to materials)
- ② Strength evaluation for flow passage shape (bondability attributable to shapes)

The following sections describe the verification results for each item.

### 3.2.1 Soundness evaluation of diffusion-bonded parts

The details of the bonding method used in each product are determined and managed for the corresponding material by "diffusion bonding procedure qualification records (DPQRs)." When evaluating soundness, samples are prepared in accordance with each DPQR. The test pieces taken from these samples were evaluated for their mechanical properties. As a result, it has been confirmed that the bonding parts exhibit tensile strength, proof strength and elongation, all equaling or exceeding the standard value, regardless of the bonding location (the positions where the specimens were taken) and direction (vertical or parallel to the bonding interface).

### 3.2.2 Strength evaluation focusing on the flow passage shape

As described above, the bonding conditions are

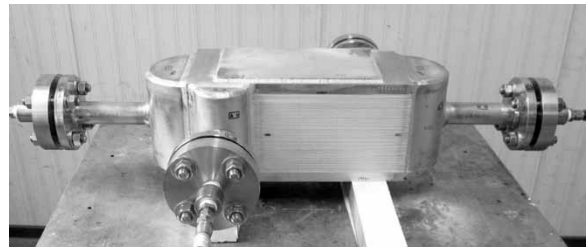


Fig. 8 DCHE with U-stamp of ASME

determined on the basis of the DPQR. In general, the shapes of flow passages determine the strength of an entire heat exchanger regardless of the material and bonding conditions. Therefore, the strength in relation to the flow passage shape is evaluated not only by calculation, but also by a burst test conducted on test samples. In a burst test, a diffusion-bonded test sample is pressurized by water, or by oil, and the pressure is measured when a part of the test sample starts to crack. The burst pressure is determined rather easily because the flow passage, unable to take any more pressure, expands, increasing its inner volume and causing the inner pressure to drop rapidly.

As an example of the burst test, a sample made of SUS316L stainless steel was tested. The result has confirmed that the test sample, with its flow passage shaped for high pressure, withstands a pressure of 450MPa or higher. Adopting a safety factor of 4 for this flow passage shape makes the design pressure 100MPa or higher. Different types of flow passages were subjected to bursting tests, which yielded bursting pressures that fall within plus/minus several percentages of variation, verifying the stability of the bonded parts.

## 4. Verification of fatigue strength

Applications for DCHEs include heat exchangers for high-pressure hydrogen stations. Conventionally, double-pipe heat exchangers have been used for this application because it calls for water cooling ultra-high-pressure hydrogen of approximately 80MPa. The problem with these conventional heat exchangers was that a great many number of joints are involved, and the equipment is large in size. In particular, a hydrogen station is expected to be annexed to an existing filling station and is required to be small.

The following are the specific applications of DCHEs for hydrogen stations:

- ① Intercoolers and aftercoolers of compressors (design pressure 95MPa, design temperature not exceeding 180°C)
- ② Precoolers for dispensers (design pressure 92MPa, design temperature -50°C to 50°C)

These applications require not only the static mechanical strength, but also the fatigue strength to withstand daily start-stop operation and the pressure fluctuations of the compressors. Therefore, an evaluation of strength was conducted by analysis under the following conditions (Test 1 and Test 2). A fatigue test was also performed using a test sample that simulated an actual heat exchanger in a high-pressure environment, as shown in **Table 1**. The results were used to verify the mechanical strength. Here, Test 1 assumes a cooler for the compressor in accordance with application ①, while Test 2 assumes a pre-cooler for the dispenser in accordance with application ②.

#### 4.1 Evaluation by stress analysis

**Fig. 9** depicts an analysis model for the flow passage shape of the present heat exchanger. **Fig.10** depicts the result of an analysis of the model in operation. Values required for fatigue strength

Table 1 Pressure fluctuation condition

	Test 1	Test 2
Test media	Water	Hydrogen
Temperature of test device	20°C	-40°C
Range of pressure fluctuation	86.5MPa	90MPa
Cycle of pressure fluctuation	100,000 cycle	70,000 cycle

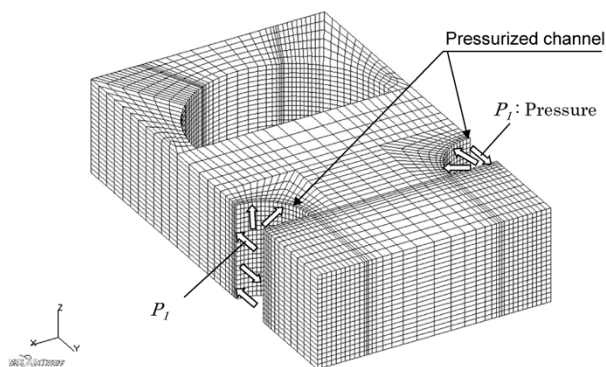


Fig. 9 Stress analysis model

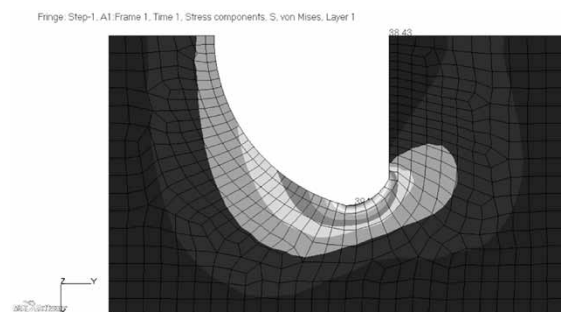


Fig.10 Stress analysis of production simulation model

evaluation, such as peak stress, mean stress, and stress amplitude of pressure fluctuations were calculated on the basis of the peak stress measured at a corner of each flow passage. The fatigue strength was evaluated on the basis of the design fatigue curve with the mean stress corrected for austenitic stainless steel. The results have confirmed that there is sufficient margin in the operating conditions and no problem in the use.

#### 4.2 Evaluation by fatigue test

Cycle tests under varying pressure, shown in Table 1, were conducted as shown in **Figs.11** and **12**. Neither test resulted in bursting of the test sample even after the planned number of cycles was exceeded. No leak of fluid (water or hydrogen) was detected, either. After the pressure cycle test, a tightness leak test using helium as the test fluid was performed to reconfirm that there was no leakage from any spot. These results verify the validity of the analysis and fatigue strength evaluation technique described above.

Furthermore, the diffusion-bonded parts were evaluated for hydrogen embrittlement. Specimens taken from the diffusion-bonded test samples were hydrogen charged and subsequently subjected to a tensile test at a low strain rate. The results confirm

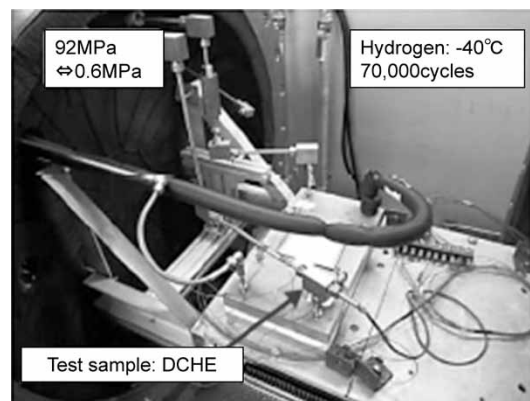


Fig.11 Cycle test of pressure fluctuation (Test 2)

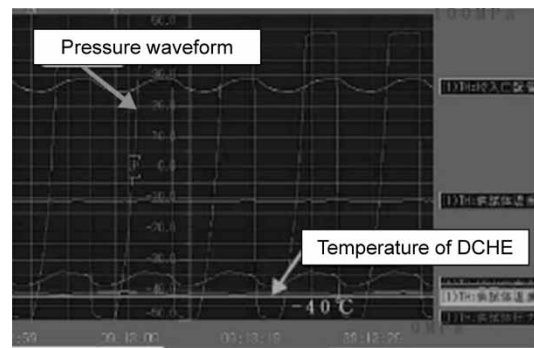


Fig.12 Cycle test of pressure fluctuation (Test 2)

that no effect of embrittlement is recognized in a high-pressure hydrogen environment.

From the above, the diffusion-bonded product has been confirmed to pose no problem in bonding quality and it has been found to withstand the pressure cycle test that accounts for the start-stop operation of a hydrogen station.

On the basis of these results, an aftercooler for a hydrogen compressor, shown in **Fig.13**, was fabricated in accordance with the designated equipment inspection regulations of the high pressure gas safety law. The equipment is very small, being only 1/30 to 1/100 the size of the conventional double-pipe heat exchanger. The DCHE is expected to be used in a variety of applications.

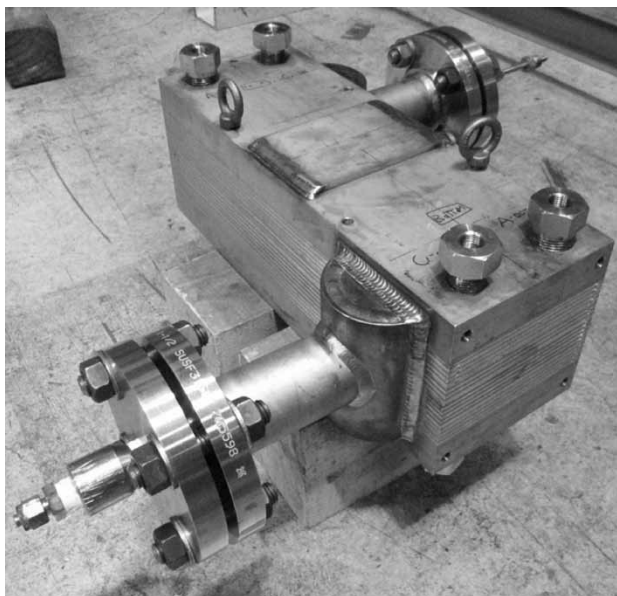


Fig.13 Outside view of DCHE for hydrogen station

## Conclusions

This paper introduces the diffusion-bonded compact heat exchanger (DCHE), a type of compact heat exchanger. The diffusion-bonding technique has been confirmed to pose no problem in bonding quality, which has been verified by mechanical testing and fatigue testing, as well as by computer analysis. The applications for DCHEs are expected to increase as they are used for hydrogen stations, a high-pressure application in which reliability counts most. Meanwhile, for offshore applications, DCHEs should be larger in capacity, and of high-performance, and their production technologies are being improved. We will continue to accumulate experience in producing DCHEs to further improve their reliability and will continue their development for further applications.

Lastly, we would like to express our gratitude to Tatsuno Corporation for conducting the experiment introduced in Table 1, Test 2.

## References

- 1) SCEJ Division of Chemical Reaction Engineering, Subdivision of Micro Chemical Process Engineering. *Lecture handout of micro chemical process sectional meeting 2010-1-15*, p.1-10.
- 2) K. Noishiki et al. *R&D Kobe Steel Engineering Report*. Vol.53, No.2, p.28-31.
- 3) K. Noishiki. *PETROTECH JAN 2012*. VOL. 35, NO. 1.
- 4) *JIS Z3001-1*, 2008, p.27.
- 5) T. Hashimoto et. al. *Current welding technical system No. 9 Solid-phase welding·Brazing*. Sanpo Publications Inc., 1980, p.95.
- 6) O. Ohashi. *Q&A Diffusion bonding*. Sanpo Publications Inc., 1993, p.31.

# Microchannel Reactor (Stacked Multi-Channel Reactor: SMCR<sup>®</sup>) for Bulk Chemical Industry

Dr. Koji NOISHIKI \*1, Yasutake MIWA \*1, Akira MATSUOKA \*2

\*1 Products Development Dept., Development Center, Machinery Business

\*2 Mechanical Engineering Research Laboratory, Technical Development Group

A microchannel reactor (MCR) has high thermal performance and rapid mass transfer thanks to its small channels where the reaction takes place. The microchannels offer a field that is more reactive than that offered by conventional mixer-type reactors. The application of MCRs, however, is limited to products such as medicines that have high value and are produced in small volumes. This is due to the limitation of the flow capacity of an MCR. Against this background, Kobe Steel has developed a stacked multi-channel reactor (SMCR<sup>®</sup>) that enables mass production and is applicable to the bulk chemical industry. This report explains the technology of the MCR, the features and the construction of the SMCR and the use of an SMCR for development work aimed at commercialization.

## Introduction

Microchannel reactors (MCRs) are receiving considerable attention. They have flow passages with small diameters, which enables them to achieve a heat transfer performance and mass transfer rate higher than those achieved by conventional reactors such as mixing tanks. These MCRs, however, have been applied only in the small-volume production of high-value-added products, such as pharmaceuticals that are manufactured in a wide variety. This is due, among other things, to the limitation in their throughput capacities.

Against this background, Kobe Steel has developed a stacked-type multi-channel reactor (hereinafter an SMCR<sup>®</sup>, note 1)) capable of high volume processing and has been promoting the applications of this new MCR technology to bulk chemicals.

This paper introduces the technologies of MCRs, the structure of the SMCR and its features. Also introduced is the flow of the development of the SMCR up to its commercial use.

## 1. What is an MCR?

### 1.1 Features of MCR

Many have reported that reducing the diameters of flow passages, as shown in Fig. 1, achieves a higher heat transfer performance and mass transfer

rate compared with conventional reactors such as mixing tanks.<sup>1), 2)</sup>

Fluid in a small flow passage is greatly affected by wall surfaces, but is relatively less affected by gravity. This makes the separation commonly observed in conventional equipment and piping—that is, a separation between heavy and light products, or between gas and liquid—less likely to occur. As a result, various flow patterns appear, as shown in Fig. 2, depending on the physical properties of the fluid and the flow velocity. In the case of two mutually insoluble liquids such as water and oil, for example, slug flow appears in the region where the flow velocity is relatively low, while two-layer flow appears in the region where the flow velocity is high. Fig. 3 shows a photograph of slug flow with its image diagram. When the wall

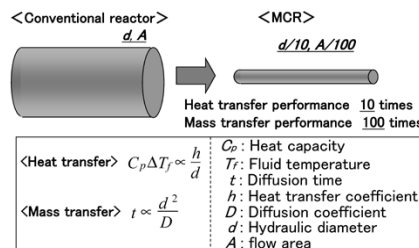


Fig. 1 Comparison between conventional reactor and microchannel reactor

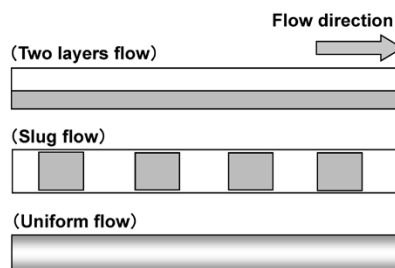


Fig. 2 Example of flow pattern in microchannel

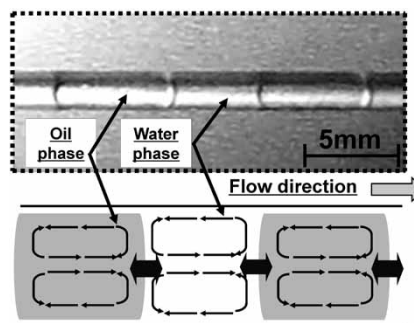


Fig. 3 Slug flow in microchannel

note 1) SMCR is a registered trademark of Kobe Steel.

surface is either stainless steel or glass, for example, its hydrophilic nature makes the water stagnate on the wall surface. Thus the oil flow is enveloped by the water. As a result, the slug flow sometimes creates a greater contact area at the interface of the fluids than does the two-layer flow. In addition, such wall surfaces also have been confirmed to cause an internal circulation flow.<sup>3), 4)</sup> Hence, a higher mass transfer performance can be achieved by selectively exploiting the slug flow, which is expected to further improve the performance of MCRs.

## 1.2 Problems with conventional MCR

An MCR is often called a "micro reactor" because of the established image of the equipment itself as being small in size, and not just because of the size of its flow passages. For this reason, the units are mostly used for small volume production, from several to several hundreds of kilograms per annum, of high-value-added products such as pharmaceuticals. They have hitherto not have been adopted by the general chemical industry, which processes large volumes amounting from several thousands to several tens of thousands of tonnes per annum.

The major reason is the high cost of making equipment, including the cost of fabricating the flow passages, which only permits the making of small units. There is also a methodological difficulty in fabricating a large number of flow passages in a unit (hereinafter referred to as "numbering-up"), making the unit unsuitable to high-capacity applications.

In short, the major issue is that, notwithstanding the reactor's potential for delivering a better performance than has ever been seen before, no means has been available for the industrial use of the MCR. It is against this background that Kobe Steel launched its development of an MCR unit capable of processing large volumes.

## 2. Structure of SMCR equipment

### 2.1 Basic technology of stacked heat exchanger

The basic technology of the SMCR lies in its brazed aluminum plate-fin heat exchangers (hereinafter called ALEX<sup>®</sup>, note 2)), a high-performance heat exchanger made of aluminum alloy having excellent heat transfer performance. It was developed as a heat exchanger for equipment that separates air into oxygen and nitrogen at very low-temperatures. Being capable of exchanging

heat among several fluids at a time, the ALEX has recently been widely used in plants as an apparatus for natural gas processing and in cryogenic section in ethylene plants.

As shown in Fig. 4, an ALEX comprises a brazed core for exchanging heat and a header/nozzle for guiding fluid into the core. It has a stacked structure, made capable of homogeneously distributing not only gas and liquid, but also two-phase flow (gas-liquid mixed phase), by arranging and combining fins in each layer. The apparatus can also exchange heat among several fluids simultaneously.

In some applications, an ALEX can have a heat transfer area per unit volume of 1,000m<sup>2</sup>/m<sup>3</sup> or greater, which exceeds that of conventional shell & tube type heat exchangers by a factor of 5 or more; so it can enable the downsizing of the equipment. The ALEX can be used as a single unit, in which multiple cores are welded together and attached to a common header and nozzle, or as multiple units connected by pipes. This enables the ALEX to handle any given flow rate and to process large volumes.

### 2.2 Technologies applicable to large capacity SMCRs

Being widely used as a heat exchanger, the ALEX offers the following basic technologies:

- (1) Production technology including joining and flow passage fabrication.
- (2) Heat transfer design used for performance calculation, and technology for pressure loss calculation.
- (3) Technologies for homogeneously distributing and mixing on the basis of the structure for gas-liquid distribution.
- (4) Technology for reducing maldistribution of

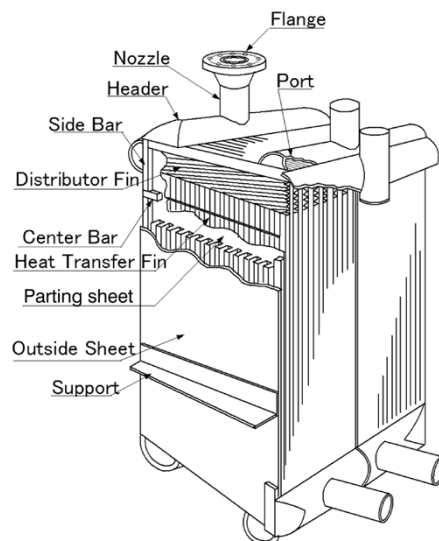


Fig. 4 Structure of ALEX

note 2) ALEX is a registered trademark of Kobe Steel.

the fluid between cores.

- (5) Technology for reducing maldistribution of the fluid between layers.

These are the design technologies and know-how obtained through experience with the ALEX, and they can be exploited for large capacity SMCRs.

### 2.3 Basic construction of SMCR

The flow passages in an MCR basically consists of the combination of multiple tubes, each having a Y shape or a T shape, as shown in Fig. 5 top. However, if used as-is for the numbering-up of capacity enlargement, this configuration is limited in the arrangement of flow passages due to difficulties in, for example, the supply method of fluids. Notwithstanding the ease of numbering-up in the stacking direction, it is difficult to arrange multiple fluid passages in an efficient manner in the width direction, rendering the structure unsuitable for large capacity MCRs. Therefore, a structure has been devised, on the basis of the existing structure of ALEX (Fig. 5 bottom), with the flow passages fabricated in a three-dimensional arrangement on both sides of each plate.

This structure allows for a dense arrangement of the flow passages within a plate, as shown in Fig. 6. This significantly increases the number of flow passages per unit volume, enabling high-

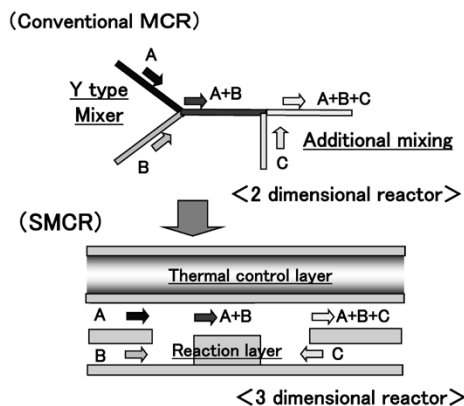


Fig. 5 Basic construction of two-dimensional reactor and three-dimensional reactor

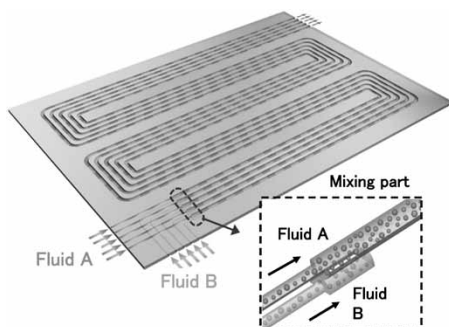


Fig. 6 Basic construction of multi-channel SMCR

volume processing. For increased processing volume, a plurality of plates can be stacked, as shown in Fig. 7, to further increase the number of flow passages. In other words, the number of flow passages per unit is given by the number of flow passages per plate multiplied by the number of the plates stacked.

When temperature control is required for operation, a thermal control layer can be stacked, as shown in Fig. 5, to permit precision temperature adjustment. For the supply of fluid into each flow passage, a header-nozzle assembly, as shown in Fig. 4 for the case of the ALEX, may be used for the homogeneous distribution of fluid into each plate (Fig. 7). A large capacity MCR, adopting the above construction, is referred to as an SMCR.

The process of making an SMCR is as follows: First, a flow passage pattern as shown in Fig. 8 is formed by, for example, chemical etching on metal plates, such as stainless steel plates. Next, these plates are stacked, in combination with thermal control layers, until the required number of flow passages is reached. This is followed by heating and pressing the stacked plates in a vacuum furnace to diffusion-bond them so as to form the flow passages. Fig. 9 shows an example of a diffusion-bonded section of stainless steel. No deformation of the flow passages was found, and the crystal grains were observed to have grown beyond the bonded interface, ensuring a bonding strength equal to or higher than the strength of the base material. Hence, the pressure-withstanding performance can be estimated by a strength calculation based solely on the size of the flow passages. In addition,

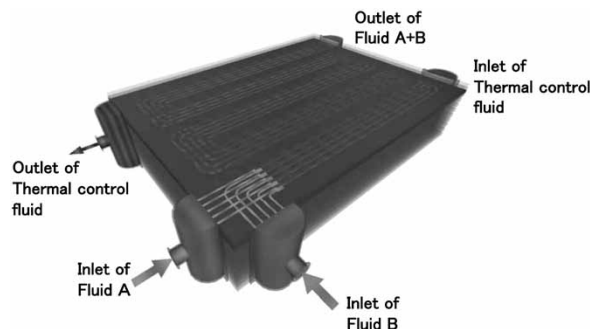


Fig. 7 Inside image of SMCR

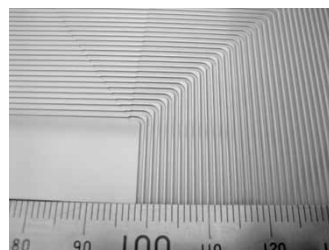


Fig. 8 Microchannel manufactured by chemical etching

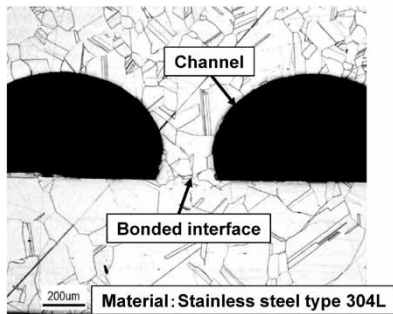


Fig. 9 Cross-sectional observation of channels and diffusion bonded interface

various materials can be used, depending on the specification requirements, such as high resistance to corrosion and being able to withstand high temperatures; this permits a high degree of freedom in design and production.

### 3. Flow of development up to commercial use

As in the case of conventional equipment, the development of an SMCR follows the flow shown in Fig.10. Here, the concept of numbering-up, a feature of the MCR, can be adapted to the SMCR so as to shorten the development period.

The following describes an example of laboratory testing. An extraction feed of dodecane containing 0.1wt% of phenol was prepared. This solution was subjected to the extraction of phenol using water as the extraction solvent. Various flow passage diameters and shapes (semicircular and circular) were used. As shown in Fig.11, the volumetric mass transfer coefficient,  $Ka$ , an indicator of the mass transfer rate, has been confirmed to correlate with the hydraulic equivalent diameter (= four times the cross-sectional area of the flow passages divided by the length of wetted perimeter).<sup>5)</sup>

This result verifies that laboratory test data obtained by universities and corporate research institutions can be adopted as-is for the SMCR, minimizing the overlap of testing and shortening its test and development period.

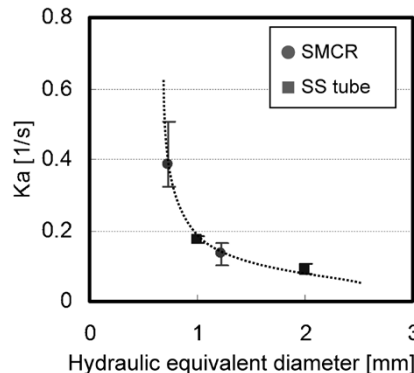


Fig.11 Relationship between  $Ka$  and hydraulic equivalent diameter

Bench tests are effective in predicting the performance of the commercially used equipment. These bench tests are conducted after determining the shape, plate size and the number of stacks required for commercially used equipment. Plates that have a size equivalent to that of the actual equipment, as shown in Fig. 6, are stacked in three layers, for example, or in any number of layers that allows confirmation of the effect of maldistribution. The issues involved in commercialization include the homogeneous distribution of fluid into each plate layer at the time of upsizing. In the case of ALEX, more than a hundred layers were stacked while distributing the fluid homogeneously into each flow passage. This proven design technology can be used to prevent any problems due to maldistribution in practice. Hence, the risk of performance decrement caused by scale-up, a problem for the reactors of mixing-tank type, can be significantly reduced. In the case of the SMCR, a verification test serving as both a bench test and demonstration plant is considered sufficient for making all the judgments needed for commercialization.

As described above, SMCRs are not only excellent in heat transfer performance and mass transfer rate, but they also make it possible to decrease the amount of investment and shorten the development period.

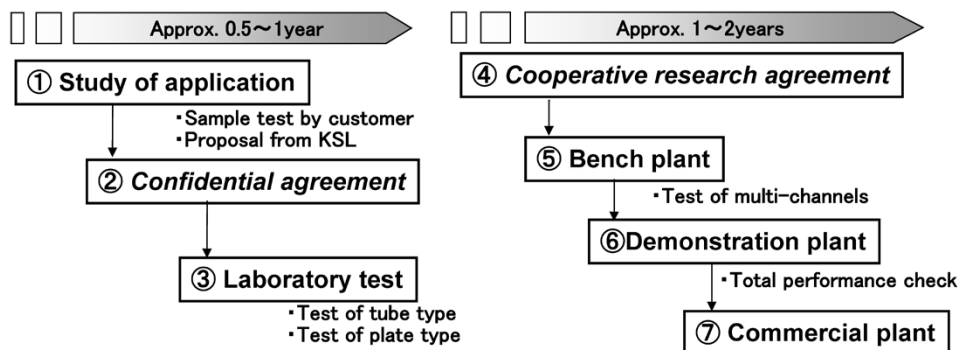


Fig.10 Flow of development work for commercialization

## 4. Examples of SMCR applications

### 4.1 Study for extraction applications

A process of making various chemical products involves an extraction step, using extraction solvent for removing objective substances (or, non-objective substances) in an objective fluid. When the extraction solvent is recycled, for example, a series of processes are performed, including extracting product from the objective fluid using extraction solvent in a mixing tank, separating the product from the extraction solvent using the difference in their specific gravities, and subsequently separating and recovering the subjective fluid and extraction solvent by a distillation operation or the like. In this case, the capacity of the solvent recovery apparatus is determined so as to match the capacity of the mixing tank used for the extraction.

When used for such extraction equipment, the SMCR is expected to provide the following effects:

- (1) decreased extraction time
- (2) decreased size of the extraction process equipment
- (3) reduced unit consumption, thanks to using a smaller amount of extraction solvent
- (4) capability of continuous processing when multi-stage extraction is required

The following describes an extraction test using an SMCR to confirm its applicability to the extraction process.

### 4.2 Experimental method and results

SMCR test units comprised a stainless steel plate having semicircular microchannels formed by etching, in which the stainless steel plate was sandwiched by other stainless steel plates. Three types of units having different number of flow passages were prepared: one having one flow passage (1 passage/layer  $\times$  1 layer), another having five flow passages (5 passages/layer  $\times$  1 layer), and yet another having 25 flow passages (5 passages/layer  $\times$  5 layers). These units were tested to confirm if there were any performance decrement due to maldistribution of fluid caused by the increased number of flow passages, or by the capacity upsizing. Extraction experiments were carried out using the bench test apparatus shown in Fig.12.

In this experiment, phenol was extracted from an extraction feed of dodecane containing 0.1wt% of phenol, using water as the extraction solvent.

The above feed and solvent, mixed at a volume ratio of 1, were pumped into each test unit at a given flow rate (total of 1 to 10ml/min per flow

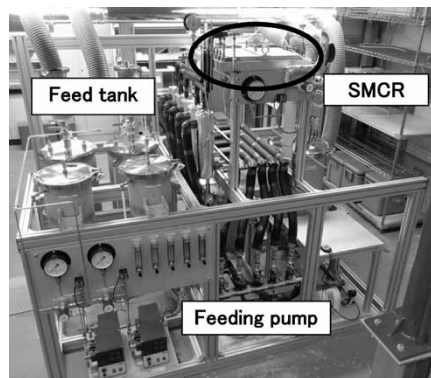


Fig.12 Bench test apparatus of SMCR for extraction use

passage). The recovered solution was separated into an organic phase and a water phase. The separated organic phase was subjected to absorption spectrophotometry to measure the phenol concentration in it and to determine the extraction rate of the phenol.

A mixer extraction test was conducted, in which the extraction feed and extraction solvent, 100ml of each, were poured into a 200ml beaker and the extraction solvent phase was stirred at a given rpm using a magnetic stirrer. The phenol concentration in the extraction feed was analyzed at a given time interval to determine the extraction rate. Fig.13 shows the experimental results. The vertical axis represents the equilibrium extraction ratio (= extraction rate (%) / equilibrium extraction rate (%)), and the horizontal axis represents the retention time.

In this mixer extraction test, increased revolution of the stirrer shortens the time required for extraction; however, revolutions higher than 400rpm resulted in a dispersion of the extraction feed in the extraction solvent, making separation difficult. It took approximately 100minutes for the mixer extraction to reach an equilibrium extraction, while SMCR achieved the same result within 0.1 to 1 minute, a shortening of approximately 1/100. The fluid from the SMCR test unit was separated into the two phases of extraction feed and extraction solvent as soon as the fluid was discharged. This is because

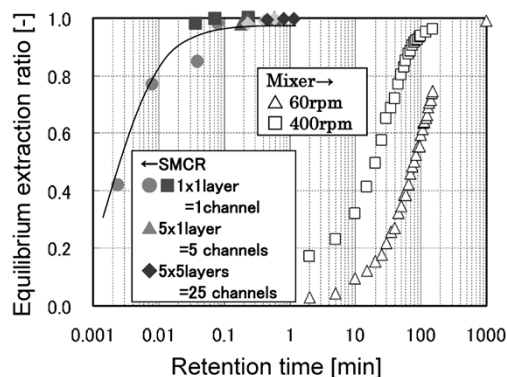


Fig.13 Test results for extraction use (SMCR vs. Mixer)

the mixing portions, shown in Fig. 5, do not vigorously mix but rather form a slug flow and/or a two-layer flow of oil and water so as to keep them separable. These experimental results confirm the following advantages of using the SMCR for extraction:

- (1) The retention time is shortened to 1/100 of that required for mixer extraction.
- (2) Excellent separability is achieved after the extraction.
- (3) Excellent distribution of the solution is achieved regardless of the numbers of flow passages and layers.

### 4.3 Study of the commercial use of SMCR

Many extraction applications require multiple steps of extraction until a desired extraction concentration is reached. In a conventional extraction unit, the mixing tank serves also as a separation tank as shown in Fig.14. In such a tank, multiple steps of extraction, each followed by a separation step, were performed in batches. In some extraction applications, the extraction operation itself lasts for only several minutes; however, the separation takes several hours, requiring much time and labor to achieve the target extraction rate.

On the other hand, when the SMCR is used for multistage extraction, more than one extraction unit can be stacked and integrated as shown in Fig.15. Furthermore, the excellent separability after extraction enables a continuous process: the raw material, rapidly separated by settlers, is continuously fed into the SMCR.

This eliminates the time-consuming separation and the switching operation of charging and discharging the solution, steps required by the conventional-type process, thus enabling the SMCR to perform efficient extraction. Hence, there are two options for the commercial use of the SMCR. One is to minimize the equipment size with a reduced process volume per unit time so as to complete the process within a time equivalent to that required

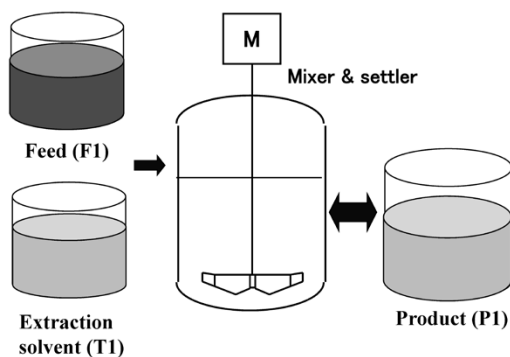


Fig.14 Conventional extraction unit using mixer

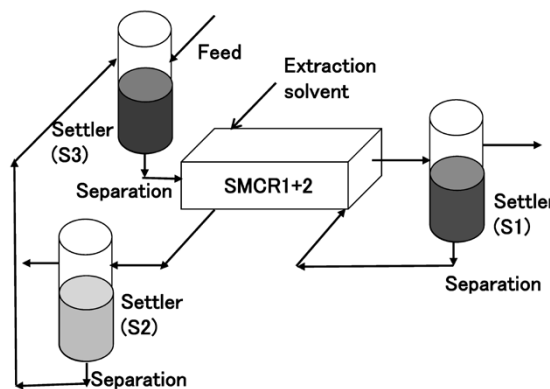


Fig.15 Multi-stage extraction unit using SMCR

for a conventional batch process. The other is to aim at a larger process capacity by processing at higher efficiency within a time shorter than that required by a batch process.

As future efforts to promote commercial use, testing will be continued for other extraction applications to accumulate data on their extraction performance and to compare their economy, including equipment and operational costs, with that of a conventional extraction unit.

### Conclusions

Features of MCRs such as their high heat transfer performance and mass transfer rate have led to their being considered for industrial use. In general, however, these units are small and costly, which limits their application to high-value-added products and to cases where a rapid reaction calls for almost no retention time and only small equipment is required. However, the SMCR described in this paper can have increased capacity while keeping the MCR's functions of high heat transfer and mass transfer. This makes these units applicable not only to high-value-added products, but also to bulk chemical industries involving, for example, extraction and other reactions requiring a relatively long retention time.

The SMCR has various features, including high heat transfer performance and high yield. Thus, its applications are not limited to the downsizing of equipment. Its advantage of continuous-processing capability is exploited to improve production efficiency, including the elimination of setup time that would otherwise be required if using conventional batch processes. Versatile effects, including the relaxing of process conditions (e.g., operating pressure and temperature), can be achieved. This can save energy and reduces the amount of the various chemicals used, including extraction solvent.

## References

- 1) J. Yoshida. *Development and Application of Microreactors*. CMC Publishing CO., LTD., 2003, p.4.
- 2) G. S. Calabrese. *AIChE J.* 2011, Vol. 57, No. 4, p.828.
- 3) A. Ghaini et al. *Chemical Engineering Science*. 2011, Vol.66, p.1168-1178.
- 4) H. Kinoshita et al. *Lab Chip*, 2007, Vol. 7, p.338-346.
- 5) A. Matsuoka et al. Extraction performance in small flow channel with semicircular cross section. *Proceeding of the SCEJ 44th Autumn Meeting 2012*, I305.

# LNG Vaporizer for LNG Re-gasification Terminal

Shinji EGASHIRA \*1

\*1 Takasago Equipment Plant, Energy & Nuclear Equipment Div., Machinery Business

*Kobe Steel leads the world in LNG vaporizers. We design and fabricate "open rack type vaporizers (ORVs)" and "intermediate fluid type LNG vaporizers (IFVs)" for large LNG receiving terminals. This paper introduces the trends in the present LNG receiving terminals, the features of LNG vaporizers and topics having to do with the company's development of vaporizers.*

## Introduction

Natural gas is a clean fuel and the demand for it is increasing worldwide. In consuming countries such as Japan, far from gas producing regions, natural gas is received as liquefied natural gas (LNG) in a cryogenic state (approximately -160°C), warmed up to normal temperature to be regasified, and is used as fuel for power generation and city gas.

As a leading manufacturer of LNG vaporizers, Kobe Steel has been actively developing its business in Japan and overseas. The recent trend is for the number of projects to increase in countries where the company has no delivery record and in areas where the environment and heat sources are different from the traditional ones.

LNG receiving terminals are classified into two categories: i.e., primary receiving terminals for receiving LNG imported in large LNG vessels, and secondary receiving terminals (satellite terminals) for receiving and regasifying LNG transported by trucks or the like from a primary receiving terminal. This paper outlines the latest trends in primary receiving terminals (hereinafter simply referred to as "receiving terminals") with a special focus on the LNG vaporizers used in these terminals.

## 1. Trends in LNG receiving terminals

### 1.1 Diversification of regions

In the past, LNG was imported by a limited number of advanced countries, including Japan, South Korea, Taiwan, and western European countries, such as France and Spain. Since the turn of the century, however, the countries receiving LNG have diversified as the demand has increased. The following describes the recent circumstances of LNG receiving regions.

- In the countries with high economic growth,

such as in India and Brazil, the number of projects for LNG receiving terminals is increasing. A large number of projects are underway or planned, particularly in China.

- In regions such as the Middle East and Central and South America, or in countries that hitherto have not imported LNG, the number of projects for LNG receiving terminals is increasing.
- New construction projects for LNG receiving terminals are underway or planned in countries, such as Indonesia and Malaysia, that used to be exporters of LNG.
- With the shale gas revolution, US terminals that used to receive LNG are being converted into liquefaction and exporting terminals.

### 1.2 Diversification in the types of LNG receiving terminals

Conventionally, LNG receiving terminals have been built along coasts and used seawater—or fuel in cold districts during cold seasons—as their heat sources for vaporizing and warming LNG to normal temperature gas. Recently, new types of LNG receiving terminals have emerged, and the number of projects they are involved in is gradually increasing. These new types include the following:

- ① Floating storage regasification units (hereinafter FSRUs), and
- ② LNG vaporizer systems with air heat sources

#### 1.2.1 Floating storage regasification units (FSRU)

FSRUs are LNG receiving terminals consisting of vessels that have been modified to accommodate equipment such as vaporizers; they are moored offshore. The following describes the features of FSRUs:

- The use of existing LNG vessels eliminates the need for civil engineering work and the construction of LNG tanks, which would be required for land terminals, enabling the shortening of the period of construction.
- FSRUs are mobile and can be used in other locations.
- In the event of a mishap, damage to the general public and neighbors can be avoided, thus making protest campaigns against the construction unlikely.



Fig. 1 Image of FSRU in operation<sup>1)</sup>

- Measures must be taken against the pitching and rolling of the hull.

FSRUs have already been put into service in Brazil, for example. Fig. 1<sup>1)</sup> shows an image of the outside of an FSRU. The vessel on the left is an LNG carrier, and the one on the right is an FSRU. The equipment on the top shelf of the FSRU's bow structure includes an intermediate fluid type vaporizer (hereinafter, an IFV).

### 1.2.2 LNG vaporizer systems with air heat-source

Seawater is generally used as a heat source for vaporizing and warming LNG in primary receiving terminals, except for those built in cold areas. Using seawater requires significant investment in facilities for the intake and discharge of water. In addition, environmental regulations must be followed for the cold seawater discharged after the heat exchange with LNG.

To avoid these issues, a non-seawater vaporizer system was devised in which LNG is vaporized by the sensible heat of aqueous glycol solution. The cooled glycol solution is warmed by the heat of air blown by a fan and is reused for vaporizing LNG. This system is currently operating at the DAHEJ terminal in India, while others are being constructed or planned at other terminals in this country.

This vaporizer system is basically designed to be operated at an atmospheric temperature of 15°C or higher and is applicable only to areas where the ambient temperature is high enough.

## 2. Structure and features of LNG vaporizers for primary receiving terminals

### 2.1 Outline

Currently, over thirty LNG receiving terminals are operating in Japan, and there are many others overseas. This section describes the structures and

features of the vaporizers generally used in these terminals: namely, open rack vaporizers (ORVs), intermediate fluid type vaporizers (IFVs) and submerged combustion vaporizers (SCVs).

### 2.2 Open rack vaporizers (ORV)

#### 2.2.1 Overall structure of ORVs and the vaporizing process

Fig. 2 schematically outlines an ORV. An ORV is a vaporizer in which LNG, flowing inside a heat-transfer tube, exchanges heat with seawater that flows outside the heat-transfer tube to gasify the LNG. The LNG flows in from an inlet nozzle near the bottom and passes through an inlet manifold and a header pipe to be sent to a set of panels, each consisting of a curtain-like array of heat-transfer tubes. As LNG flows upward inside the heat-transfer tubes, it exchanges heat with seawater that flows downward in a film-like manner outside the heat-transfer tubes. This produces normal temperature gas to be sent out from an outlet nozzle via an outlet header and manifold pipe.

Each panel generally consists of close to a hundred heat-transfer tubes. Several of these panels (3 to 8) are unified into a block by a manifold pipe and are hung from a ceiling frame placed over a concrete structure at the installation site. A slide-type support is provided under the block so as to absorb thermal expansion/contraction. The surfaces of these panels, each consisting of aluminum alloy, are spray-coated with aluminum-zinc alloy that serves as a sacrificial anode to protect the base material from being corroded by seawater.

The heat-transfer tubes for ORVs are made of aluminum alloy having excellent low-temperature characteristics, such as low-temperature toughness, as well as excellent thermal conductivity and workability, and are provided with fins to increase

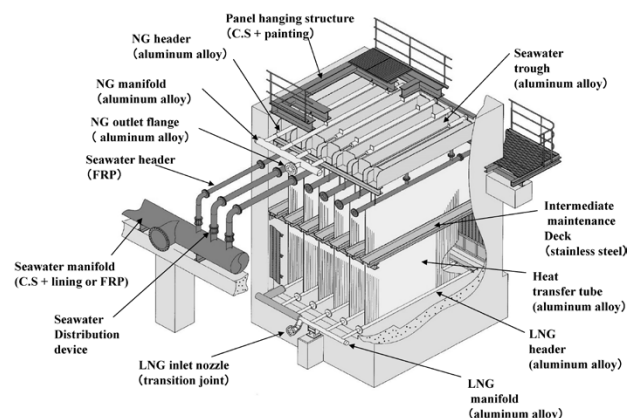


Fig. 2 Schematic of Open Rack Vaporizer (ORV)

the heat transfer area. Inside each heat-transfer tube, there is a cruciate profile of aluminum alloy, spirally twisted and fixed through the entire length. This structure promotes turbulent flow, which improves the heat transfer performance while preventing LNG mist from spilling to the outlet.

### 2.2.2 Heat transfer tube with dual structure: SUPERORV<sup>®</sup> note)

When an ORV is in operation, the outer wall temperature at the lower part of each heat-transfer tube sinks lower than the freezing point of seawater, causing icing to build-up on the tubes. Especially, when the seawater temperature is low, icing thickness and height increases significantly, which causes a significant heat-transfer resistance. As a measure, Kobe Steel has developed a new heat-transfer tube (SUPERORV) that has a duplex-pipe structure at its lower part to suppress icing on the outer surface of the heat-transfer tube. This has significantly improved the vaporizing performance. SUPERORVs are now in actual use in heat exchangers. Fig. 3 shows the structure of the SUPERORV heat-transfer tube.

### 2.2.3 ORV features

ORVs have the following features and are most generally used for primary receiving terminals.

- ① The use of seawater as a heat source achieves low running costs (in most cases incurring only the cost of powering the pumps).
- ② The system is simple and has excellent operability, allowing visual observations from the outside of the heat-transfer tubes during its operation, which ensures very high reliability.
- ③ Increasing or decreasing the number of panels

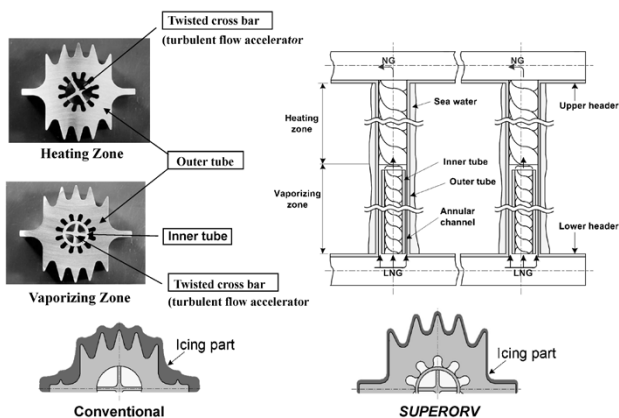


Fig. 3 Configuration of SUPERORV heat transfer tube

note) SUPERORV is a registered trademark of Kobe Steel.

or blocks easily allows a design appropriate for the vaporizing capacity, enabling the designing of vaporizers with large capacities, exceeding 300 tonnes/h, for example.

## 2.3 Fluid type vaporizers (IFV)

### 2.3.1 Structure of IFV and its vaporizing process

An IFV is a vaporizer in which a heat source, such as seawater, is used to vaporize LNG via a heating medium such as propane. It was originally developed by OSAKA GAS Co., Ltd. in the 1970s under the name of TRI-EX. An IFV has a structure combining three types of shell-and-tube heat exchangers, i.e., an intermediate fluid vaporizer (E1), LNG vaporizer (E2) and NG trim heater (E3).

Fig. 4 schematically shows an IFV. LNG is first introduced into the heat-transfer tube of the E2. Next, the LNG exchanges heat with intermediate fluid gas above the E1 shell and is almost entirely vaporized and then transferred to the shell side of the E3 via an interconnecting line. Here, the LNG exchanges heat with seawater that flows inside of heat-transfer tube and is warmed up to be delivered as gas at a normal temperature. On the other hand, as a result of the heat exchange with LNG, the intermediate fluid is condensed on the outer surface of the heat-transfer tube of the E2, drops down into the E1 shell and exchanges heat with the seawater flowing inside yet other heat-transfer tubes, and is vaporized again as the intermediate fluid gas for vaporizing the LNG flowing inside the E2 tube. Propane is used as the intermediate fluid in most cases.

Those tubes in which seawater flows (i.e., the heat-transfer tubes of E1 and E3) are made of titanium alloy to ensure very high corrosion resistance against seawater.

### 2.3.2 Features of IFVs

The following describes the features of IFVs:

- ① As in the case of ORVs, the use of seawater as the major heat source achieves a low running

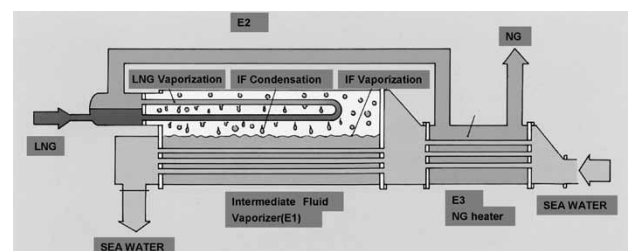


Fig. 4 Schematic of Intermediate Fluid type Vaporizer (IFV)

cost.

- ② Heat is exchanged between LNG and a heat source fluid via an intermediate medium, which avoids the freezing of the heat source fluid and its consequences such as the blockage of flow passages.
- ③ The use of titanium alloy for the material of heat-transfer tubes avoids problems, including erosion and corrosion, even when low quality seawater is used as the heat source.
- ④ The intermediate fluid and the chilled heat-source fluid after the heat exchange can be utilized as cold heat-sources.

Above feature ③ is embodied, for example, in the IFV that Kobe Steel delivered to the Shanghai LNG terminal in China, at which location the seawater contains 10,000 ppm of suspended solids (125 times the value of 80ppm recommended for ORVs). Since startup in 2009, the operation has been steadily continuing. Similarly, an IFV was adopted by the Ningbo LNG terminal in China and has been running since November 2012 at a location where the seawater contains a large amount of suspended solids.

## 2.4 Submerged combustion vaporizers (SCV)

### 2.4.1 Outline structure of the SCV and its vaporizing process

An SCV has a structure in which an underwater burner, burning fuel-gas, generates heat to vaporize LNG. It comprises a tank, an underwater burner, a bundle of heat-transfer tubes, combustion-air fan and fuel-supply control device (Fig. 5).

Both the bundle of heat-transfer tubes, which are a heat exchanging portion, and the underwater burner, a heat source, are submerged in the

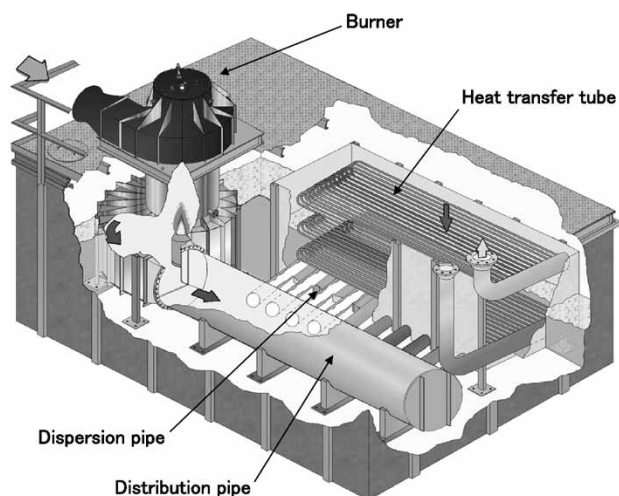


Fig. 5 Schematic of Submerged Combustion Vaporizer (SCV)

water inside the bath. This water is heated by the underwater burner. Because high-temperature combustion gas is exhausted into the water, the latent heat of steam contained in the combustion gas is effectively utilized. Inside the bath, the exhausted gas also forms a two-layer flow of mixed bubbles containing micro-bubbles, acting on the heat-transfer tube bundle to promote a more efficient heat exchange. The underwater burner and combustion-gas distribution mechanism, as well as an exhaust stack, are all provided inside the bath.

### 2.4.2 Features of SCV

The following describes the features of SCV:

- ① The use of combustion gas as a heat source allows the vaporizer to be smaller than other types of vaporizers of the same capacity.
- ② Even when the fuel gas is suddenly stopped, the supply of vaporizer gas continues, although for a limited time, thanks to the heat capacity of the heated water in the bath.
- ③ Unlike ORVs and IFVs, an SCV does not require any facility for water intake and discharge, which reduces the construction cost.
- ④ The running cost is very high because approximately 1.5% of the vaporized LNG is consumed as fuel.
- ⑤ Regulations on the combustion exhaust gas must be complied with.

## 3. Initiative for diversification in the types of LNG receiving terminals

As described in section 1.2, the types of LNG receiving terminals have been diversified in recent years. This section describes Kobe Steel's initiative for diversifying terminal types.

### 3.1 Initiative for FSRU

#### 3.1.1 Kobe Steel's history of LNG vaporizers for FSRU

As described in 1. 2. 1, the hulls of FSRUs pitch and roll, which must be taken into consideration for LNG vaporizers. In 1999, Kobe Steel studied an LNG vaporizer for a receiving terminal on board a vessel, in response to a request from the then Mobil Corporation (currently ExxonMobil Corporation). The study revealed that an IFV is the best fit, as long as a measure is taken against the sloshing (a waving phenomenon caused by moving liquid surface) of the intermediate medium propane. On the basis of this result, Kobe Steel applied for a patent on an

IFV comprising a measure against sloshing, and the patent was granted.

Although this project planned by Mobil Corporation was not realized in the end, Kobe Steel later received an order for three IFVs, each having a vaporizing capacity of 150tonnes/h, from SAIPEM S.P.A. in Italy. The purchase order was placed for LNG vaporizers used in an FSRU to be operated offshore of Livorno, Toscana, Italy by Offshore LNG Toscana (OLT). Notwithstanding the delay of the OLT FSRU project due to the client's circumstances after the delivery of the IFVs, they are slated to be put into service in the summer of 2013 after trial operations.

This project is subject to Italian ship classification (RINA), which involves a certification process and onsite inspections by RINA including manufacturer certification and process certification of the materials used for each pressure containment part of the IFVs, welding factory certification and welding method/welder certification, all of which have been implemented. A strength evaluation analysis was required, mainly for saddles and equipment joints, using the data of hull pitching and rolling that assumes a one-hundred-year storm. Also required was a sloshing analysis of the intermediate medium propane, and a certification procedure in writing, including assessments of various risk factors.

Fig. 6 shows the OLT FSRU under construction.

### 3.1.2 Future issues for LNG vaporizers used in FSRUs

Since an FSRU is built by modifying an LNG vessel, installation space is limited. Thus its LNG vaporizer must have a small footprint and low weight. Recently, circumstances have called for not only the supply of vaporizers alone, but also the package supplying of LNG vaporizer equipment, including peripheral piping, electrical apparatus, instrumentation and pumps.

In response to such requirements, Kobe Steel is



Fig. 6 Outside view of OLT FSRU (under construction)

moving forward with the downsizing of IFV with improved performance and the modularization of LNG vaporizer equipment.

## 3.2 Initiative for LNG vaporizer systems with air heat-sources

### 3.2.1 Development of IFV with air heat-source (Air-IFV)

As described in 1. 2. 2, an LNG vaporizer for a primary receiving terminal has been put into service at the DAHEJ terminal in India. The vaporizer uses air instead of seawater for its heat source. This system uses aqueous glycol solution, which is once cooled by exchanging heat with LNG and warmed up by air blown by fans to be reused for heat exchange with LNG. More than a hundred air blowers are required for the total 600tonnes/h of LNG vaporizing capacity.

On the basis of existing IFV technology, Kobe Steel has devised a new IFV with air heat-source (hereinafter "Air-IFV"), which employs air instead of seawater for its heat source and propane as its intermediate fluid to exchange heat with LNG. The newly developed system is more advantageous in the following points, compared with the aforementioned system that uses aqueous glycol solution as the intermediate medium.

- ①The new system exploits the latent heat of the vaporization and condensation of propane, and requires a smaller circulating volume than that required by conventional systems utilizing the sensible heat of a liquid such as aqueous glycol solution. This enables the reduction of the electric power cost of running circulating pumps.
- ②When propane is warmed up, a high boiling heat-transfer coefficient is obtained on the vaporizing side of propane, which reduces the amount of air compared with that required when aqueous glycol solution is used for warming. As a result, the number of fans and their power cost are reduced.

Fig. 7 depicts a schematic process flow of an

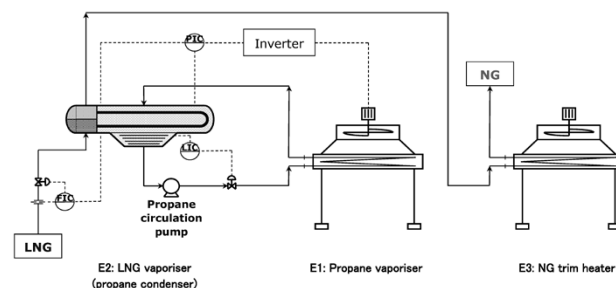


Fig. 7 Schematic process of Air-IFV

Air-IFV. The volume of air is inverter controlled, in response to the circulation volume of propane and atmospheric temperature, such that the pressure of propane in the LNG vaporizer (E2; propane condenser) is kept constant, which serves to reduce the power cost.

### **3.2.2 Future development of Air-IFVs**

Currently, studies are being conducted with the aim of putting Air-IFVs into service. Priority is being given to the verification of the evaporation characteristics of propane when an air heat-source is used, in order to establish the technique for designing a propane evaporator usable at a practical level. We will strive to design the details, including the control method, to provide LNG vaporizing equipment for launching in the market.

## **Conclusions**

This paper outlines the latest trends of LNG primary receiving terminals, the features of LNG vaporizers for these primary receiving terminals and Kobe Steel's efforts to develop LNG vaporizers.

Kobe Steel, as the world's leading manufacturer of LNG vaporizers, will continue brushing up its own technologies for ORVs and IFVs and will strive to develop and propose LNG vaporizer systems optimized for diversifying the types of LNG receiving terminals.

## **References**

- 1) A. Favi. OLT Livorno FSRU: an innovative solution for the gas industry. Convegni Tematici ATI-2012 Sesto San Giovanni (MI).

# Air-sourced 90°C Hot Water Supplying Heat Pump "HEM-90A"

Takahiro OUE\*1, Kazuto OKADA\*1

\*1 Refrigeration System & Energy Dept., Compressor Div., Machinery Business

Kobe Steel has developed an air-sourced heat pump, "HEM-90A," for supplying hot water. This heat pump is capable of supplying hot water at 65-90°C to the heating process of factories making products such as foods, beverages, automobiles and chemicals. The newly developed heat pump has achieved the highest energy efficiency among air-sourced heat pumps for supplying hot water by circulation heating. This was made possible by using a two-stage twin-screw compressor modified for high temperature operation by selecting an adequate refrigerant and optimizing an air-sourced evaporator unit. This paper introduces the features and the performance of our newly developed heat pump.

## Introduction

In plants making products such as beverages, foods and automobiles, high-temperature water is needed for various processes including the rinsing/sterilizing of raw materials and painting. Conventional heat sources for such hot water include combustion-type gas boilers and heaters. Recently, heat pumps are highly evaluated for their energy-saving features, and an increasing number of them are being used as alternative heat sources.

In 2009, Kobe Steel commercialized a series of heat pumps (HAI-EFU-MINI series). This includes the HEM<sup>note 1)</sup>-II HR, a heat pump that can simultaneously supply hot water up to 70°C and cold water. In 2010, the company commercialized the HEM-HR90, which can simultaneously supply hot water up to 90°C and cold water; this is an industry first.<sup>1), 2)</sup> These heat-source machines are being used in various production processes. Their simultaneous supplying of cold and hot water can efficiently utilize energy. Their merits are especially appreciated when both cold and hot energies are utilized for their base loads. In applications with a relatively small heat demand, however, the load balance between the cold and hot energies must be controlled. For this reason, some users have declined the introduction of these heat pumps.

In order to further disseminate heat pumps, Kobe Steel developed an air-sourced heat pump that supplies hot water without a cold-water load, the HEM-90A; it went on the market in May 2012. This paper introduces the system construction of the

newly developed heat pump, as well as its features and performance.<sup>3), 4)</sup>

## 1. Features of HEM-90A

### 1.1 Outline

Fig. 1 depicts the flow diagram of the HEM-90A. The conventional heat pump, the HEM-HR90, which takes out cold heat and hot heat simultaneously, comprises a vaporizer for taking heat from cold water as the latent heat of the vaporization of refrigerant fluid, a screw compressor for pressurizing the refrigerant gas that is vaporized, and a condenser for providing the latent heat of condensation of the refrigerant gas to heat water. This heat pump has a very high coefficient of performance (COP),<sup>note 2)</sup> thanks to the simultaneous use of cold and hot energies; however, the ratio between the amounts of cold and hot energies taken out is determined uniquely by the temperatures of the cold water and hot water. Thus, the load balance between the cold and hot energies must be controlled in some customers' applications.

To minimize the restrictions on customers when they use Kobe Steel's heat-source machines, the newly developed HEM-90A adapts an air heat exchanger for its vaporizer so as to eliminate the load of cold water and to take out heat from the air as the latent heat of vaporization of the

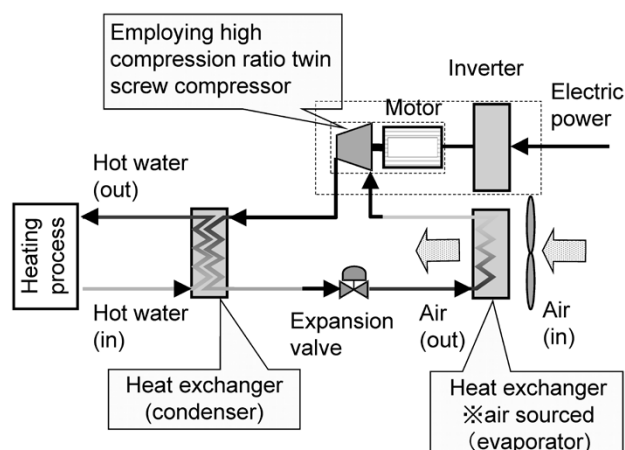


Fig. 1 Flow diagram of HEM-90A

note 1) HEM is a registered trademark in Japan of Kobe Steel.

note 2) Coefficient of performance (COP): the ratio of the heat put out over the electrical energy put in, i.e., an index of energy efficiency

refrigerant. This has enabled the sole supply of high-temperature water by a heat-pump cycle.

The outline specification, the performance and refrigerating cycle of HEM-90A are shown in Table 1, Table 2 and Fig. 2, respectively.

## 1.2 Advantage

The newly developed HEM-90A exploits the technology of the HEM-HR90. The new model adopts a two-stage screw compressor that can keep

Table 1 Specifications

Dimension (m)	L 2.84×W 1.54×H 2.70
Weight (kg)	2,990
Refrigerant	Mixture of HFC-134a and HFC-245fa
Hot water temperature at outlet (°C)	65~90
Ambient temperature (°C)	-10~40
Compressor	semi-hermetic two-stage twin-screw

Table 2 Performance (ambient temperature : 25°C)

Performance (condition ①)	55/65
Hot water temp. (°C)	
Heating capacity (kW)	159.1
Power input (kW)	45.2
Heating COP	3.5
Performance (condition ②)	80/90
Hot water temp. (°C)	
Heating capacity (kW)	176.2
Power input (kW)	62.9
Heating COP	2.8

high efficiency even under the discharge condition of high-temperature water up to 90°C. This is combined, for example, with the optimal design of an air heat exchanger, as well as with the optimal selection of refrigerant to enable operation with high energy efficiency. As a result, the new model has achieved a heating COP of 3.4 (conditions: ambient temperature 25°C, hot water 60/70°C), the highest efficiency that has yet been achieved by a circulation-type hot-water heat pump with an air heat-source. The term "heating COP" as herein used means the ratio of the quantity of heating heat over the power supplied to a heat-pump unit.

The newly developed heat pump requires less piping than water heat-source types. Also, it is designed to be compact (foot print: approximately 4.4m<sup>2</sup>), notwithstanding its being an air-source type. Thus, this heat pump can be installed in the proximity of a process requiring hot water, which significantly reduces the heat transfer loss that has conventionally occurred when steam or hot water is supplied from centralized heat sources. (A more detailed description will be found in section 4.)

## 2. Technology for improving efficiency

### 2.1 Compact two-stage screw compressor with high compression ratio

Fig. 3 outlines the compact two-stage screw compressor used for the HEM-90A, as well as a single-stage compressor. The compact two-stage compressor was modified from the one that had been developed for general HVAC and refrigeration, such that it can be used for the supply of high-temperature water. Here, a cooling method was

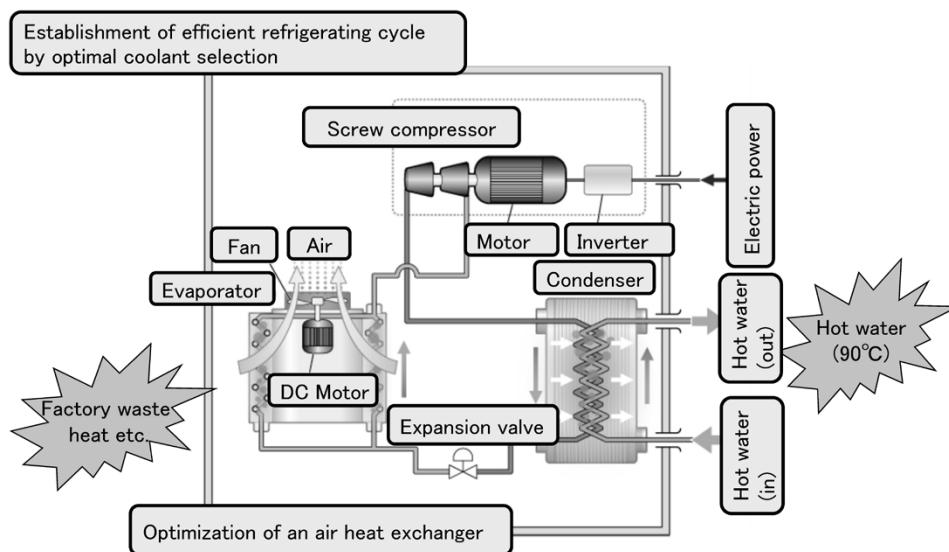


Fig. 2 Refrigerating cycle of HEM-90A

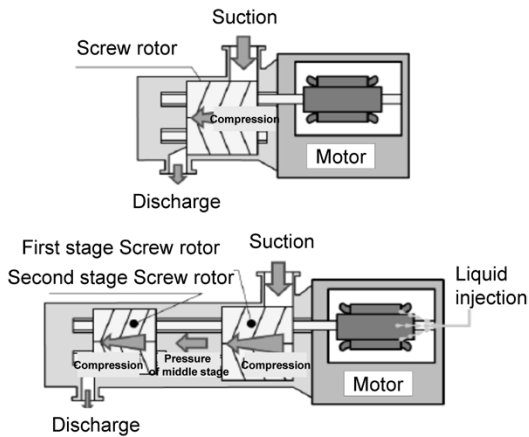


Fig. 3 Schematic view of compressor

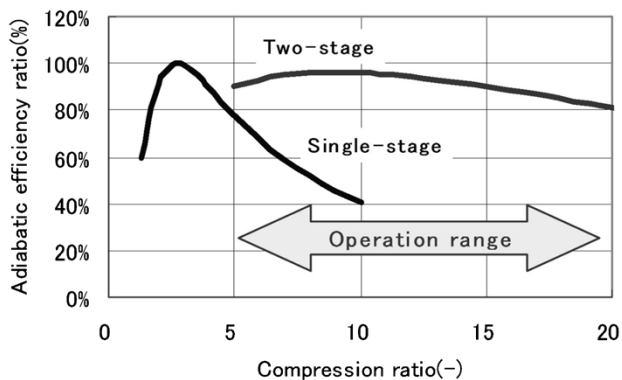


Fig. 4 Adiabatic efficiency ratio of compressor

devised, in which flashed refrigerant was sprayed directly onto the motor so as to retain the motor cooling performance even under high temperature conditions.

Fig. 4 shows the relationship between compressor efficiency (adiabatic efficiency) and the compression ratio. The term "compression ratio," as herein used, means the ratio of the discharge pressure to the suction pressure of a compressor. A heat pump requires a larger compression ratio as the temperature difference between the ambient air and hot water increases. As shown in this figure, the HEM-90A is operated in the range of a high compression ratio. In this operational range, a single-stage screw compressor sometimes exhibits significantly decreased efficiency depending on the ambient temperature and/or hot water temperature. Thus, the HEM-90A has adapted a two-stage screw compressor that can keep high efficiency over a wide compression ratio range and has realized high system performance.

## 2.2 Optimization of air heat exchanger

The air heat exchanger (vaporizer) adopts a plate-fin-tube type heat exchanger. If maldistribution of flow occurs during the partitioning of refrigerant

into each heat-transfer tube of an air heat-exchanger, the refrigerant dries out in the vicinity of the outlet of the heat-transfer tube that receives a smaller supply of the refrigerant. Also, if the flow of air becomes nonuniform as it passes a plate fin, the heat-transfer surface does not work effectively. These phenomena can cause the decrement of heat-transfer performance.

Also the refrigerant used this time is a mixture of fluorocarbons, HFC-134a and HFC-245fa. This makes the refrigerant non-azeotropic, in which case, its evaporating temperature varies depending on the quality of the refrigerant (mass flow ratio of refrigerant gas to refrigerant liquid at a given cross-section). The mixed refrigerant has a higher viscosity and lower thermal conductivity compared with single HFC-134a. As a result, the evaporative heat transfer for a given mass velocity condition may become relatively low.

In consideration of the above concerns about the design of an air heat exchanger, we adopted an inner grooved tube for the heat-transfer tubes and a louver type for the plate fins. The specification of the fan was selected while taking into account the partitioning mechanism of the refrigerant, the arrangement of heat-transfer tubes and the footprint of the unit. The layout, including the air heat exchanger, was also optimized. The new fan specification and layout have realized excellent heat-transfer performance with minimized power for the fan.

## 2.3 Optimum selection of refrigerant

When the refrigerant HFC-134a is used for supplying hot water at 90°C, its temperature becomes almost equal to the critical temperature (101.1°C) at which the refrigerant undergoes a phase transition from gas to liquid, making it difficult to establish a refrigerating cycle with high efficiency. Hence, the HEM-90A has adapted a mixed refrigerant consisting of HFC-245fa and HFC-134a. The HFC-245fa has been proven in HEM-HR90, has a critical temperature (157.5°C) higher than that of HFC-134a and is readily available.

The use of this mixed refrigerant has established a single refrigeration cycle, eliminating the needs for multiple compressors and heat exchangers for transferring heat between the low order-side and high order-side, the compressors and heat exchangers required for a binary refrigeration cycle.

## 3. Performance characteristics

Figs. 5 and 6 show, respectively, the characteristics

of the heating capacity and heating COP against ambient temperatures. Under typical operating conditions including an ambient temperature of 25°C and hot water outlet temperature of 70°C (hot water inlet temperature at 60°C), a heating capacity of 163.8kW and heating COP of 3.4 have been achieved.

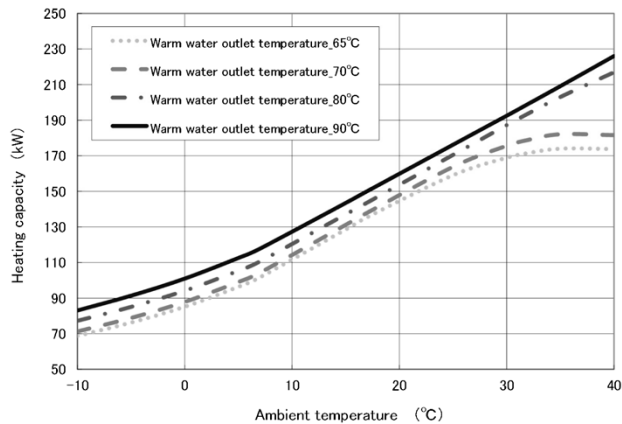


Fig. 5 Relationship between ambient temperature and heating capacity

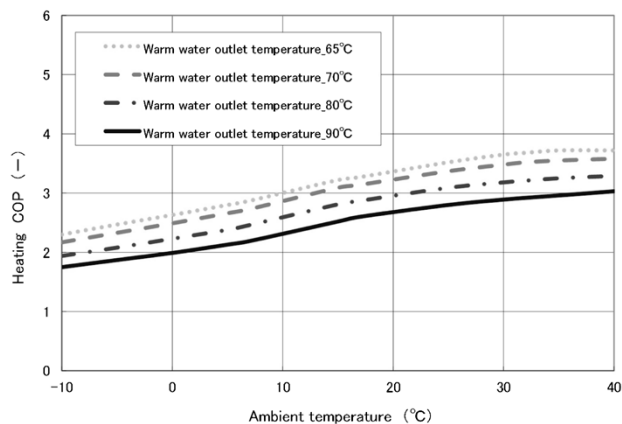


Fig. 6 Relationship between ambient temperature and heating COP

A heating capacity of 176.2kW and heating COP of 2.8 have been demonstrated even for the maximum hot water outlet temperature of 90°C (hot water inlet temperature 80°C).

For the first time for air-sourced heat pumps, the newly developed heat pump has enabled taking hot water out at a temperature as high as 90°C with high energy efficiency.

#### 4. Effects of introduction

A significant amount of heat is exhausted from plants producing, for example, beverages, food and automobiles. In conventional processes, heat loss from steam supply pipes, as well as pressure loss at reducer valves, occurs when steam is supplied from a gas boiler to each process segment, as shown in Fig. 7. In addition, the drain is exhausted without being fully utilized after processing in many cases. Thus, in some cases, the total loss in an entire system is reported to reach as high as approximately 70%.<sup>5)</sup>

An HEM-90A, installed in the proximity of the process requiring steam, can have the advantages of reducing the heat loss caused by the steam pipes and utilizing the heat that is unused and exhausted from the production process. In other words, the heat exhausted to the atmosphere in a plant can be partially recovered to be reused for generating high-temperature water by a heat-pump cycle.

The following describes a quantitative evaluation of the merit of doing this. Assuming a case where the outlet temperature of the hot water is 70°C (inlet temperature: 60°C), the application is an industrial operation running 8,000h per annum, and an existing boiler has a system efficiency of 50%, then the HEM-90A is expected to achieve significant cost reductions, a 58% reduction of running cost (Fig. 8)

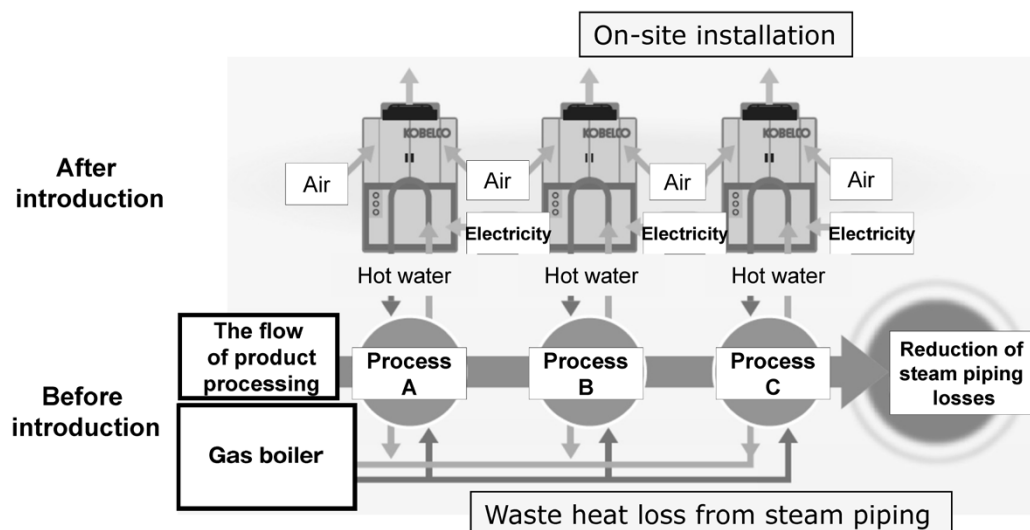


Fig. 7 Introduction method of gas boiler and HEM-90A to a process

and a 56% reduction of energy consumption (Fig. 9). Here, the outdoor air condition is the average temperature of Tokyo, Nagoya and Osaka areas, the electric rate unit price is 12 yen/kWh and the gas rate is 57yen/Nm<sup>3</sup>.

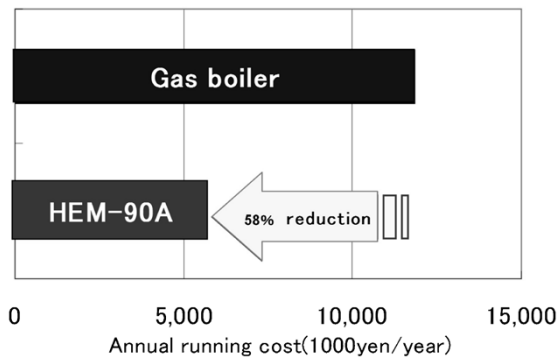


Fig. 8 Estimation of annual running cost

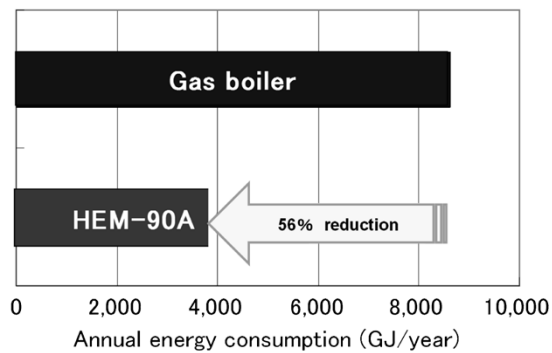


Fig. 9 Estimation of annual energy consumption

## Conclusions

Since the Great East Japan Earthquake, the domestic supply of electrical power has become tight, raising concerns about the increased price of fossil fuels such as petroleum and natural gas. Under such circumstances, the best mix of conventional combustion-type boilers and electrically-driven air-sourced heat pumps, the HEM-90A, is considered to diversify the risk and to save energy. When introducing heat pumps for industrial applications, it is considered important to ascertain in advance the merits of introducing them, including economic efficiency and energy-saving, acquiring a clear picture of each process, because the method of heat utilization varies depending on the manufacturing process.

We will strive to propose heat-source machines that match the user's needs and to contribute to the wide use of industrial heat pumps.

## References

- 1) N. Shimodahira. *Heating Piping & Air Conditioning*. Aug. 2009, No.631, p.28-30.
- 2) N. Shimodahira. *Heating Piping & Air Conditioning*. Sept. 2010, No.647, p.23-25.
- 3) T. Oue et al. *Proceedings of the 2012 JSRAE annual conference*. p.275-276.
- 4) N. Shimodahira et al. *Electro-heat*. Sept. 2012.
- 5) The Energy Conservation Center, Japan. 2007 *National convention on distinguished examples of energy-saving*. <http://www.eccj.or.jp/succase/07/b/26kan10.html>, (accessed 2013-04-09).